

Angular Distributions of  $^{12}\text{C}(\gamma, NN)$  reactions.

Thesis

submitted by

Tony Tsz-Hong Yau

for the degree of

Doctor of Philosophy



Department of Physics and Astronomy,

University of Glasgow,

May 1996.

©Tony T-H. Yau, 1996.

ProQuest Number: 11007920

All rights reserved

INFORMATION TO ALL USERS

The quality of this reproduction is dependent upon the quality of the copy submitted.

In the unlikely event that the author did not send a complete manuscript and there are missing pages, these will be noted. Also, if material had to be removed, a note will indicate the deletion.



ProQuest 11007920

Published by ProQuest LLC (2018). Copyright of the Dissertation is held by the Author.

All rights reserved.

This work is protected against unauthorized copying under Title 17, United States Code  
Microform Edition © ProQuest LLC.

ProQuest LLC.  
789 East Eisenhower Parkway  
P.O. Box 1346  
Ann Arbor, MI 48106 – 1346

Thesis  
10508  
Copy 1



## Abstract

The work presented in this thesis describes an experimental study of the  $^{12}\text{C}(\gamma, pn)$  and  $^{12}\text{C}(\gamma, pp)$  reactions using tagged photons in the energy range of 120MeV to 400MeV. The experiment was carried out using the MAMI-B c.w. electron accelerator at the Institut für Kernphysik, Mainz, Germany.

Bremsstrahlung photons were produced on a thin nickel foil and are tagged by momentum analysing the recoiling electrons using the Glasgow tagging spectrometer. The Tagger tags photons with an energy resolution of 2MeV and a photon flux of  $\sim 10^7\text{s}^{-1}$ . A plastic scintillator hodoscope PIP was used to detect the protons in both reaction channels. It was set in three positions covering polar angles from  $22.7^\circ$  to  $156.7^\circ$  with a resolution of  $\sim 3.5^\circ$  and azimuthal angle from  $-22.8^\circ$  to  $+22.8^\circ$ . The coincidence neutrons or protons were detected in 3 banks each of 4 layers of plastic time-of-flight(TOF) scintillator detectors. These were positioned opposite to PIP in a back-to-back two nucleon breakup kinematic configuration. The total TOF polar angle ranged from  $10.5^\circ$  to  $153.4^\circ$  with a resolution of  $\sim 2^\circ$ , and the azimuthal angle from  $162.5^\circ$  to  $192.7^\circ$ . The detector system has a missing energy resolution of  $\sim 7\text{MeV}$  allowing nucleon breakup from the (1p1p) shells and (1s1p) shells to be isolated. The target is in the form of a 2mm thick graphite sheet.

The results for both reaction channels are presented as double differential cross sections ( $d^2\sigma/d\Omega_1 d\Omega_2$ ) as a function of TOF-side nucleon angles for emission originating from (1p1p) shells and separately for emission originating from the (1p1s) shells. The results are split into six photon energy bins with mean values of  $135\text{MeV} \pm 15\text{MeV}$  then  $175\text{MeV}$  to  $375\text{MeV} \pm 25\text{MeV}$ . Ratios of the strength in the  $(\gamma, pp)$  channel to that in the  $(\gamma, pn)$  channel are also presented.

Preliminary comparisons of the lowest photon energy data with the micro-

scopic theory from Gent in the  $(\gamma, pn)$  channel show fairly good agreement in the shape of the angular distribution. The small observed discrepancy in the magnitude is discussed together with possible improvements which would allow a better comparison. The systematic variations in the measured spectra at higher photon energies are also discussed. Conclusions on the importance of various reaction mechanisms are made.

## Declaration

The data presented in this thesis were obtained by the Nuclear Structure group at the University of Glasgow in collaboration with colleagues from the Nuclear Physics groups at the University of Edinburgh and Tübingen. The experiment was performed at the Institut für Kernphysik at the University of Mainz. I participated fully in the execution of the experiment. The analysis and interpretation of the experimental data is entirely my own work. This thesis was composed by myself.

Tony T-H. Yau

## Acknowledgements

It is my pleasure to take this opportunity to thank all the members of the Glasgow University Nuclear Physics group for all their help and advice throughout my three years of study.

I would like to give a most grateful thank to Prof. Robert Owens, who gave me the opportunity to do this research, and throughout my study has continually gave encouragements and enlightening discussions in all areas of my work. I also like to give a sincere thank to my supervisors, Douglas MacGregor and Cameron McGeorge and also Peter Harty. I am indebted to them all for the many valuable discussions and advice. Their help and guidance over the past three or so years have on many occasions saved me from barking up the wrong tree!

I would like to thank John Annand for his technical expertise in which the performance of this experiment relied upon. Also a big thank to Peter Grabmayr from Tübingen and John Mackenzie from Edinburgh for their part as initiators in getting PIP-TOF into ACQU. An equally big thank to Ian Anthony and Mr Andy Sibald for maintaining the essential computing service, and Gary Miller for the daily lifts to and from the Kelvin Lab.

I like to give thanks to the following worthy people for their inputs to those informative analysis meetings and for sharing those long hours of night shifts. They are, from Tübingen, Torsten Hehl, Ralf Schneider, Tomas Lamparter, Karin Spaeth and Jens Leyboldt. From Edinburgh Derek Branford, Meme Liang and Doug Johnstone and my office mates Dan Watts and Stephen McAllister.

I am grateful to the Insitut für Kernphysik for providing the excellent beam facilities and Juergen Ahrens for his support as A2 spokesperson. Finally I would like to thank the SERC, now EPSRC for the funding of this work, and also the head of the Physics and Astronomy department in Glasgow, Prof. Ferrier for the financial supports for attending international conferences.

To my father.

# Contents

<b>1</b>	<b>Introduction</b>	<b>1</b>
1.1	Introduction . . . . .	2
1.1.1	Photon Probe . . . . .	3
1.1.2	Photo-Absorption . . . . .	4
1.2	Review of Experimental Progress . . . . .	6
1.2.1	Photon Tagging Techniques . . . . .	6
1.2.2	Review of $(\gamma, NN)$ Experiments . . . . .	8
1.3	Review of Theoretical Progress . . . . .	11
1.3.1	The Quasideuteron Model . . . . .	11
1.3.2	The Factorized Quasideuteron Model . . . . .	12
1.3.3	Criticisms of Gottfried's Approach . . . . .	15
1.4	Recent Theoretical Developments . . . . .	16
1.4.1	Nucleon-Nucleon Correlations . . . . .	16
1.4.2	Meson-Exchange Current . . . . .	17
1.4.3	$(\gamma, pn)$ and $(\gamma, pp)$ Channel . . . . .	19
1.4.4	Contributions of Different 2h States . . . . .	21
1.4.5	Direct and Indirect contribution to $(\gamma, NN)$ channels . . .	22
1.5	Recent Angular Distribution Calculations . . . . .	24
1.5.1	$(\gamma, NN)$ Cross Section Formalism . . . . .	25
1.5.2	Final State Interaction . . . . .	28

1.5.3	Absorption Mechanisms . . . . .	30
1.6	Summary and Aim of Present Experiment . . . . .	33
<b>2</b>	<b>Experimental Apparatus</b>	<b>36</b>
2.1	Mainz Microtron : MAMI-B . . . . .	37
2.2	Photon Production . . . . .	39
2.2.1	The Tagging Spectrometer (Tagger) . . . . .	41
2.2.2	The Focal Plane Detector (FPD) . . . . .	42
2.2.3	Photon Beam Collimation . . . . .	44
2.2.4	Tagging Efficiency . . . . .	44
2.3	Targets . . . . .	47
2.4	Particle Detectors . . . . .	48
2.4.1	Start and Veto $\Delta E$ Detectors . . . . .	49
2.4.2	PIP . . . . .	50
2.4.3	TOF . . . . .	52
2.4.4	Experimental Setup . . . . .	52
2.5	Data Acquisition . . . . .	57
2.5.1	Event Information . . . . .	57
2.5.2	PIP-TOF . . . . .	57
2.5.3	Tagger . . . . .	58
2.5.4	Trigger Logic . . . . .	59
2.5.5	Data Acquisition . . . . .	66
<b>3</b>	<b>Detector Calibration</b>	<b>67</b>
3.1	Pedestal Subtraction . . . . .	68
3.2	Discriminator Thresholds . . . . .	68
3.3	Walk Correction . . . . .	70
3.4	Start Detector . . . . .	73

3.5	Tagger . . . . .	74
3.6	PIP . . . . .	74
3.6.1	Position Calibration . . . . .	74
3.6.2	Cosmic : Droop Correction and Alignment of Gains . . .	78
3.6.3	Energy Calibration . . . . .	79
3.7	TOF . . . . .	83
3.7.1	Position Calibration . . . . .	83
3.7.2	Proton Detection . . . . .	84
3.7.3	Timing: Channels to ns . . . . .	87
3.7.4	T-zero : Time-of-Flight . . . . .	88
3.8	Detector Performance . . . . .	91
3.8.1	Missing Energy . . . . .	91
3.8.2	Energy and Angular Resolution . . . . .	92
<b>4</b>	<b>Data Analysis</b>	<b>97</b>
4.1	PIP Proton Selection . . . . .	98
4.2	TOF Neutron Selection for $(\gamma, pn)$ Events . . . . .	99
4.3	TOF Proton Selection for $(\gamma, pp)$ Events . . . . .	101
4.4	Random Subtractions . . . . .	105
4.4.1	Tagger Randoms . . . . .	105
4.4.2	TOF Randoms . . . . .	106
4.5	Tagging Efficiency . . . . .	108
4.6	Neutron Efficiency . . . . .	108
4.7	Hit Multiplicity : Subevents . . . . .	112
4.8	Background Subtraction . . . . .	115
4.9	Cross Section Derivation . . . . .	117
4.10	Solid Angle Determination . . . . .	119

4.11	Dead TOF bars . . . . .	121
4.12	Correction for PIP energy Threshold . . . . .	123
4.13	Experimental Uncertainties . . . . .	125
<b>5</b>	<b>Results and Discussion</b>	<b>128</b>
5.1	Introduction . . . . .	129
5.2	$(\gamma, pn)$ and $(\gamma, pp)$ Angular Distributions . . . . .	130
5.2.1	Method of Presentation . . . . .	130
5.2.2	Comparison of $(\gamma, pn)$ data with Gent Calculations at low Photon Energy . . . . .	131
5.2.3	Conclusion: Low Photon Energy Region . . . . .	136
5.2.4	Systematics of $(\gamma, NN)$ Angular Distribution . . . . .	136
5.3	Ratios of $\sigma(\gamma, pp)/\sigma(\gamma, pn)$ . . . . .	142
5.4	Summary of Experimental Results . . . . .	146
<b>6</b>	<b>Conclusion</b>	<b>147</b>
<b>A</b>	<b>Table of Results</b>	<b>150</b>
<b>B</b>	<b>Correction factors applied to TOF dead bars</b>	<b>175</b>
<b>C</b>	<b>Energy threshold correction factors</b>	<b>176</b>

# List of Figures

1.1	Total photon absorption cross section per nucleon . . . . .	4
1.2	Missing energy spectra of $^{12}\text{C}(\gamma, pn)$ and $^{12}\text{C}(\gamma, pp)$ . . . . .	10
1.3	(a)Correlation function $f(r)$ : (b)resultant cross section . . . . .	17
1.4	$^{16}\text{O}(\gamma, pp)$ cross section (a) with OMY (b) with RSC potential . .	20
1.5	$^{16}\text{O}(\gamma, pn)$ cross section with OMY and RSC at $E_\gamma = 250\text{MeV}$ . .	21
1.6	$^{16}\text{O}(\gamma, pn)$ cross section with OMY and RSC at $E_\gamma = 80\text{MeV}$ . .	22
1.7	$^{12}\text{C}(\gamma, pn)$ and $^{12}\text{C}(\gamma, pp)$ strength from different 2h states . . . .	23
1.8	Photon energy dependence of the various absorption terms . . . . .	25
1.9	Comparison of <i>unfactorized</i> and <i>factorized</i> for the seagull term .	26
1.10	Absorption terms considered for the $(\gamma, pn)$ emission . . . . .	27
1.11	Possible FSI terms for the $(\gamma, NN)$ interaction . . . . .	29
1.12	Higher order absorption terms for the $(\gamma, NN)$ interaction . . . . .	30
1.13	Interference of the $\pi$ -seagull and $\pi$ -in-flight absorption terms . . .	31
1.14	Interference from the heavier meson-exchange . . . . .	32
2.1	Schematic diagram of a racetrack microtron . . . . .	38
2.2	The Mainz Microtron MAMI-B and experimental area . . . . .	40
2.3	Schematic diagram of photon tagging . . . . .	41
2.4	Schematic diagram of the tagging spectrometer . . . . .	43
2.5	Schematic view of the photon beam line . . . . .	46
2.6	Target orientations . . . . .	48

2.7	A schematic diagram of the $\Delta E$ ring . . . . .	50
2.8	A schematic diagram of PIP . . . . .	51
2.9	Schematic diagram of a TOF stand . . . . .	53
2.10	Experimental layout for PIP at FORWARD angle . . . . .	54
2.11	Experimental layout for PIP at CENTRE angle . . . . .	55
2.12	Experimental layout for PIP at BACKWARD angle . . . . .	56
2.13	Schematic diagram of the electronics circuit . . . . .	58
2.14	The 1 <sup>st</sup> Level, Fast Trigger . . . . .	60
2.15	The Sub-1 <sup>st</sup> Level, Cosmic Trigger . . . . .	61
2.16	Plot of $\Delta E_2$ -E for particle identification . . . . .	63
2.17	The 2 <sup>nd</sup> Level: Electron reject logic . . . . .	64
2.18	The 3 <sup>rd</sup> Level: Final trigger logic . . . . .	65
3.1	Pedestal and readout threshold . . . . .	69
3.2	The effect of 'Walk' . . . . .	70
3.3	Walk correction to the $\Delta E_{start}$ . . . . .	71
3.4	Proton selection . . . . .	72
3.5	$\Delta E_{start}$ correction to Tagger TDCs . . . . .	75
3.6	Position calibration method . . . . .	76
3.7	Position calibration parameters . . . . .	76
3.8	Geometrical effect in the Position calibration . . . . .	78
3.9	Pulse height attenuation: Droop effect . . . . .	79
3.10	Light output function:Energy loss through a material . . . . .	80
3.11	Measured gmean of pulse amplitude <i>vs</i> Calculated energy for protons which stop in the PIP E1 layer . . . . .	82
3.12	Measured gmean <i>vs</i> Calculated energy for E1+E2+E3 layers . . .	83
3.13	TOF position calibration . . . . .	84

3.14	Cross check of TOF position calibration . . . . .	85
3.15	TOF charged particle identification . . . . .	86
3.16	TOF missing QDC correction . . . . .	87
3.17	TOF charged particle identification: with missing QDC correction	88
3.18	TOF timing calibration: channels to ns . . . . .	89
3.19	TOF $t_{zero}$ time-of-flight spectrum . . . . .	90
3.20	Double arm $CD_2(\gamma, pn)$ missing energy spectrum . . . . .	92
3.21	Deuterium ridge cut on missing energy . . . . .	93
3.22	Proton energy and angular resolution: from $(E_\gamma, \theta_n)$ . . . . .	94
3.23	Neutron energy resolution from $(E_\gamma, \theta_n)$ . . . . .	95
4.1	Time of flight window . . . . .	100
4.2	Tracking of neutron induced protons through TOF . . . . .	101
4.3	Tracking of protons through TOF . . . . .	102
4.4	TOF proton selection . . . . .	103
4.5	Simulation of proton energy detected in TOF . . . . .	104
4.6	Cuts of Prompt and Random regions in the Tagger timing spectra	106
4.7	Cuts of Prompt and Random regions in the TOF timing spectra .	107
4.8	Tagging Efficiency as a function of Photon energy . . . . .	109
4.9	Neutron Efficiency as a function of Neutron energy for pulse height threshold of 7.6MeVee . . . . .	110
4.10	Neutron Efficiency: Edge effects at end bars in each stand . . . .	111
4.11	Average Neutron Efficiency $\epsilon_n(N = 1, 2, 3, 4)$ . . . . .	112
4.12	Average Neutron Efficiency along a TOF bar . . . . .	113
4.13	Random subtracted missing energy spectrum . . . . .	114
4.14	Background subtracted missing energy spectrum . . . . .	116

4.15	Illustrative diagram for determining $\Delta\Omega_n$ and the corresponding $\Delta\Omega_p$ . . . . .	121
4.16	Combined scatter plots illustrating the angular cuts . . . . .	122
4.17	Threshold cut off on PIP proton energy distribution . . . . .	124
5.1	Comparison of $^{12}\text{C}(\gamma, pn)$ with $\pi$ -meson contributions . . . . .	133
5.2	Comparison of $^{12}\text{C}(\gamma, pn)$ with the effect of $\rho$ -meson contribution . . . . .	135
5.3	$^{12}\text{C}(\gamma, pn)$ data with missing energy 20-40MeV . . . . .	138
5.4	$^{12}\text{C}(\gamma, pn)$ data with missing energy 40-70MeV . . . . .	139
5.5	$^{12}\text{C}(\gamma, pp)$ data with missing energy 20-40MeV . . . . .	140
5.6	$^{12}\text{C}(\gamma, pp)$ data with missing energy 40-70MeV . . . . .	141
5.7	$\sigma(\gamma, pp)/\sigma(\gamma, pn)$ ratio as function of photon energy . . . . .	144
5.8	Angular distribution of $^{12}\text{C}$ $\sigma(\gamma, pp)/\sigma(\gamma, pn)$ ratio . . . . .	145

# List of Tables

2.1	Dimensions of the PIP E blocks . . . . .	52
3.1	Distance proton traversed into detector before generating a TDC STOP . . . . .	77
3.2	Summary of detector performance . . . . .	96
4.1	Information about the targets used for the experiment. . . . .	117
4.2	Missing Energy and Photon Energy Ranges used in the analysis of the experiment. . . . .	119
4.3	Table of $\bar{\theta}_n$ used for evaluating corresponding $\bar{\theta}_p$ . . . . .	120
A.1	$(\gamma, pn)$ cross sections for $E_\gamma=135\text{MeV}$ and $E_m=20\text{-}40\text{MeV}$ . . . .	151
A.2	$(\gamma, pn)$ cross sections for $E_\gamma=175\text{MeV}$ and $E_m=20\text{-}40\text{MeV}$ . . . .	152
A.3	$(\gamma, pn)$ cross sections for $E_\gamma=225\text{MeV}$ and $E_m=20\text{-}40\text{MeV}$ . . . .	153
A.4	$(\gamma, pn)$ cross sections for $E_\gamma=275\text{MeV}$ and $E_m=20\text{-}40\text{MeV}$ . . . .	154
A.5	$(\gamma, pn)$ cross sections for $E_\gamma=325\text{MeV}$ and $E_m=20\text{-}40\text{MeV}$ . . . .	155
A.6	$(\gamma, pn)$ cross sections for $E_\gamma=375\text{MeV}$ and $E_m=20\text{-}40\text{MeV}$ . . . .	156
A.7	$(\gamma, pn)$ cross sections for $E_\gamma=135\text{MeV}$ and $E_m=40\text{-}70\text{MeV}$ . . . .	157
A.8	$(\gamma, pn)$ cross sections for $E_\gamma=175\text{MeV}$ and $E_m=40\text{-}70\text{MeV}$ . . . .	158
A.9	$(\gamma, pn)$ cross sections for $E_\gamma=225\text{MeV}$ and $E_m=40\text{-}70\text{MeV}$ . . . .	159
A.10	$(\gamma, pn)$ cross sections for $E_\gamma=275\text{MeV}$ and $E_m=40\text{-}70\text{MeV}$ . . . .	160
A.11	$(\gamma, pn)$ cross sections for $E_\gamma=325\text{MeV}$ and $E_m=40\text{-}70\text{MeV}$ . . . .	161

A.12 ( $\gamma, pn$ ) cross sections for $E_\gamma=375\text{MeV}$ and $E_m=40\text{-}70\text{MeV}$ . . . . .	162
A.13 ( $\gamma, pp$ ) cross sections for $E_\gamma=135\text{MeV}$ and $E_m=20\text{-}40\text{MeV}$ . . . . .	163
A.14 ( $\gamma, pp$ ) cross sections for $E_\gamma=175\text{MeV}$ and $E_m=20\text{-}40\text{MeV}$ . . . . .	164
A.15 ( $\gamma, pp$ ) cross sections for $E_\gamma=225\text{MeV}$ and $E_m=20\text{-}40\text{MeV}$ . . . . .	165
A.16 ( $\gamma, pp$ ) cross sections for $E_\gamma=275\text{MeV}$ and $E_m=20\text{-}40\text{MeV}$ . . . . .	166
A.17 ( $\gamma, pp$ ) cross sections for $E_\gamma=325\text{MeV}$ and $E_m=20\text{-}40\text{MeV}$ . . . . .	167
A.18 ( $\gamma, pp$ ) cross sections for $E_\gamma=375\text{MeV}$ and $E_m=20\text{-}40\text{MeV}$ . . . . .	168
A.19 ( $\gamma, pp$ ) cross sections for $E_\gamma=135\text{MeV}$ and $E_m=40\text{-}70\text{MeV}$ . . . . .	169
A.20 ( $\gamma, pp$ ) cross sections for $E_\gamma=175\text{MeV}$ and $E_m=40\text{-}70\text{MeV}$ . . . . .	170
A.21 ( $\gamma, pp$ ) cross sections for $E_\gamma=225\text{MeV}$ and $E_m=40\text{-}70\text{MeV}$ . . . . .	171
A.22 ( $\gamma, pp$ ) cross sections for $E_\gamma=275\text{MeV}$ and $E_m=40\text{-}70\text{MeV}$ . . . . .	172
A.23 ( $\gamma, pp$ ) cross sections for $E_\gamma=325\text{MeV}$ and $E_m=40\text{-}70\text{MeV}$ . . . . .	173
A.24 ( $\gamma, pp$ ) cross sections for $E_\gamma=375\text{MeV}$ and $E_m=40\text{-}70\text{MeV}$ . . . . .	174
B.1 correction factors applied to dead TOF bars . . . . .	175
C.1 Detector energy threshold correction factors . . . . .	176

# Chapter 1

## Introduction

## 1.1 Introduction

At photon energies between the Giant Dipole Resonance and the free pion production threshold the mechanisms responsible for photon absorption have been studied with renewed vigour in recent years. This has come about due to the advances in accelerator technology over the last decade allowing the production of high quality, high duty factor electron beams. Experiments using the low duty factor electron beams previously available had large uncertainties due to problems in determining both the photon flux and the photon energy. High duty factor beams made coincidence experiments possible and coupled with the advances in photon tagging techniques, the uncertainties in real photon experiments in determining the photon flux and photon energy are now no longer a problem.

Alongside these experimental advances the theoretical interpretation of photoreactions at the microscopic level has become increasingly sophisticated. The initial discovery back in the 1950's [1] that photoinduced  $pn$  pairs at intermediate photon energies were emitted roughly back-to-back suggested that the nucleon pairs were initially strongly interacting. This mutual interaction between the nucleon pairs was originally [2] attributed to strong short range nucleon-nucleon correlations (SRC). Therefore the  $(\gamma, pn)$  reaction was often quoted as a promising tool for the study of nucleon-nucleon SRC. However it is now realised that meson exchange processes (MEC) play an important role in  $(\gamma, pn)$  reactions and that the effects of SRC are harder to observe than at first suggested. These MEC are suppressed in the  $(\gamma, pp)$  channel which may therefore be more sensitive to SRC.

However, before information on SRC can be extracted, detailed understanding of MEC contributions is essential. Recent theoretical studies [3, 4] suggested that the angular distribution of the  $(\gamma, pn)$  reaction is sensitive to the various terms in the exchange current contributions, and that comparison of  $(\gamma, pn)$  and

$(\gamma, pp)$  angular distributions would give information on the underlying reaction mechanism responsible for the  $(pp)$  emission.

### 1.1.1 Photon Probe

The use of photons as a probe for the nucleus has several advantages compared to using nucleons. The interaction between photons and nuclei is relatively weak in comparison to nucleon-nucleon interactions. This results in a negligible initial state interaction and allows the photon to probe the entire nuclear volume in its ground state. The other major advantage is that the fundamental electromagnetic interaction of the photon with nucleons is well understood, allowing a theoretical understanding of the reaction mechanisms and the extraction of nuclear structure information with no uncertainty due to details of interaction of the probe itself as is the case using nucleon probes.

Due to its zero rest mass the interaction of real photons of energies above say 50MeV with the nucleus imparts a substantial amount of energy with relatively small momentum. This property of the real photon restricts the absorption process on the nucleus. If only one nucleon is involved it must have a high initial momentum well above the Fermi momentum or otherwise the absorption must involve two, or more correlated nucleons in order to conserve momentum and energy. The quasifree knockout process where the photon is absorbed on a single nucleon leading to its emission is therefore inhibited by the momentum mismatch between the photon and the emitted nucleon. The strength of this process decreases rapidly with increasing photon energy and the process gives way to dominant photon absorption on nucleon pairs. Here the momentum can be balanced by the relative momentum of the nucleon pair in their initial states. This picture was reinforced by the early experimental observations [5, 6, 7] that  $pn$  pairs are emitted back-to-back and recent work [8, 9, 10] has confirmed that

the recoil momentum distributions in the  $^{12}\text{C}(\gamma, pn)$  reaction is consistent with the idea that the rest of the nucleus acts as a spectator. It was thought that [2] the initial separation of the nucleon pairs must be very small ( $< 1\text{fm}$ ) and a strong interaction must exist between the two nucleons so that study of  $(\gamma, pn)$  reaction can give information about SRC in the nuclei.

### 1.1.2 Photo-Absorption

An overview of the characteristics of photon interactions with various elements is shown in figure(1.1) [11]. The plot shows the total photoabsorption cross section

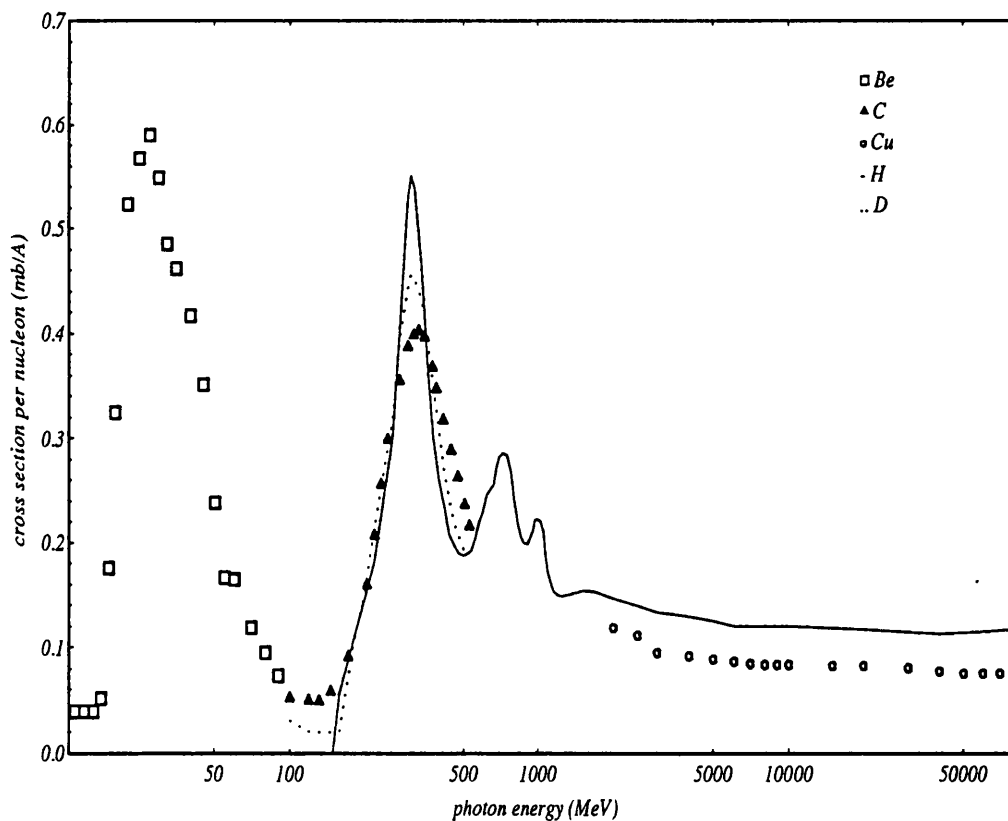


Figure 1.1: Total photon absorption cross section per nucleon

per nucleon as a function of photon energy up to  $\sim 5.5\text{GeV}$ . The general features of the two large resonance peaks and the tailing off to almost constant cross

section at the high energy end are common to all complex nuclei.

The peak at photon energy of  $< 50\text{MeV}$  is the giant dipole resonance peak. This is well described by a collective model where the photon absorption takes place predominantly via electric dipole transitions causing a collective excitation of the whole nucleus. The excited nucleus then decays mainly by the emission of neutrons, since the decay via proton emission is inhibited by the Coulomb barrier. The decay process is statistical resulting in an isotropic angular distribution.

In the range of energies between  $50\text{MeV}$  to  $200\text{MeV}$ , where the cross section is much smaller, the collective model was found to be inadequate [12, 13, 14]. At this intermediate range in the photon energies, conservation of momentum suppresses the photon absorption on a single nucleon. These considerations led to the Quasideuteron Model [15]. The initial proposed model has undergone several changes [16] and modifications [2], but the basic assumption that the absorption process proceeds by absorption on a proton-neutron pair has successfully described the general features of the photo-interaction in this energy range.

At the large resonance peak at  $\sim 300\text{MeV}$ , the cross section per nucleon is almost independent of the nucleus. The absorption in this region is dominated by nucleon excitation via the  $\Delta(1232)$ -resonance. This is the first excited state of the nucleon which decays to a pion and a nucleon. Quasi-free-pion production where the pion is created, but then is reabsorbed on another nucleon pair provides an additional absorption mechanism leading to  $NN$  emission. Recently microscopic model of the photon absorption in the  $\Delta$  region was developed by Carrasco and Oset(see below). The present investigation into the  $(\gamma, NN)$  absorption mechanisms covers the photon energy range from the intermediate region to the  $\Delta$ -resonance region( $120\text{MeV}$  to  $400\text{MeV}$ ) where there is a dramatic change from processes without  $\Delta$  terms to processes dominated by the  $\Delta$ . This allows the corresponding change in the angular distribution, which is predicted to be

sensitive to the various microscopic absorption processes to be investigated across the two regions(see below).

## 1.2 Review of Experimental Progress

### 1.2.1 Photon Tagging Techniques

One of the main problems of photonuclear experiments in the past was the production of a mono-energetic or pseudo mono-energetic photon beams. These problems can in principal be overcome by photon tagging techniques. In all of the principal tagging techniques, an initial electron beam of known energy is used for the production of the photon beam. Generally, one of the products of the initial electron beam interaction must be detected in order to determine the energy of the photon produced. The three principal techniques which have been developed for the production and tagging of photon beams are reviewed below.

- Positron Annihilation-in-flight;  $e^+ + e^- \rightarrow \gamma + \gamma$

A beam of positrons is initially produced from electron bremsstrahlung by pair production in a high  $Z$  converter [17]. This positron beam is momentum analysed to determine its energy. It is then passed through a low  $Z$  material such as beryllium in which positron annihilation with atomic electrons produces pairs of photons of equal energy in the center of mass frame. In the laboratory frame one photon generally has a higher energy than the other. The low energy photons are detected in coincidence with the reaction products, and from their angle the energy of the corresponding high energy photon, which interacts with the target, can be determined.

- Laser Backscattering;  $e^- + \gamma \rightarrow e^{-'} + \gamma'$

Here low energy photons are produced by a powerful laser. These are then

collided with a high energy electron beam. The laser photon undergoes inverse Compton scattering, gaining energy due to the large electron momentum the scattered photon emerges in a direction close to that of the electron beam. Detection of the recoil electron in coincidence with the reaction products determines the energy of the scattered photon.

- Bremsstrahlung;  $e^- \rightarrow e^- + \gamma$

In this process a high energy electron beam is passed through a thin foil such as nickel. A cone of bremsstrahlung photons are produced in the direction of the initial electron beam. The recoil electrons are momentum analysed to determine their energy and are detected in coincidence with the reaction products.

Use of the same bremsstrahlung method of photon production but without the detection of the recoil electrons was in fact employed in many earlier experiments. Measurements of the photonuclear reaction were carried out using bremsstrahlung from electron beams of slightly different energies. The results from the lower electron beam energy are subtracted from the higher beam energy. The technique has an inherent drawback, that is the cancellation of yield due to lower energy photons is not perfect due to the slightly different bremsstrahlung shapes from the two electron beams. The results of these experiments often include a small 'tail' of lower energy photons.

In the most up-to-date facilities such as those at MAMI-B where the experiment of this thesis was carried out, the bremsstrahlung tagging technique is used. MAMI-B provides a high intensity, 100% duty cycle (CW) electron beam, at a well determined energy of 855 MeV. This is complemented by the Glasgow Photon Tagging Spectrometer which is operated with a photon energy resolution of  $\sim 2$  MeV and a maximum photon tagging rate  $\sim 10^8 \text{s}^{-1}$ . The Tagger has a large

momentum acceptance range which allows the energy dependence of the photoreaction to be investigated over a very wide energy range. This is difficult to do with the other established techniques. An inherent advantage of the tagging technique is that by counting individual recoil electrons, it allows the photon flux to be determined reliably.

### 1.2.2 Review of $(\gamma, NN)$ Experiments

Early photonuclear experiments [5, 6, 7, 18] provided a qualitative confirmation of the quasideuteron prediction of Levinger. Using the bremsstrahlung difference technique these experiments confirmed the strong emission of correlated proton-neutron pairs. The average opening angle of the pair in the center of mass was found to be similar to that for the deuteron. Smearing in the opening angle was mainly attributed to the initial momentum of the quasi-deuteron pair and to a lesser extent to final state interactions. One of the earliest  $(\gamma, pp)$  experiments by Weinstein *et al* [19] gave the ratios of  $(\gamma, pp)$  to  $(\gamma, pn)$  cross sections as 0.4% in  ${}^6\text{Li}$  and 2.2% in  ${}^{16}\text{O}$ . They argued that their results were consistent with the assumption of an initial  $(\gamma, pn)$  absorption followed by charge exchange final state interactions(FSI).

Experiments using tagged photons at Bonn by Arends *et al* [20] and similar experiments by Homma *et al* at INS in Tokyo [21, 22, 23] have investigated the photon energy and angular dependence of the emitted protons. These experiments covered photon energies from  $\sim 200\text{MeV}$  to  $\sim 450\text{MeV}$ . The INS group presented proton momentum spectra taken in coincidence with a second correlated nucleon on the other side of the beamline for proton angles of  $23^\circ$  and  $30^\circ$  over a range of light nuclei. The proton spectra from both laboratories supported the strong role of the QD mechanism at the intermediate photon energies. At high photon energies they also provided evidence of the quasi-free pion production(QF $\pi$ )

mechanism. The INS group investigated the  $(\gamma, pp)$  channel in  ${}^9\text{Be}$  and reported an average ratio of  $\sim 6\%$  for  $\sigma(pp)/\sigma(pn)$  which increased with photon energy [22]. This was attributed to the increase in charge exchange FSI of the  $(n, p)$  type from the  $(\gamma, pn)$  channel.

Extensive investigation of the  $(\gamma, NN)$  reaction on several light nuclei in the intermediate photon energy range 80MeV to 157MeV was carried out by the Glasgow group in collaboration with Edinburgh, Mainz and Tübingen Universities [8, 9, 10, 24, 25]. Their 7MeV missing energy resolution allowed them to identify the various shells from which the nucleons were emitted. The most extensive double arm measurements were made on  ${}^{12}\text{C}$  [8, 10]. The missing energy ( $E_m$ ) spectra obtained for  ${}^{12}\text{C}(\gamma, pn)$  and  ${}^{12}\text{C}(\gamma, pp)$  are shown in figure(1.2). The  $(\gamma, pn)$  reaction shows a peak near the reaction threshold indicating that the residual nucleus is often left in or near the ground state. For the  $(\gamma, pn)$  case, the shape of the missing energy spectra can be simulated by folding together two single nucleon missing energy spectra obtained from high resolution  $(e, e'p)$  experiments on  ${}^{12}\text{C}$  [10]. This supports the view that the residual nucleus acts as a spectator during the reaction. The simulation was based on the spectator model and the relative strengths of the  $s$  and  $p$  shells were calculated from the number of nucleons in each shell. The result is shown by the smooth solid line. The dashed line is obtained using the relative  $pp$ ,  $sp$  and  $ss$  absorption strength calculated by Ryckebusch *et al* [26] at  $E_\gamma=151\text{MeV}$ .

The result for the  $(\gamma, pp)$  case, shows no evidence of a peak at threshold and coupled with the results of the simulation suggests that most of the strength does not originate from direct absorption on the proton-proton pairs. Both assumptions about the relative strength of  $pp$ ,  $sp$  and  $ss$  absorption underestimate the strength at high missing energy. Possible reasons for this are simple FSI following  $(\gamma, pn)$  or the onset of virtual pion mechanisms, such as  $(\gamma, N\pi)$  and  $(\pi, 2N)$

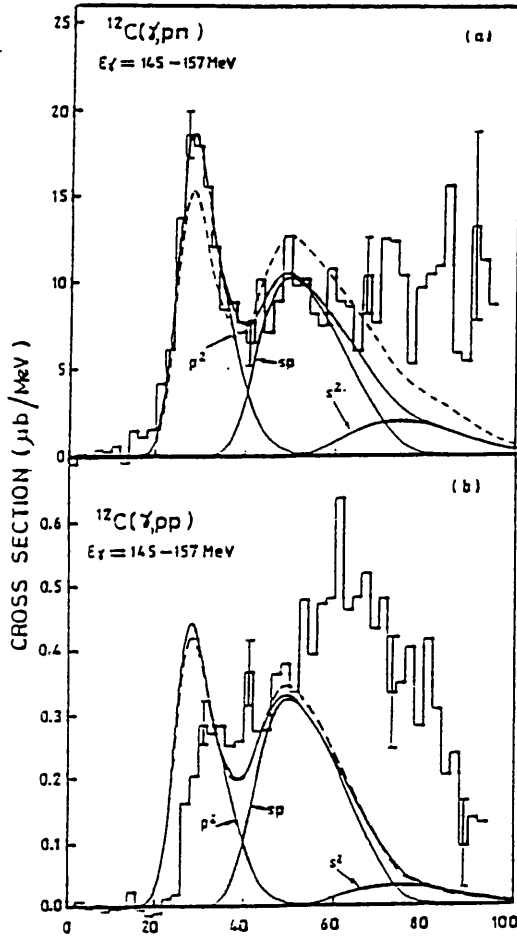


Figure 1.2: Missing energy spectra of  $^{12}\text{C}(\gamma, pn)$  and  $^{12}\text{C}(\gamma, pp)$  for  $E_\gamma = 145\text{--}157\text{MeV}$ . The smooth lines are results from folding spectra derived from  $^{12}\text{C}(e, e'p)$  data. The dashed lines are results from using the calculated  $pp, sp$  and  $ss$  absorption strengths at  $E_\gamma = 151\text{MeV}$ .

which can result in a third undetected nucleon.

The observed recoil momentum of  $(\gamma, pn)$  and to some extent  $(\gamma, pp)$  [10] can be described by a simulation based on the spectator model. One important finding from these measurements is the absence of any significant tail of events with large recoil momenta which indicates that FSI do not introduce significant distortion to the measured events, since large recoil momenta and missing energies are likely to be caused by final state scattering and energy loss.

The strength of final state nucleon absorption, was investigated by Harty *et al* [27] who made a comparison of the  $^{12}\text{C}(\gamma, pn)$  and  $^{12}\text{C}(\gamma, p)$  reaction yields. The results provide an estimate of the neutron transmission in  $^{12}\text{C}$ . An average

transmission of  $\sim 0.80 \pm 0.08$  was found for neutrons of energies 20-45MeV. This indicates that final state absorption is a relatively small effect in this energy range.

## 1.3 Review of Theoretical Progress

### 1.3.1 The Quasideuteron Model

A phenomenological quasideuteron model(QD) in which the  $(\gamma, pn)$  cross section was parameterized in terms of the free deuteron cross section was first developed by Levinger in the early fifties [15]. In his treatment he argued that the strength of the observed  $(\gamma, p)$  cross section at high proton momentum must be due to the proton having high momentum in the initial state. This arises when the proton is in close proximity to another nucleon and experience strong mutual forces. He argues that if the two nucleons are so close together that their separation is less than the average spacing in the nucleus then it is very unlikely that other nucleons will be near enough to be involved in the photon absorption process. Also since the electric dipole term in the photonuclear interaction is dominant only neutron-proton pairs need to be considered in the photonuclear reaction; the proton-proton pair has no dipole moment. In his treatment the incoming photon couples to a  $pn$  pair while the residual  $(A - 2)$  nucleons were regarded as non-participating spectators. With the above arguments he obtained the quasideuteron photoabsorption cross section  $\sigma_{QD}$  by scaling this to the deuteron photodisintegration cross section  $\sigma_D$ .

$$\sigma_{QD}(E_\gamma) = L \frac{NZ}{A} \sigma_D(E_\gamma) \quad (1.1)$$

where  $\frac{NZ}{A}$  corresponds to the density of the quasideuteron pairs and  $\sigma_D$  is the deuteron cross section. The Levinger parameter  $L$  was interpreted as a factor

that takes into account the difference between  $pn$  pair in the nucleus and the real deuteron. It describes an enhancement in the cross section due to the increased  $p-n$  coupling in the quasideuteron. Levinger originally quoted a value for  $L$  of 6.4 for photons  $\sim 150$  MeV. The QD model does not take into account of effects such as Pauli blocking, final state interaction effects(FSI), (though meson exchange effects and any SRC are included implicitly through  $\sigma_D$ ). The value of  $L$  has been estimated from experimental total absorption cross section [11] together with equation(1.1). In many of the earlier  $(\gamma, NN)$  experiments attempts at correcting for Pauli blocking and FSIs and various other experimental uncertainties such as  $NN$  pair detection efficiencies have resulted in widely different  $L$ -values [28].

A modified quasideuteron model (MQD) was later proposed by Levinger [16] in an attempt to account for the effect of the Pauli-blocking for heavier nuclei. The modified model includes a photon energy dependent damping term, and the cross section is given by

$$\sigma_{MQD}(E_\gamma) = L \frac{NZ}{A} \sigma_D(E_\gamma) \exp\left(\frac{-D}{E_\gamma}\right) \quad (1.2)$$

where  $D$  is  $\sim 60$  MeV. The cross section predicted by equation(1.2) are in qualitative agreement with the measured total cross section. Due to various technical difficulties involved in performing the experiments at the time widely different results from several laboratories made quantitative comparisons difficult and often inconclusive.

### 1.3.2 The Factorized Quasideuteron Model

A more sophisticated analysis of the nucleon pair correlation was carried out by Gottfried [2]. He showed that the cross section for the photoproduction of correlated neutron proton pairs could be factorized as

$$d\sigma = \frac{1}{(2\pi)^4} F(P) S_{fi} \delta(\epsilon - \bar{\epsilon}) d^3 k_1 d^3 k_2 \quad (1.3)$$

where  $k_1$  and  $k_2$  are the momenta of the ejected nucleons. The form factor  $F(P)$  is proportional to the probability for finding two nucleons of zero separation and total momentum  $P = |k_1 + k_2 - \omega|$  in the Slater determinant of the independent particle shell model wavefunctions. It is derived from the 'long range' shell model wavefunctions and contains no information about the short range interactions. This is contained in the factor  $S_{fi}$  which is related to the two nucleon short range correlation function. In order to factorize the  $(\gamma, pn)$  cross section into the above form, four main assumptions were made.

- The photo-nuclear interaction energy is the sum of two-body operators and three nucleon effects can be neglected. For photon energies above 100MeV the measured deuteron photodisintegration cross section has a maximum at the same energy as the resonance in photo-meson production. This suggests that in a typical nucleus virtual pion emission and reabsorption is the predominant disintegration mechanism. Gottfried argued that the distance within which the virtual pion mechanism appears to be important is sufficiently small that the probability for finding three nucleons within range of each other is negligible.
- The residual nucleus could be excited to a variety of quantum states. To allow summation over the final states to be carried out, the residual  $(A - 2)$  core was assumed to have a very small excitation energy compared to the initial photon energy. This is termed the *closure approximation*.
- The nucleons of the residual core were assumed to act as mere spectators and have no effect on the photon absorption process.

- The wavefunction  $\Phi_0$  of the bound pair in the ground state was assumed to lead to a Jastrow-type [30] pair correlation function

$$\rho(r_1, r_2) = \rho_s(r_1, r_2) |g(|r_1 - r_2|)|^2 \quad (1.4)$$

where  $\rho_s$  is the pair correlation function derived from the shell model in the Slater Determinant *ie*

$$\rho_s(r_1, r_2) = \int \Phi_s^* \Phi_s d^3 r_3 \dots d^3 r_A \quad (1.5)$$

where  $\Phi_s$  is the ground state nuclear wavefunction. The Jastrow-type function  $g$  is the modification of  $\rho_s$  which accounts for SRC due to nuclear forces.

In addition the photon was assumed to be absorbed by nucleons in a relative  $^3S_1$  state. The factor  $S_{fi}$  can then be written as

$$S_{fi} = 4\pi \frac{3\gamma^3}{[k_p E_p]_0} \left[ \frac{d\sigma_D}{d\Omega_p} \right]_0 \quad (1.6)$$

The photodisintegration cross section in complex nuclei can then be related to deuterium photodisintegration by

$$\frac{d\sigma}{d\Omega_p} = \frac{3\gamma^3}{4\pi^3} F(P) \left[ \frac{d\sigma_D}{d\Omega_p} \right]_0 \frac{k_p E_p}{[k_p E_p]_0} \delta(\epsilon - \bar{\epsilon}) dT_p d^3 k_n \quad (1.7)$$

where  $\gamma$  is a constant and  $[\dots]_0$  denotes evaluation in the frame where  $k_1 + k_2 = 0$ . The factor  $F(P)$  determines the shape of the proton-neutron opening angle distribution. It smears out the correlation in the angular distribution obtained from a stationary deuteron.

The factorized form of the  $(\gamma, pn)$  cross section has proven to be very successful in giving a qualitative understanding of the experimental results. In recent experiments [8, 10, 31] the spectator model was tested quantitatively by comparing the predicted  $pn$  pair momentum distribution based on Gottfried's framework

with the measured recoil momentum spectra in the  $^{12}\text{C}(\gamma, pn)$  reaction. In this framework and, in the absence of final state effects, the momentum of the recoil nucleus is equal and opposite to the initial momentum of the nucleon pair. Here the measured recoil momentum is obtained from

$$\mathbf{P}_{recoil} = \mathbf{P}_\gamma - \mathbf{P}_p - \mathbf{P}_n \quad (1.8)$$

where  $\mathbf{P}_{\gamma,p,n}$  are respectively the measured photon, proton and neutron momentum.

In modelling the initial momentum distribution of the quasideuteron [7], the direction of the initial momentum of the  $pn$  pair was chosen from an isotropic distribution and its magnitude was assumed to follow the distribution of  $\mathbf{P}^2\mathbf{F}(\mathbf{P})$ , where  $\mathbf{F}(\mathbf{P})$  is derived from harmonic-oscillator nucleon wavefunctions and depends on the shells of the two nucleons involved. For absorption where the two nucleons were in the p-shells

$$\mathbf{F}_{1p1p}(\mathbf{P}) = \frac{8}{15\sqrt{2\beta^3\pi}} \left( 3 - \frac{\mathbf{P}^2}{\beta} + \frac{\mathbf{P}^4}{4\beta^2} \right) \exp\left(-\frac{\mathbf{P}^2}{2\beta}\right) \quad (1.9)$$

and if one originates from the s-shell

$$\mathbf{F}_{1p1s}(\mathbf{P}) = \frac{2}{3\sqrt{2\beta^3\pi}} \left( \frac{\mathbf{P}^2}{\beta} \right) \exp\left(-\frac{\mathbf{P}^2}{2\beta}\right) \quad (1.10)$$

The parameter  $\beta$  has the value  $0.302\text{fm}^{-2}$  for  $^{12}\text{C}$  in order to give the correct rms radius.

### 1.3.3 Criticisms of Gottfried's Approach

It has recently been shown by Ryckebusch [32] that the assumptions made in Gottfried's approach were relatively crude approximations especially at photon energies below the  $\Delta$  resonance. It was pointed out that especially at lower photon momentum, where the average range of the exchanged pions is larger,

the approximation assumed in the  $F(P)$  term, that the two nucleons were to be found at zero separation at the point of photon absorption, is not very accurate. Also around the  $\Delta$  resonance region the photon can be absorbed by  $pn$  pairs in a relative P state rather than the relative S state assumed by Gottfried. In addition evidence for photoabsorption on  $T=1$   $pn$  pairs rather than  $T=0$  pairs was reported in recent high resolution  $(\gamma,p)$  measurement [33]. These deviations from the quasideuteron picture supports the Gent group's argument that the  $pn$  pairs in finite nuclei do not fully behave like quasideuterons. Yet, amidst these findings and criticisms, the Gent group acknowledged that the factorized approach is numerically more tractable and allows the 'long range effects' to be separated from any 'short range effects'. Also it is a good approximation for studying the effect of the exchanged of heavier mesons like  $\rho, \sigma$  and  $\omega$ . Furthermore, although a fully unfactorized calculation, taking FSI into account using a partial wave expansion technique, resulted in a reduction in the cross section compared to the factorized calculation, the shape of the angular cross section remained more or less the same.

## 1.4 Recent Theoretical Developments

### 1.4.1 Nucleon-Nucleon Correlations

Early attempts at investigating the effect of simple correlation functions in the  $(\gamma, pn)$  reaction by Weise *et al* [34] assumed the photon absorption mechanisms were exclusively due to the one-body convection current with a proton-neutron correlation function of the Jastrow type

$$f(r) = n_c \left[ 1 - \int j_0 q(r) w(q) dq \right] \quad (1.11)$$

introduced in the shell-model wave function. Here  $n_c$  is a constant and  $w(q)$  is the distribution of exchanged momenta. A delta function for  $w(q)$  was used, and  $q$  is the momentum exchange. This gives rise to an effective two-body photoabsorption process. Figure(1.3a) shows the shape of the correlation function used, and figure(1.3b) shows the calculated  $^{16}\text{O}(\gamma, pn)^{14}\text{N}$  cross section for the emission of  $1p1p$  nucleons compared with a recent tagged photon measurement [9]. Agreement with experiment is obtained with a momentum exchange  $q \sim 300$  MeV/c. A

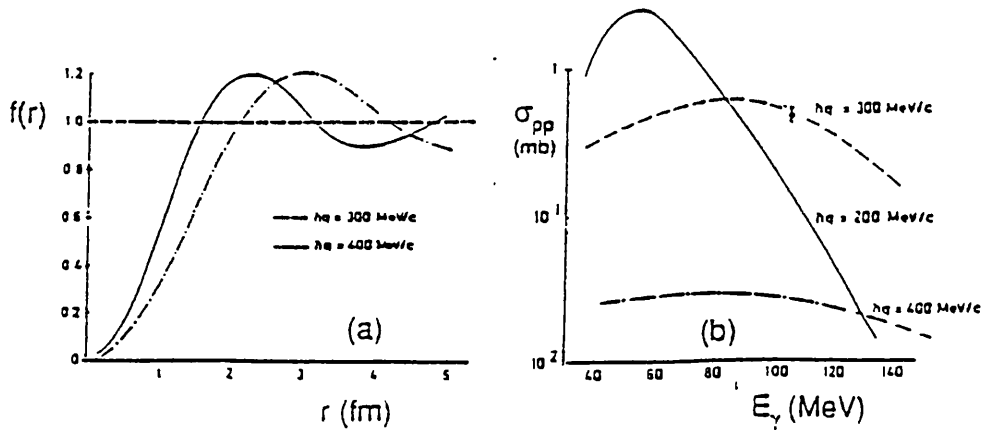


Figure 1.3: (a) Correlation function  $f(r)$  : (b) resultant cross section

major criticism of these early calculations was based on the essentially long range nature of the correlation function. Their calculation illustrated the requirement for an exchange mechanism of moderate momentum and at a range  $\sim 1$  fm. This has now been recognised to be due to the pion exchange mechanism.

### 1.4.2 Meson-Exchange Current

The quantitative contribution of the meson exchange currents (MEC) in photonuclear reactions was first assessed by Gari and Hebach [35]. Their calculation was carried out for photon energies up to 140 MeV for the  $(\gamma, pn)$  reaction, taking into account the exchange current contribution only and neglecting the  $\Delta$ -current

contribution. The use of Siegert's theorem to determine the effect of the meson-exchange currents at photon energies above the giant dipole resonance region has led others to question its validity. The theorem allows the MEC contributions to be calculated without explicit knowledge of the MEC-operators. Siegert [36] showed that the long-wavelength form of the E1 current operator could be written in a form involving only the electric dipole operator which can be calculated from the charge density.

A more fundamental approach for the photon-meson coupling using a Fermi-gas model for the nucleus to describe the  $(\gamma, pn)$  cross section was done by Wakamatsu and Matsamoto [37]. Their results managed to reproduce the qualitative features of the experimental data available then, and they concluded that the effect of the 'virtual' pion played an important role in photoabsorption process.

Boato and Giannini [38] using a factorized approach calculated the contribution of the pion exchange current to the  $(\gamma, NN)$  process on finite nuclei. Here several arguably unrealistic assumptions have to be made before the  $(\gamma, NN)$  reaction cross section can be factorized. Firstly, they assumed no Final State Interaction(FSI), that is, interaction between the outgoing nucleon pairs with the core and with each other are neglected. They evaluated the cross section assuming a simple purely central correlation function, and the separation between the initial nucleon pairs is assumed to be sufficiently small that they move in a relative S-waves which the incoming photon will then couple to. The radial dependence of the relative S-wave was discarded in order to obtain the factorization. They showed that even including MEC and with the assumptions discussed above, the  $(\gamma, NN)$  cross section can still be factorized into two terms; one containing the momentum distribution of the nucleon pairs in the nucleus  $F(\mathbf{P})$ , as in Gottfried's derivation, while the second term is determined by the two-body aspects of the photoabsorption mechanism, namely the MEC and the NN correlation.

### 1.4.3 $(\gamma, pn)$ and $(\gamma, pp)$ Channel

The  $(\gamma, pp)$  reaction was investigated by Giusti *et al* [39] along with the  $(e, e'2p)$  reaction. In contrast to  $pn$  emission which is dominated by MEC from which correlation effects are probably difficult to disentangle, the  $pp$  emission is dominated by the delta excitation with MEC vanishing to first order. The calculation adopts an unfactorized approach and they chose a coplanar and symmetrical kinematics where the two protons are emitted in opposite directions and with equal kinetic energy. Trial short range correlation functions were used for comparison. One, was the hard-core NN interaction of Omhura, Morita and Yamada(OMY) [40],

$$g(r) = \begin{cases} 0 & r \leq c \\ \{1 - \exp[-\mu^2(r-c)^2]\} \{1 + \gamma \exp[-\mu^2(r-c)^2]\} & r > c \end{cases} \quad (1.12)$$

with  $c=0.6\text{fm}$ ,  $\mu=1.118\text{fm}^{-1}$  and  $\gamma=2.078$ , and another was obtained with the Reid Soft-Core  $^1\text{S}_0$  potential [41],

$$g(r) = \left[1 - \exp\left(-\frac{r^2}{\beta^2}\right)\right]^n + hr^m \exp\left(-\frac{r^2}{\gamma^2}\right) \quad (1.13)$$

with  $\beta=0.488\text{fm}$ ,  $n=1.479$ ,  $h=0.901$ ,  $m=5.501$  and  $\gamma=0.602\text{fm}$ . Final state effects were included using outgoing distorted wave functions calculated with an optical potential. Figure(1.4) shows the results for  $^{16}\text{O}(\gamma, pp)$  reaction in coplanar symmetrical kinematics for  $E_\gamma=200\text{MeV}$  and  $T_{p1}=T_{p2}=88\text{MeV}$ . The differential cross section is plotted as a function of the angle ( $\gamma$ ) between the incoming photon and one of the protons in the laboratory frame. The result in figure(1.4a) were calculated with the OMY correlation function and in (1.4b) with the RSC function. The dashed(dot-dashed) line gives the result when only the one-body(two-body) part of the nuclear current is considered, and the solid line gives the complete result. The two-body cross section is much less affected by the choice of the correlation function. The RSC result is dominated both in shape and magnitude by two-body currents, mainly the isobar configuration (IC). In contrast OMY

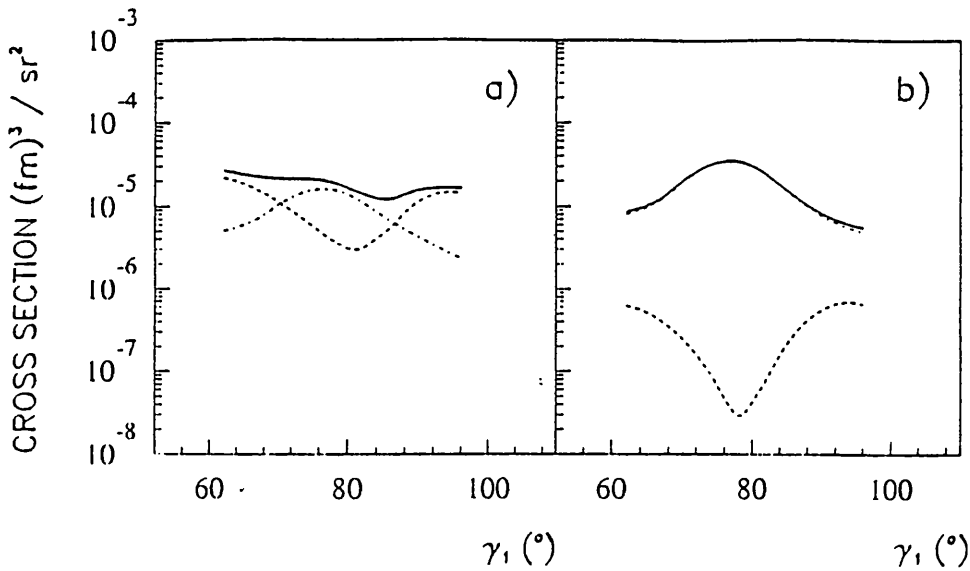


Figure 1.4:  $^{16}\text{O}(\gamma, pp)$  cross section (a) with OMY (b) with RSC potential for  $E_\gamma=200\text{MeV}$  and  $T_{p1}=T_{p2}=88\text{MeV}$ . Dashed line gives the result when only the one-body part of the nuclear current is considered; dot-dashed line when only the two-body part is considered, solid line gives the complete result.

has a very strong one-body part such that both the one-body and two-body contributions have an important effect in determining the magnitude and shape of the cross section. They conclude that with respect to the result obtained with an undistorted wave for the outgoing pairs, the imaginary part of the optical potential reduces the cross section by about 50% and the real part shifts the peak towards higher values of the breakup angle. The choice of the optical potential does not seem to be crucial.

The same approach was extended to the  $(\gamma, pn)$  case in their later publication [42]. Again the calculation only considered currents from the seagull terms and the intermediate isobar excitation and omitted the pion-in-flight term (see figure 1.10) which is of a higher order in the pion propagator. Also the calculation was performed assuming that both nucleons are emitted from the p-shells. The result with the two different SRC functions is shown in figure (1.5). Again the RSC case has a strong two-body part whereas the OMY case is dominated by

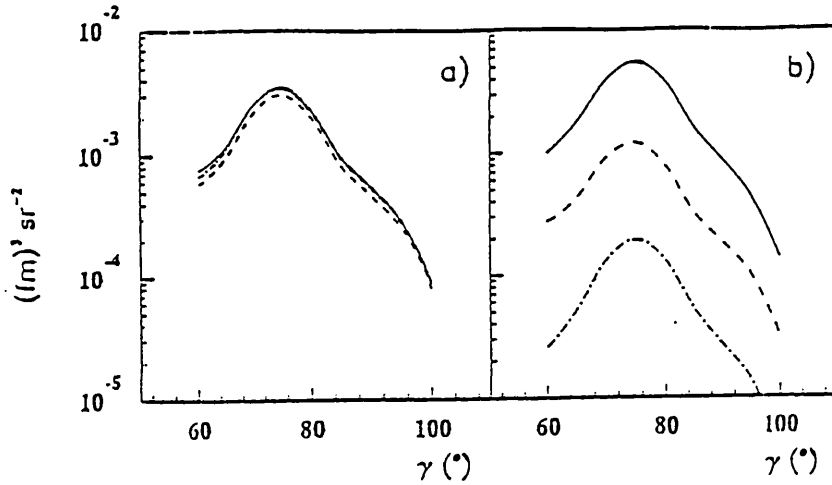


Figure 1.5:  $^{16}\text{O}(\gamma, pn)$  cross section (a) with OMY (b) with RSC at  $E_\gamma = 250\text{MeV}$  in coplanar symmetric kinematics versus the angle of one emitted nucleon. The dot-dashed line has only the one-body current contribution, the dashed line includes the seagull (MEC) term and the solid line includes the IC contribution.

the one-body current. For RSC results at  $E_\gamma = 250\text{MeV}$  shows the IC contribution dominates the two-body part but at  $E_\gamma = 80\text{MeV}$  the seagull contribution dominates, figure(1.6).

At  $E_\gamma=250\text{MeV}$  the absence of the pion-in-flight contribution was suggested to have negligible effect but at  $E_\gamma=80\text{MeV}$ , the authors suggest that due to the destructive interference introduced by the pion-in-flight term as shown by Ryckebusch *et al*, we should expect a lower cross section.

#### 1.4.4 Contributions of Different 2h States

The  $^{12}\text{C}(\gamma, pn)$  strength is dominated by  $(1p)^2$  and  $(1s)^1(1p)^1$  knockout for photon energies below the pion production threshold. As the photon energy increases  $(1s)^1(1p)^1$  knockout becomes dominant. In a naive model we would expect the relative strength in the different 2h channels to be determined by the number of ‘quasi-deuteron’ pairs. The  $(1p)^2$  to  $(1s)^1(1p)^1$  ratio would be 1, and that

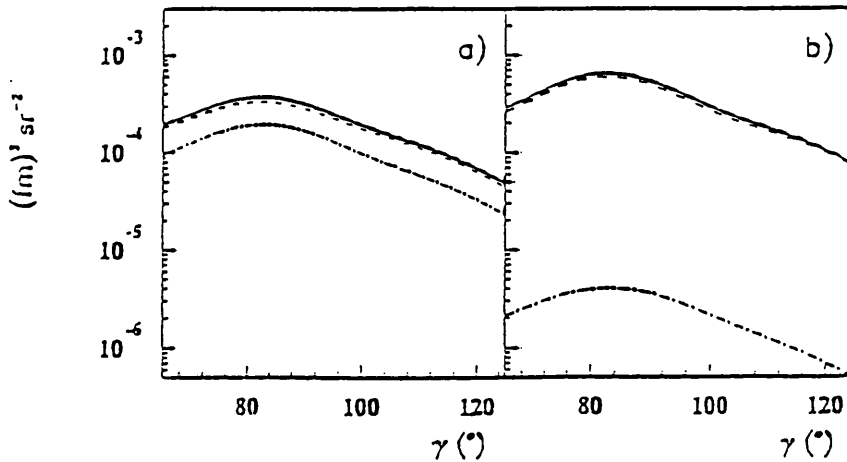


Figure 1.6:  $^{16}\text{O}(\gamma, pn)$  cross section (a) with OMY (b) with RSC at  $E_\gamma = 80\text{ MeV}$ ; same line labelling as figure(1.5).

$(1s)^2$  to  $(1s)^1(1p)^1$  would be  $\frac{4}{16}$ . Calculations [26] of the total photoabsorption strength for  $^{12}\text{C}$  are shown in figure(1.7). It shows the relative strengths of the different 2h states in the  $^{12}\text{C}(\gamma, pn)$  and  $^{12}\text{C}(\gamma, pp)$  channels. For the  $pp$  channel only one absorption mechanism is contributing, namely the  $\Delta$  excitation. The results show that the relative strength in the different 2h channels do not follow the relative number of  $pn$  pairs in each subshell and that a relatively larger strength goes through the  $^{12}\text{C}(\gamma, pn)^{10}\text{B}[(1s\frac{1}{2})^2]$  channel.

#### 1.4.5 Direct and Indirect contribution to $(\gamma, NN)$ channels

Emission of nucleon pairs can also arise from mechanisms other than 2N absorption such as 3N photon absorption or through final state interactions following quasifree photo-pion production. Calculations by Carrasco and Oset [43] consider all the relevant nucleon excitation mechanisms originating from elements of pion nuclear physics and photonuclear reactions. Five basic relevant sources of nucleon excitations are included in the model, namely direct  $\gamma$ -absorption,  $(\gamma, \pi)$  knock out,  $\pi$ -absorption and pion and nucleon scattering. The Valencia model

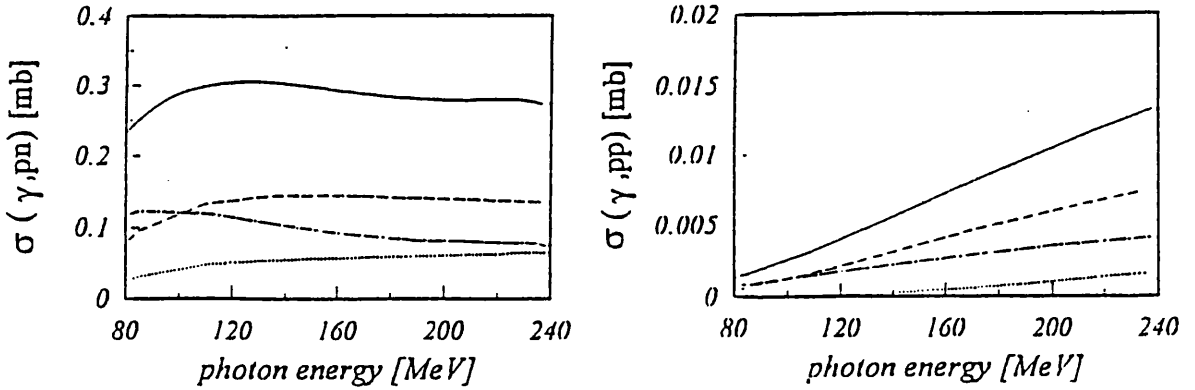


Figure 1.7:  $^{12}\text{C}(\gamma, pn)$  and  $^{12}\text{C}(\gamma, pp)$  strength from different  $2h$  states; the dotted line shows the pair emission strength from the  $1s1s$  shells, dashed line from  $1s1p$ , dot-dash line from  $1p1p$ , and solid line is the total cross section.

uses a microscopic quantum mechanical treatment of the initial photon absorption processes including quasielastic pion production and photon absorption on two or three nucleons. This is followed by a semi-classical tracking of the subsequent propagation and collisions of nucleons and pions within the nucleus based on the local nucleon density approximation and a nucleon-nucleon optical potential. The total cross section for photon absorption in finite nuclei is obtained by integrating the local reaction probability over the whole nuclear volume. In this approach indirect contributions to the  $(\gamma, NN)$  cross section are included. However, in each interaction the particles undergo on their way out of the nucleus, the initial momenta of the secondary nucleons are sampled randomly from a Fermi distribution and the nucleon binding energies are calculated from their momenta assuming zero binding energy at the top of the Fermi sea. The predicted missing energy distributions are thus lower than those observed experimentally and start at 0 MeV for all reaction channels.

The calculations show that at low photon energies the two-body processes dominate the  $(\gamma, NN)$  cross section. At high photon energies a significant contri-

bution arises from  $(\gamma, \pi)$  events followed by pion re-absorption or scattering. The model provides a good overall account of the general features of the measured  $(\gamma, p)$  [44] and  $(\gamma, pn)$  data [45], but it contains no nuclear structure information so it is not expected to predict details as observed for example, in the missing energy spectra. Also the predicted  $(\gamma, pp)$  cross section is too small by a factor of  $\sim 3.5$  when averaged over all proton energies [45].

The microscopic calculation carried out by the Gent group [46] using the basic  $(\gamma, pn)$  and  $(\gamma, pp)$  two-body knock out processes with realistic nucleon momentum distributions in principle is expected to give a better description of the details of the momentum and energy distributions of the outgoing particles for events arising from direct  $2N$  knockout processes.

## 1.5 Recent Angular Distribution Calculations

Recently a very thorough investigation into the  $(\gamma, NN)$  reaction was carried out by the Gent group. The effect of various absorption mechanisms that contribute to the  $(\gamma, pn)$  cross section were investigated using Gottfried's factorized approach [32]. Their results are shown in figure(1.8) where the various absorption terms are plotted as a function of photon energy. Although the pion-in-flight contribution is considerably smaller than the seagull contribution their interference is strongly destructive. This results in a total mesonic cross section much smaller than that obtained in most of the previous calculations where the pion-in-flight term was neglected. Although at photon energies  $>150\text{MeV}$  the  $\Delta$ -contribution becomes more dominant the mesonic contribution remains substantial.

They showed that Gottfried's factorization of the  $(\gamma, pn)$  cross section is only valid when both the quasideuteron and the zero-range approximation turn out to be good approximations. Figure(1.9) shows the cross section for  $^{16}\text{O}(\gamma, pn)$

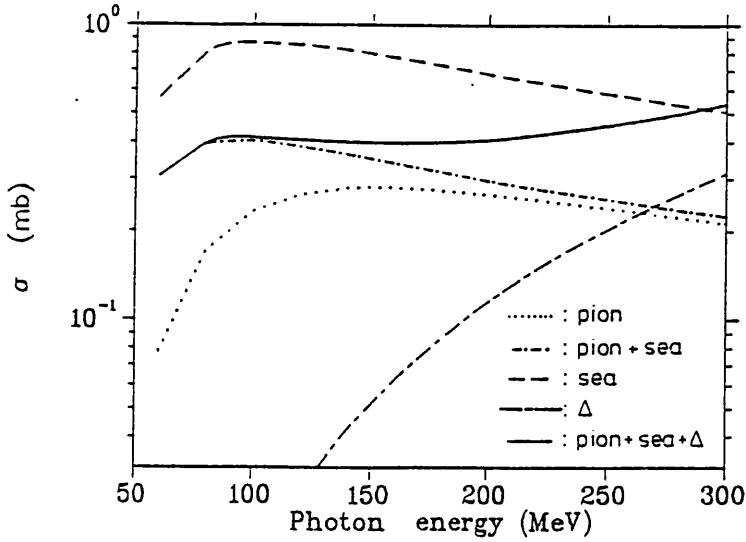


Figure 1.8: *Photon energy dependence of the various absorption terms*

taking into account the seagull term only. The dashed line shows the cross section as calculated within the factorized approach. The dot-dashed line was obtained with an unfactorized method but summed over the relative S wave ( $n=0, l=0$ ). The solid line is the result of a full unfactorized calculation with no restrictions with respect to the relative waves. This result suggests that the lower the photon momentum the larger the average range of the exchanged pions and the more the zero-range approximation fails. Also below the  $\Delta$  resonance region the initial photoabsorption contains contributions due to relative P waves ( $n=1, l=1$ ) which, at  $E_\gamma=60\text{MeV}$ , almost doubles the cross section. In the  $\Delta$  resonance region the assumption of deuteron like behaviour of the  $pn$  pairs and Gottfried's zero range approximation turns out to be reasonable.

### 1.5.1 $(\gamma, NN)$ cross section formalism

Following the absorption of a photon with energy  $E_\gamma$  by the nucleus  $A$ , the cross section for the photoinduced two-nucleon emission

$$\gamma + A \longrightarrow N_a + N_b + (A - 2) \quad (1.14)$$

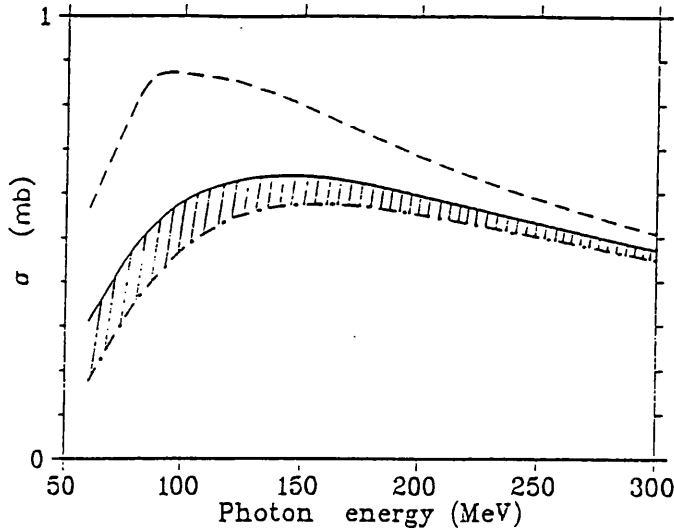


Figure 1.9: Comparison of unfactorized and factorized approach for  $^{16}\text{O}(\gamma, pn)$  for the seagull term only; dashed line shows cross section as calculated within the Gottfried's factorized approach, the dot-dashed line was obtained with the fully unfactorized approach but restricting the sum over the relative  $S$  waves only, the solid line is also unfactorized but with no restriction on the relative  $pn$  waves.

where  $N_a$  and  $N_b$  denotes the two escaping nucleons and  $(A - 2)$  is the residual nucleus which acts as a spectator, is given in the laboratory frame as [26]:

$$\frac{d^5\sigma^{lab}}{d\Omega_a d\Omega_b d\Omega_k} = \frac{1}{(2\pi)^5} \sum_f^a \frac{|m_F^f|^2 k_a^2 E_{A-2} E_a k_b^2}{2E_\gamma [k_a (E_a + E_{A-2}) - E_a (q_\gamma \cos\theta_a - k_b \cos\theta_r)]} \quad (1.15)$$

where  $k_{a,b}$  is the laboratory momentum of nucleon  $N_{a,b}$ ,  $\theta_r$  is the angle between  $k_a$  and  $k_b$ , and  $E_{A-2}$  is the total energy of the residual nucleus in the lab frame. In this form the reaction dynamics are encapsulated in the Feynman amplitude  $m_F^f$ , which is defined as

$$m_F^f = \int dr \exp(iq_\gamma \cdot r) \langle \psi_f | J(\mathbf{r}) \cdot \epsilon_\lambda | \psi_i \rangle \quad (1.16)$$

where  $\epsilon_\lambda$  is the polarization vector of the photon. The form of the nuclear current operator  $J$  depends on the photoabsorption mechanism assumed. The contributions from various mechanisms have been calculated by the Gent group showing their effects on the cross section individually and, most interestingly, the interference between the various mechanisms (see below). Figure(1.10) shows the lowest

order one-pion exchange and the  $\Delta$ -excitation diagrams used in the Gent calculation. The squared Feynman amplitude is proportional to the  $(\gamma, pn)$  cross section

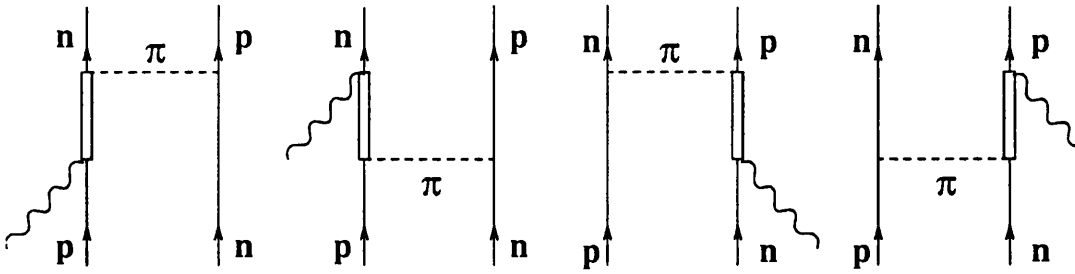
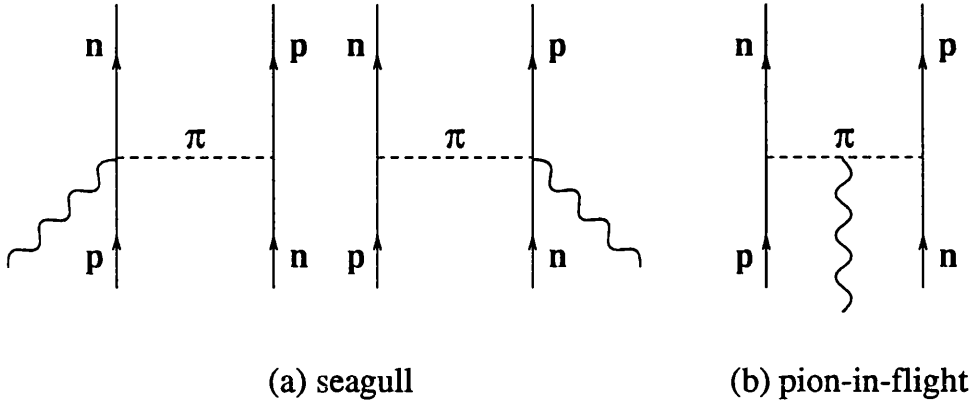


Figure 1.10: Absorption terms considered for the  $(\gamma, pn)$  emission

and in short hand notation can be expressed as

$$|m_F^f|^2 = |m_F^{sea}|^2 + |m_F^{pion}|^2 + |m_F^\Delta|^2 + 2\text{Re} \left( m_F^{sea} (m_F^{pion})^* \right) + 2\text{Re} \left( m_F^\Delta (m_F^{sea})^* \right) + 2\text{Re} \left( m_F^\Delta (m_F^{pion})^* \right) \quad (1.17)$$

where 'sea', 'pion' and ' $\Delta$ ' refer respectively to diagrams a,b and c and  $\text{Re}()$  are the real part of their interference terms.

The A-body wavefunctions  $|\psi_{i,f}\rangle$  are also model dependent. Various assumptions and approximations have been explored by various people in order to construct appropriate wavefunctions which can be used to calculate the angular

cross section for photo-induced two-nucleon emission. There is also the problem of final state effects which ought to be included in the determination of the nucleon-nucleus wavefunctions. The method adopted by the Gent group was to use a distorted wave model for the outgoing nucleon pairs. They extended the shell-model approach from the one-nucleon emission process to the two nucleon emission case by performing a partial wave expansion in terms of  $2h2p$  states. Both the bound state wavefunctions and the continuum partial waves have been calculated in a mean-field potential obtained from a Hartree-Fock calculation with an effective Skyrme interaction. This ensures orthogonality between the bound and the continuum states [46].

### 1.5.2 Final State Interaction

It has always been recognised that the wavefunctions of the escaping nucleons will be affected by the residual core. However the extent of the effects have proved difficult to assess accurately because of the large number and complex variety of strong interactions that can occur. Particularly for two nucleon emission the situation becomes a complicated three-body problem. The simplest technique to account for the FSI is to use optical potentials. The emitted particles are described by distorted waves and the distortion produced by the potential represents the scattering of the particles. Attempts were made by the Gent group to calculate the effect of FSI by explicitly including various possible FSI mechanisms. Some of the simplest cases considered were shown in figure(1.11). The photon is initially absorbed on a two-body current. In figure(1.11a) the two nucleons are simply excited into the continuum state of the mean-field potential. In figure(1.11b) the two nucleons interact with the core and the effect can be accounted for by calculating both distorted waves in an optical potential. Figure(1.11c) accounts for the mutual nucleon-nucleon interaction of the outgoing pairs and in figure(1.11d) the

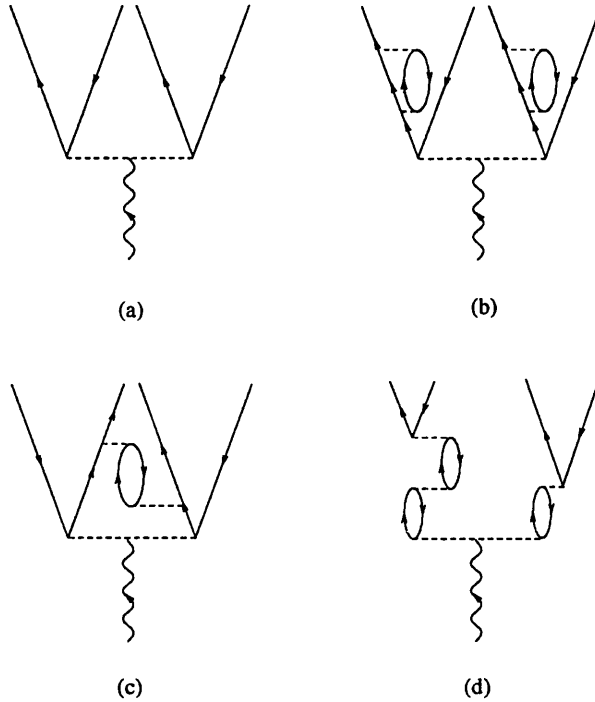


Figure 1.11: Possible FSI terms for the  $(\gamma, NN)$  interaction; (a) the two nucleons excited straight into the continuum state, (b) both nucleons interact with the core, (c) mutual interactions of the two nucleons, (d) rescattering of the two nucleons.

nucleons are assumed to have undergone rescattering; for the details of the formalism see ref [26]. The results from the Gent group's investigation suggest that the full distorted wave calculation yields a reduction of the total strength compared to the plane wave calculation. They found that the reduction is stronger in the  $pn$  case than the  $pp$  case, which they suggest is due to the distortion having a larger effect on the pionic current than on the isobar current. However, the angular correlation remains predominantly back-to-back, and the distortion only gives an overall reduction in strength.

In comparison to the factorized model, the shape of the cross section calculated with unfactorized model including FSI effects is still dominated by the pair momentum distribution  $F(\mathbf{P})$ . The absorption diagrams merely modulate the trend set by  $F(\mathbf{P})$ .

### 1.5.3 Absorption Mechanisms

In all previous investigations by others into the absorption mechanisms that contribute to the  $(\gamma, pn)$  channel have only considered the  $\pi$ -exchange term in their mesonic currents. The Gent group has recently extended this and included heavier meson exchange namely  $\rho$ -exchange. The effect of  $\sigma$  and  $\omega$ -exchange was found to be negligible [3]. Comparisons were made between factorized and unfactorized calculation. Figure(1.12) shows the absorption mechanism diagrams considered. In the unfactorized calculation, an analytical approach was used em-

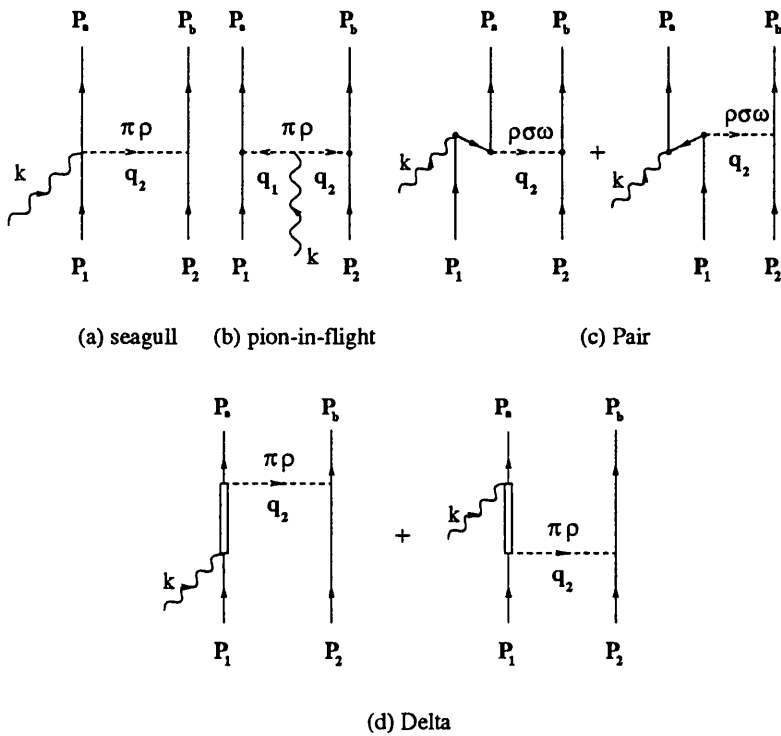


Figure 1.12: Higher order absorption terms for the  $(\gamma, NN)$  interaction

ploying momentum space harmonic-oscillator wavefunctions instead of the more usual partial-wave expansion technique. Figure(1.13a) shows the differential cross sections calculated for  $^{16}O(\gamma, pn)$ . Diagram(1.13c) shows the cross section plotted against the proton angle where the corresponding neutron angle gives the

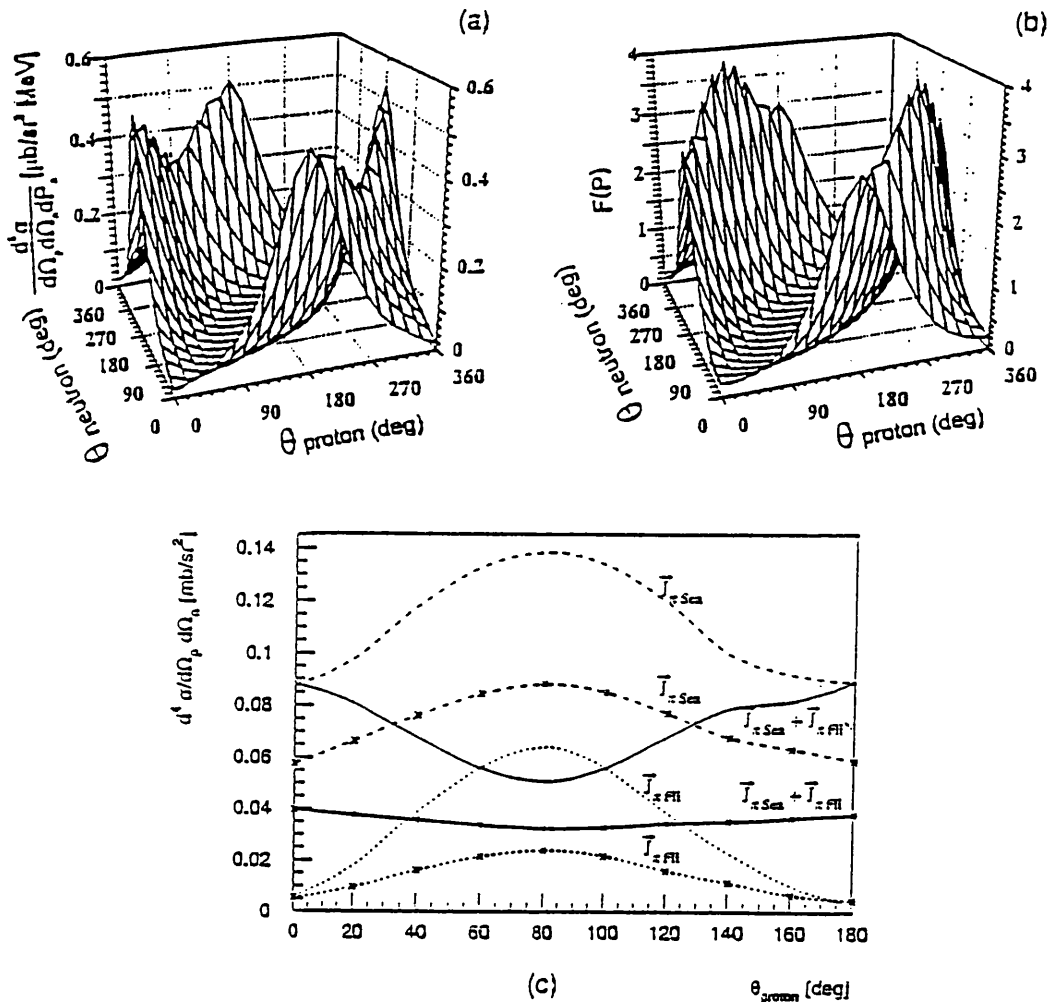


Figure 1.13: *Interference of the  $\pi$ -seagull and  $\pi$ -in-flight absorption terms; (a) Differential cross section ( $d^5 \sigma^{lab} / d\Omega_p d\Omega_n d|p|$ ), (b) The nuclear structure function  $F(P)$ , (c) Plane-wave unfactorized (stars) and factorized (no star) angular cross section, for the  $^{16}\text{O}(\gamma, pn)$  reaction at  $E_\gamma = 100\text{MeV}$  and  $T_p = 40\text{MeV}$  for  $J_{\pi sea}$  and  $J_{\pi Fli}$ .*

maximum values of  $F(P)$  the shape of which is shown in (1.13b). The cross section value is essentially the height of the ridge in diagram(1.13a). The important results that motivated the present experimental work is the observed strong destructive interference between the  $\pi$ -seagull and  $\pi$ -in-flight diagrams causing a change in shape in the angular cross section. This interference is believed to be inherent to the nature of the two terms as it results from both the factorized and plane-wave unfactorized approach. With the inclusion of the  $\rho$ -meson exchange

current further interference effects were observed. Figure(1.14) shows the angular cross section obtained from the same method as in figure(1.13) but for a higher photon energy of 140 MeV. There is a reduction in the cross section in both the factorized (no star) and unfactorized (starred) method. In the calculation of the  $\rho$ -currents the  $\rho$ -seagull current was found to be the dominant contribution hence only the  $\rho$ -seagull terms was included in the calculation.

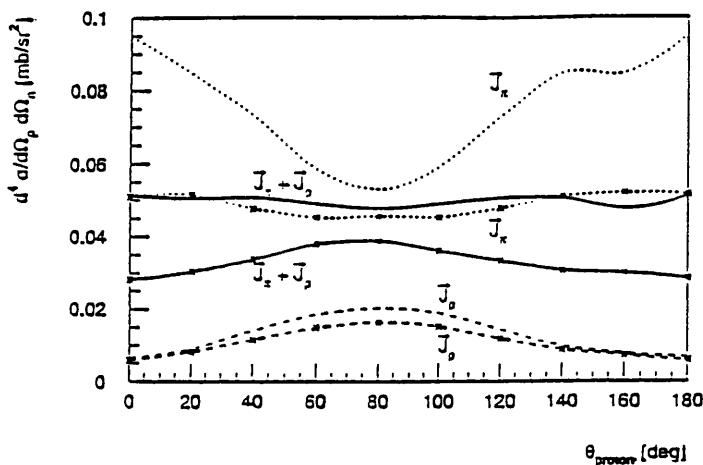


Figure 1.14: *Interference from the heavier meson-exchange. Unfactorized (starred) and factorized (no stars)  $^{16}\text{O}(\gamma, pn)$  angular cross section for  $\pi$ -current (dotted line),  $\rho$ -current (dashed line) and  $\pi + \rho$ -current at  $E_\gamma=140\text{MeV}$ .*

With increasing photon energy, the  $\Delta$ -contribution will increasingly dominate over the purely mesonic ( $\pi + \rho$ ) contribution. The inclusion of the  $\rho$ -meson in the  $\Delta$ -current leads to a strong destructive interference between the  $J_{\Delta\text{pion}}$  and  $J_{\Delta\text{rho}}$  currents [3]. However the magnitude of the effect depends on the  $\rho NN$  and  $\rho N\Delta$  coupling constants, and also in the  $\Delta$ -resonance region medium effects are believed to cause a reduction in the cross section. Little information is available on the value of the coupling constants or on the extent of the reduction due to medium effects.

Although this theoretical approach has not yet been carried out for the  $^{12}\text{C}$  nucleus, the results for both nuclei are not expected to be very different. On the

experimental point of view the missing energy peak corresponding to the  $pp$ -shell breakup in  $^{12}\text{C}$  is much cleaner and easier to select out than in  $^{16}\text{O}$ , hence favoring the used of  $^{12}\text{C}$  as target.

## 1.6 Summary and Aim of Present Experiment

Previous experiments have found that for photon energies in the region of 100MeV to 300MeV the result of photoabsorption on the nucleus often leads to the strong emission of proton-neutron pairs. The emission of proton-proton pairs is  $\sim 2\%$  of the  $pn$  emission rate at 100MeV rising to  $\sim 12\%$  at 300MeV. The relatively low cross section in the  $pp$  emission compared to the  $pn$  emission is understood to be due to the absence of pion exchange current between the  $pp$  pair. Difficulties in earlier experiments were mainly due to the problem of determining the initial photon energy or compromising that with low particle energy resolution in their detectors. This often leads to inconsistency in the results from different laboratories.

On the theoretical side most of the  $(\gamma, NN)$  calculations carried out during the seventies overlooked the importance of meson exchange currents and have mistakenly assumed their contribution to be negligible. The  $(\gamma, pn)$  reaction is now recognised to arise largely from the photoabsorption on two-body currents of meson exchange nature. On the other hand the  $(\gamma, pp)$  channel cannot be fed directly from absorption on a mesonic current. Hence short range correlation effects are not complicated by meson exchange effects as in the  $(\gamma, pn)$  channel, and it has been suggested that the  $(\gamma, pp)$  channel, though much weaker, would be more sensitive to the short range correlation.

The photoabsorption mechanisms for both the  $(pn)$  and  $(pp)$  emission must be understood before any short range correlation effect can be extracted. Most

recent calculations have suggested that at energy of  $\sim 100\text{MeV}$  to  $300\text{MeV}$  the dominant reaction mechanisms responsible for the  $(\gamma, pn)$  reaction are the pionic exchange term, intermediate delta excitation and nucleon-nucleon correlations. In the pionic current the so called *seagull* term and the *pion-in-flight* term are dominant, with the higher order terms being negligible. The largest contribution comes from the *seagull* term and the  $\Delta$  term causes an increase in the overall cross section with increasing photon energies.

The most interesting feature to come out of the Gent calculations [26] was a destructive interference from the pion-in-flight term, resulting in a dramatic change in the angular distribution. These calculations suggest that the angular distribution may be sensitive to the details of the reaction mechanisms. A detailed understanding of the  $(\gamma, pn)$  reaction mechanisms would enable us to access the contributing reaction mechanisms in the  $(\gamma, pp)$  channel. Calculations suggest that only the  $\Delta$  term and the short range correlation would most likely result in a direct  $pp$  emission. There is a possibility that this channel can also be fed from the stronger  $(\gamma, pn)$  channel through a multi-step process in which the neutron undergoes a rescattering process of the  $(n, p)$  type. The coupling between the  $(\gamma, pn)$  and the  $(\gamma, pp)$  channels needs to be understood in order to explain the two-nucleon emission processes.

The present experiment was fueled by the findings of the Gent group. The interference between various exchange terms in the photoabsorption mechanism is predicted to affect the  $(\gamma, pn)$  angular distribution, both in the magnitude and the shape of the cross section. The aim of this thesis is to obtain the angular distribution of the  $(\gamma, pn)$  reaction over a large angular range and photon energy range, and where possible to compare this with the theory. Though theoretical angular distributions for  $^{12}\text{C}(\gamma, pn)$  are not yet available, the predictions for  $^{16}\text{O}(\gamma, pn)$  can be used as a guide, since calculations for both nuclei are expected

to be similar. The angular distribution of the  $pp$  channel will also be obtained for the comparison with the  $pn$  channel. This should yield information concerning the  $\Delta$ -excitation mechanism or may indicate whether  $(\gamma, pp)$  is dominated by charge exchange FSI.

## Chapter 2

# Experimental Apparatus

## Introduction

The experiment described in this thesis was carried out using the 855 MeV electron beam at the Institut für Kernphysik at Mainz University in Germany. It was done in collaboration with other physicists from Glasgow, Edinburgh, Tübingen and Mainz Universities. The electron beam is directed towards a thin radiator where it produces Bremsstrahlung photons. The energies of these photons can be determined by detecting the associated recoiling electrons. This is done using the Glasgow photon tagging spectrometer. The photon beam is then collimated before reaching the target, where photon induced reactions are studied. Reaction products are detected by two separate systems of plastic scintillators, PIP and TOF. Protons are detected by PIP, a large solid angle segmented hodoscope which can also be used to detect pions in  $(\gamma, \pi N)$  experiments. Correlated nucleons are detected by TOF which measures their energies by their time of flight. For particle identification in the TOF detector system a thin  $\Delta E$  transmission layer close to the target was employed. Two such  $\Delta E$  transmission layers are also used in the PIP detector system, one layer for particle identification ( $\Delta E_2$ ), and the other ( $\Delta E_{start}$ ) which is closer to the target, is used to provide the coincidence trigger. When an event satisfies a pre-defined set of coincidence requirements all the energy and timing information from the Tagger and PIP-TOF detectors are collected and stored by the data acquisition.

### 2.1 Mainz Microtron : MAMI-B

In coincidence experiments using tagged photons the use of a continuous electron beam rather than a pulsed beam has the advantage of a much higher real to random coincidence ratio for a given average current. It also avoids the problem of pile-up in the detectors and reduces dead times in the data-acquisition. The

above problems could be avoided if the instantaneous current from a microtron is low. MAMI-B can provide a maximum beam current of  $100\mu\text{A}$  at a resolution of  $60\text{keV}$ , but for the present work a current of  $\sim 30\text{nA}$  was used throughout.

The Mainz Microtron, MAMI-B, produces a 100% duty factor continuous electron beam at a current from a few picoamps up to one hundred microamps. The beam has low emittance and is highly stable.

MAMI-B essentially consists of three successively larger Race Track Microtrons(RTM) see figure(2.1).

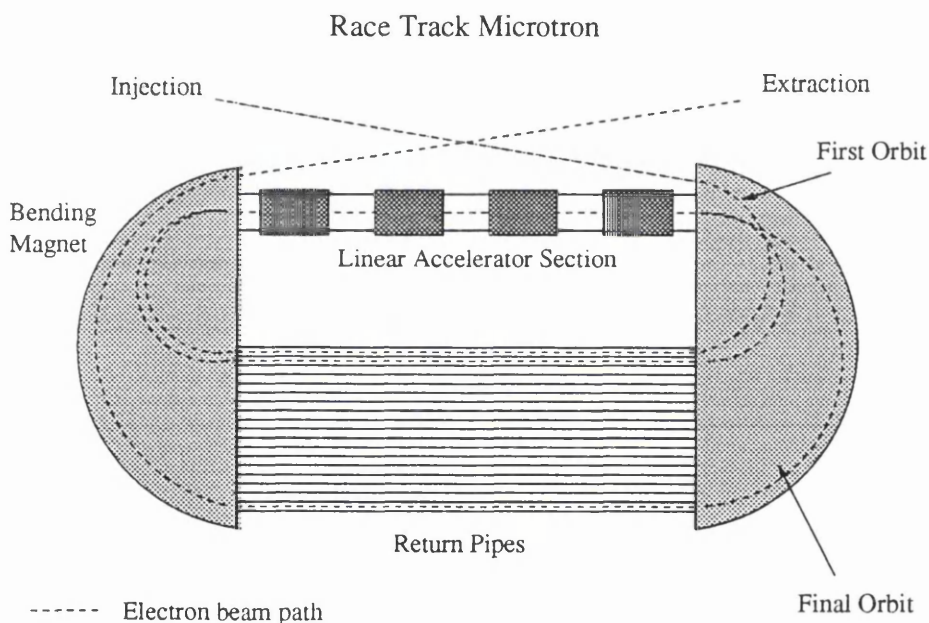


Figure 2.1: *Schematic diagram of a racetrack microtron*

Each RTM consists of a linear accelerating section(linac) which the electron beam passes through many times, each time being accelerated along waveguides by radio frequency fields provided by klystrons. The electrons are recirculated many times through the linac and on each pass the electrons gain a relatively low energy boost. This allows the accelerating klystrons to be operated in a continuous wave mode. The electron beam is recirculated back to the linac by two

bending magnets and an array of return pipes. After each pass through the linac the electrons have a larger orbit radius allowing them to travel through separate return pipes. The increase in orbit length is an integer number of wavelengths of the accelerating RF field, so on re-entering the linac the electrons are in phase with the field. On extraction the beam acquires the RF microstructure, but since the RF frequency of 2.45GHz is high this is not distinguishable by the particle detectors and is seen as a continuous beam.

The principle workings of MAMI-B, figure(2.2), start with a 100keV electron gun. The beam is then fed into a 3.5MeV linac which then injects it into the first stage of MAMI-B, which is an 18 turn Race Track Microtron(RTM1). This increases the beam energy to 14MeV before entering the second stage, a 51 turn RTM2. This increases the beam energy to 180 MeV before entering the final stage, RTM3 which has 90 turns and boosts the final beam energy to 855MeV. The beam emerges with a resolution of 60keV and an emittance of less than  $0.14\pi$ .mm.mrad. The beam produced is then steered by a number of dipoles into the (A2)Tagger hall. Some focusing of the beam is done by quadrupoles inside the hall.

## 2.2 Photon Production

The electron beam is focused onto a radiator which is a  $4\mu\text{m}$  Ni foil. Bremsstrahlung photons are produced as electrons decelerate in the presence of Ni nuclei. The photons radiate in a forward cone of average semi-angle  $m_e/E_e$ , where  $m_e$  is the mass of the electron and  $E_e$  is the kinetic energy of the electron. The energy distribution of these photons can be approximated as being proportional to  $1/E_\gamma$ .

Keeping the radiator thin reduces multiple scattering and consequently minimises the divergence of the photon beam and maximises the tagging efficiency

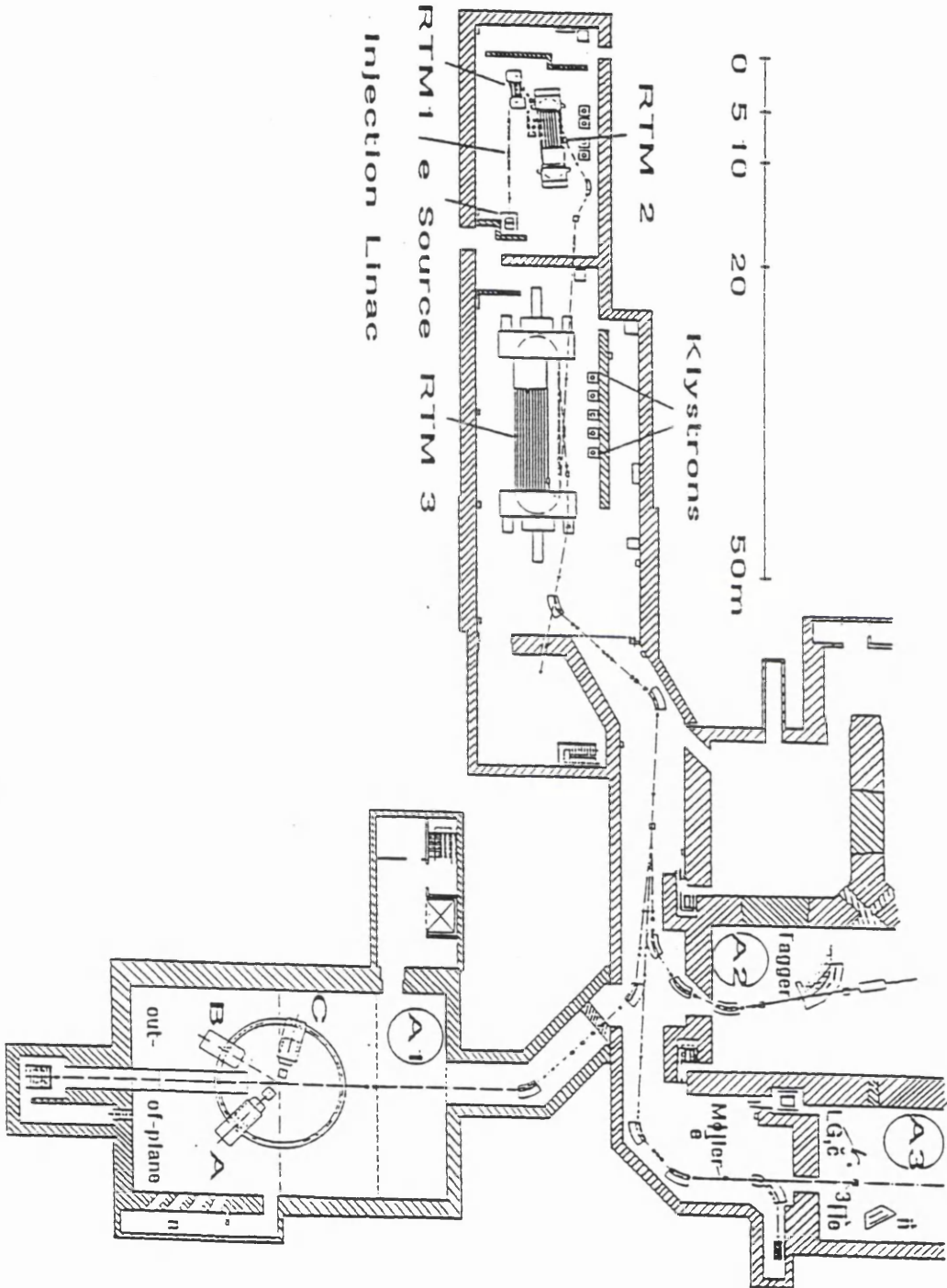


Figure 2.2: The Mainz Microtron MAMI-B and experimental area

(see below), but is at the expense of a low photon flux. Thin, high  $Z$  materials are difficult to handle since to get the same radiation length as Ni the thickness required would be extremely thin and easily be torn, but low  $Z$  material gives a larger Møller scattering resulting in a lower tagging efficiency. The choice of the Ni radiator is a compromise between high photon flux and high tagging efficiency and robustness.

### 2.2.1 The Tagging Spectrometer (Tagger)

The energy of Bremsstrahlung photons can be determined by measuring the energy of the recoiling electrons  $E'_e$ . The Glasgow Tagger, a combined quadrupole-dipole, is a magnetic spectrometer designed to momentum analyse the recoiling electrons. Since the initial electron beam energy is known  $E_e = 855\text{MeV}$  the photon energy is then given by

$$E_\gamma = E_e - E'_e \quad (2.1)$$

see figure(2.3).

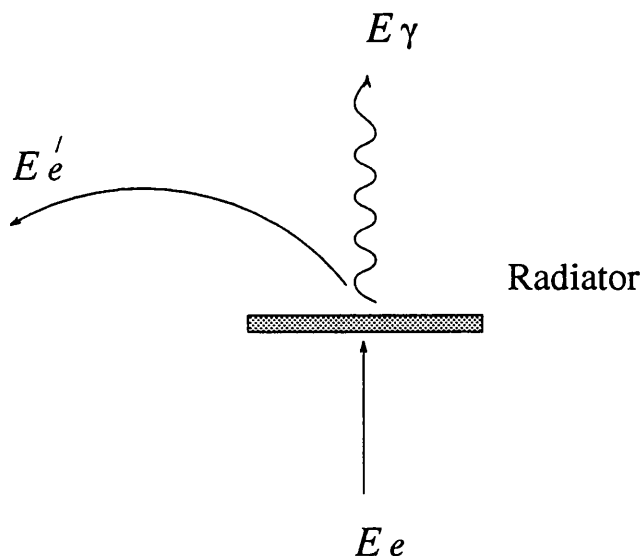


Figure 2.3: Schematic diagram of photon tagging

The Tagging Spectrometer is shown in figure(2.4). The design of the Tagger must satisfy a few criteria which are essential for this experiment. The main bending dipole also serves to re-direct the unscattered beam away from the experimental hall and into a Faraday Cup beam dump. The spectrometer also has a wide angular acceptance for the recoiling electrons, so most of the electrons will reach the focal plane. The focal plane is reasonably flat allowing a more simple focal plane detector design. Along with the quadrupole magnet which allows focusing in the vertical direction, the high homogeneity of the main dipole magnetic field gives the spectrometer an overall intrinsic resolution of  $\sim 120\text{keV}$  over the entire tagging range [47, 48]. The spectrometer has a wide momentum acceptance with the ratio of  $p_{max}$  to  $p_{min} \sim 16:1$ . This allows it to tag photons from  $40\text{MeV}$  to  $790\text{MeV}$ , but in this experiment the lower photon energy section of the focal plane detector ( $E_\gamma < 110\text{MeV}$ ) was switched off to allow the use of a more intense electron beam.

### 2.2.2 The Focal Plane Detector (FPD)

To compromise between reasonable cost and reasonable resolution the focal plane detector was constructed with an array of 353 scintillators. Each is equipped with its own photomultiplier(PM) tube, a dual threshold discriminator with a timing resolution of better than  $1\text{ns}$ , and a logic coincidence unit. The scintillators are located along the median line of the focal plane covering the whole accessible length [49]. Each element overlaps its neighbours and a 'hit' requires a coincidence signal between neighbouring pairs. This requirement reduces spurious background electrons. The total electron energy acceptance is  $40\text{MeV}-790\text{MeV}$  with about  $2.2\text{MeV}$  resolution.

All hit signals are counted by FASTBUS scalers. The sum of these scalers corresponds to the total number of bremsstrahlung electrons in the tagged range

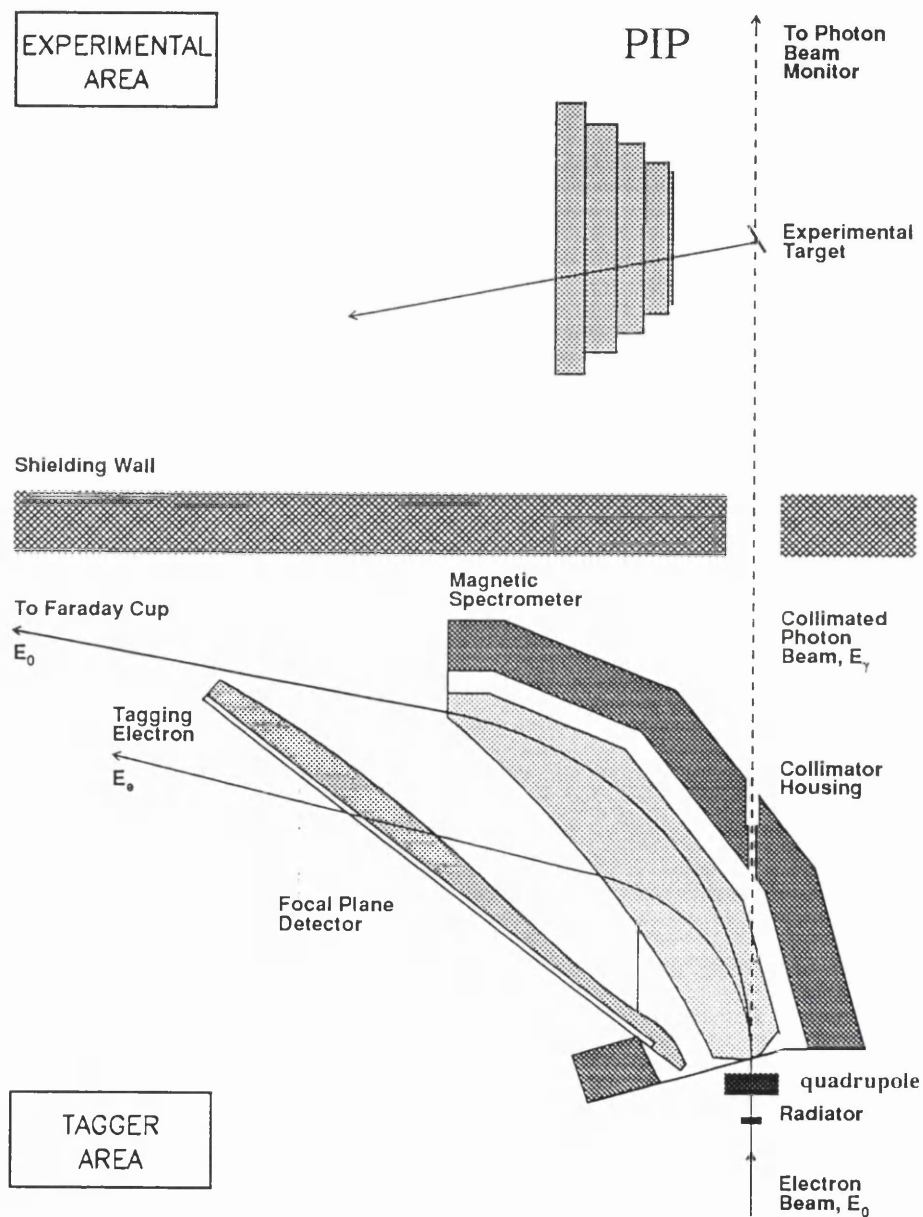


Figure 2.4: Schematic diagram of the tagging spectrometer

and are used to calculate the photon flux through the target. The scalers are disabled by a trigger(see below) from PIP/TOF so that when a photoreaction event is identified no more hit signals will be counted by all the scalers. The scalers are enabled when the acquisition system is ready for the next event. This method avoids the need for any deadtime correction when calculating experimental cross sections.

The FPD timing information is processed by a time to digital converter(TDC). This is 'gated' by the data acquisition system with an 80ns gate. Within this time hit signals must come from the focal plane in order to be accepted as a possible coincidence with the photoreaction induced at the target.

### 2.2.3 Photon Beam Collimation

A small well defined beam spot on the target is desirable in order to minimize the uncertainty in defining the reaction vertex. Hence the photon beam was collimated by three sets of lead collimators. The closest to the radiator positioned at 250cm down the photon beam line is 5cm long and 5mm in diameter. This defines the beam spot size at the target. The two other sets of collimators placed further down the beam line were designed to stop any charged particles produced in the first collimator from reaching the  $\Delta E$  detectors which are placed close to the beam. The beam spot at the target is 15mm in diameter. This contributes  $\sim 0.6^\circ$  uncertainty to the particle's measured trajectories.

### 2.2.4 Tagging Efficiency

The Tagger scalers count the number of recoil electrons detected in the FPD. Due to the photon beam collimation, not all the bremsstrahlung photons produced will reach the target. In order to determine the photon flux through the target the

tagging efficiency  $\epsilon_t$  must be determined. This is the fraction of electrons detected in the FPD having an associate photon which reaches the target. It was measured in a separate experiment using a Pb glass detector which was placed directly on the photon beam line, figure(2.5).

The Pb glass detector represents 30 radiation lengths and thus has  $\sim 100\%$  photon detection efficiency. The Tagger TDCs are now 'gated' by the signals from the Pb glass. The number of times the TDC registers a signal corresponds to the number of photons reaching the target. Thus the tagging efficiency for each Tagger element is:

$$\epsilon_t = \frac{\text{TDCcounts}}{\text{SCALERcounts}} \quad (2.2)$$

Measurements of the tagging efficiency were made periodically throughout the whole experiment. This was done with a very low electron beam current. This allows the Pb glass to detect all incoming photons and reduces random coincidences in the Tagger to a negligible level. The average tagging efficiency remained stable at  $\sim 55\%$ .

For on-line monitoring of the photon beam, an ion chamber was placed directly in the photon beam. The ratio of the current in the ion chamber to the rate of the electrons detected in the FPD gives an on-line indication of the tagging efficiency. This serves to monitor any drifts in the initial electron beam, which would result in a decrease in the tagging efficiency. In addition, a sensitive TV camera was also used to give a visual on-line image of the position and profile of the photon beam. This was also used to set up the position and direction of the electron beam at the beginning of the experiment.

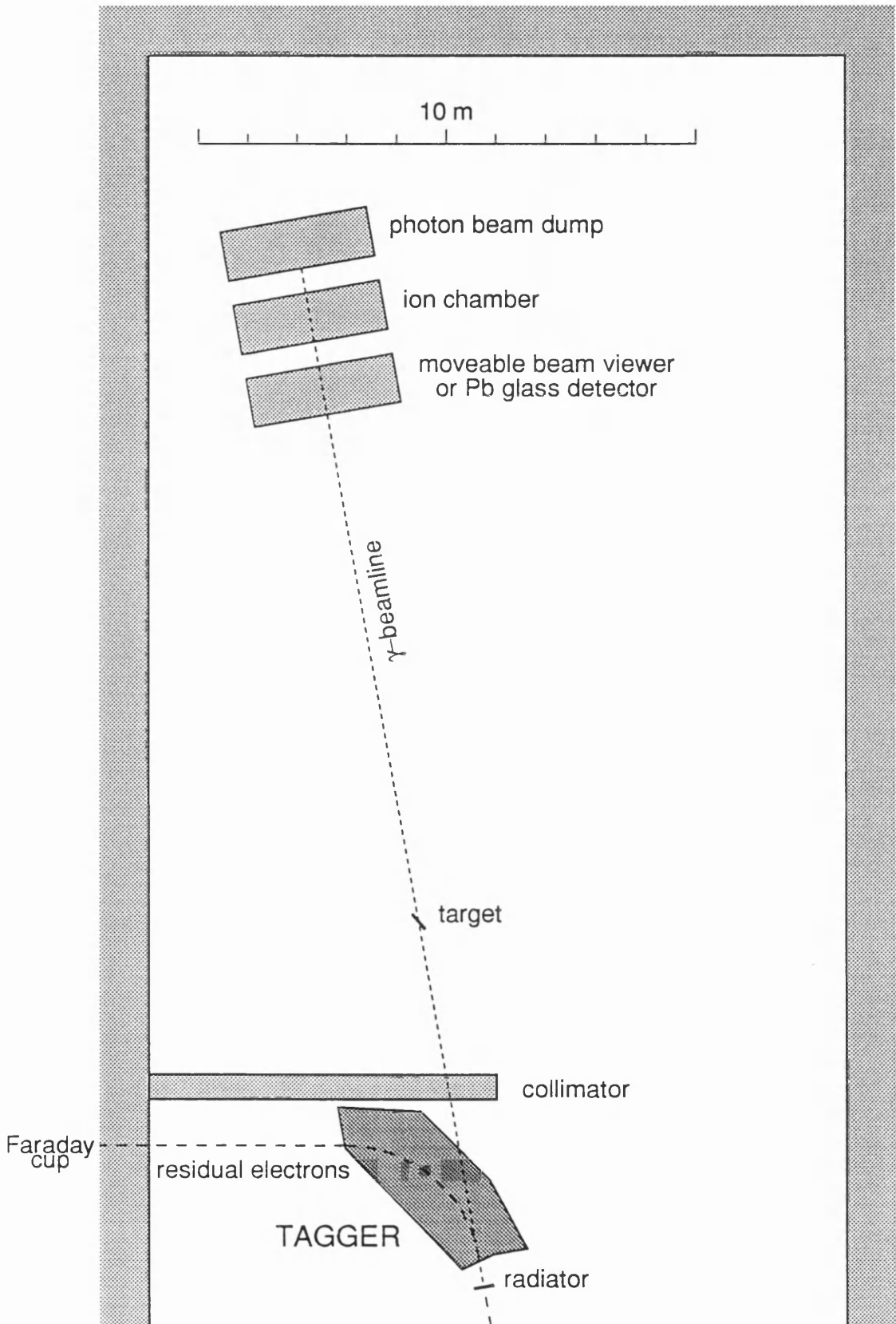


Figure 2.5: Schematic view of the photon beam line

## 2.3 Targets

The choice of carbon-12 as the target for this experiment is chosen more on the basis of practicality. The target in the form of graphite sheet is readily available and easy to handle. No containment nor special support structure are required leaving the monitoring, dismounting and changing of the targets simple and quick. There is an advantage too from the theoretical point of view of using  $^{12}\text{C}$  for the  $(\gamma, pn)$  photoreaction. As Carbon is a light nucleus and the reaction products have little nuclear matter to traverse, thus ensuring that the observed cross section are not dominated by final state effects.

In addition a  $\text{CD}_2$  target is also used during the experiment, the purpose of which is to utilize the deuterium two body breakup reaction to calibrate the proton detector PIP. The number of quantities measured by the PIP-TOF detectors together with the Tagger over-determines the two-body breakup kinematics. This allows independent calibration of the two detectors and also mutual cross-checking of the calibration itself. For example, from the two-body kinematics, the neutron energy can be calculated using the measured photon energy from the Tagger and proton polar angle from PIP. This calculated neutron energy is then compared with the measured neutron energy from TOF. Similarly the measured proton angle can be cross checked using the measured photon energy and the neutron angle (see Calibration). Both targets are mounted on a mechanical ladder driven by a stepping motor which could be controlled remotely.

The thickness of the target was a compromise between high count rate which favours a thicker target, and low ionization losses by the charged reaction products as they emerge from the target which favours a thin target. The angle of the target to the beam is also a compromise between large ionization losses which will give large uncertainty in the energy of the emitted proton, and large photon

beam spot which will result in a large uncertainty in the proton angle. For this experiment PIP was placed in three different positions and the two corresponding target angles used are shown in figure(2.6). The energy lost from a 50MeV proton

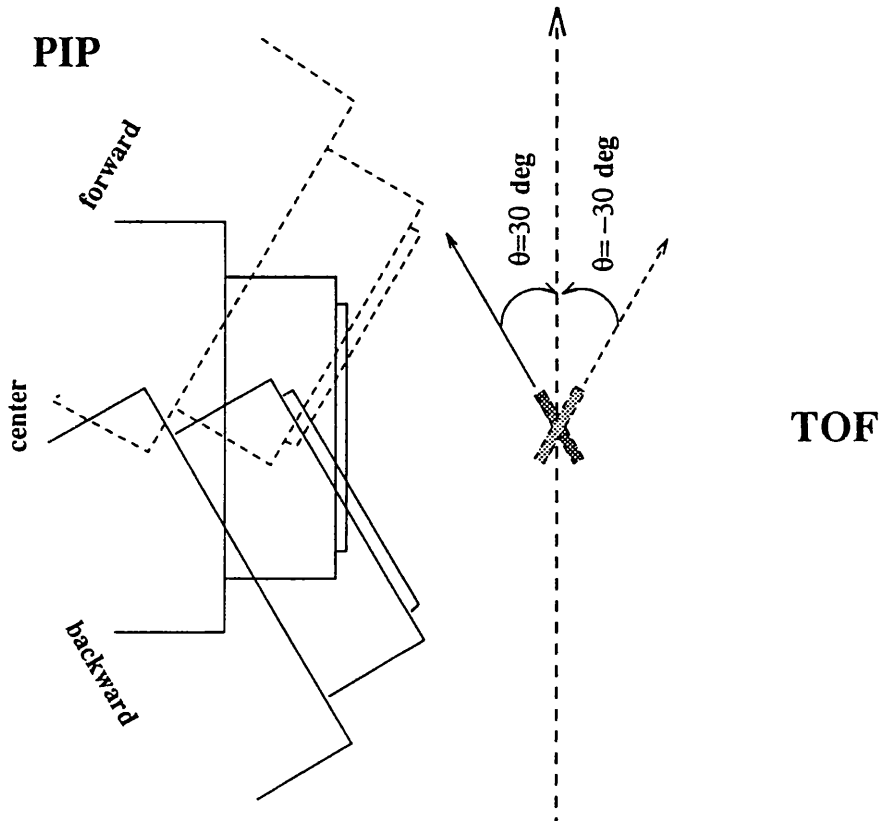


Figure 2.6: Target orientations; target angle for  $\theta = -30^\circ$  was used with PIP at Forward angle, while  $\theta = +30^\circ$  was used at Central and Backward angle.

after traversing through 2mm of  $^{12}\text{C}$  is  $\sim 4\text{MeV}$  giving an uncertainty of  $\pm 2\text{MeV}$ . The maximum contribution from the target size to the angular uncertainty at 50cm away with the target at  $30^\circ$  and a beam spot of diameter  $\sim 1.5\text{cm}$  is  $\sim 0.6^\circ$ .

## 2.4 Particle Detectors

PIP and TOF were designed primarily to study the various aspects of  $(\gamma, NN)$  and  $(\gamma, \pi N)$  reactions. The detector requirements for these studies include:

- Good Particle Identification:

Need to distinguish the various reaction products such as  $e$ ,  $\pi$ ,  $p$ ,  $n$  and  $d$  so that the  $(\gamma, pn)$  channel can be isolated.

- Good Energy Resolution:

Must be sufficient to resolve the different shells of the nucleus. In light nuclei this requires a missing energy resolution of  $\sim 10\text{MeV}$ .

- Good Angular Resolution:

Theoretical calculation predicts the angular distribution of the  $^{12}\text{C}(\gamma, NN)$  reaction to vary smoothly over a large range of angles. A resolution of a few degrees is therefore sufficient for a good comparison with theory.

The various parts of the PIP-TOF detector systems are described below with their specification and layout in the experimental hall.

### 2.4.1 Start and Veto $\Delta E$ Detectors

A segmented layer of thin plastic scintillators  $\Delta E$  surrounds the target at a radius of  $\sim 11\text{cm}$ , figure(2.7). There are seven segments on each side of the beam. At the forward angle the widths of the segments are smaller. This reduces the count rate in the forward segments which are exposed to a larger flux of reaction products mainly from atomic processes.

The set of  $\Delta E$  detectors on the PIP side of the beam,  $\Delta E_{start}$ , is one of the most important parts of the experiment. Due to its close proximity to the target, a coincidence of a  $\Delta E_{start}$  signal with PIP is almost certain to have been caused by a charged particle coming from the area around the target. This coincidence was used as a 1<sup>st</sup> level trigger for the experiment. Also the timing of this  $\Delta E_{start}$  signal is closely correlated with the timing of the photoreaction, hence it is used as the 'start' signal for all the time-to-digital convertors. For each angular setup

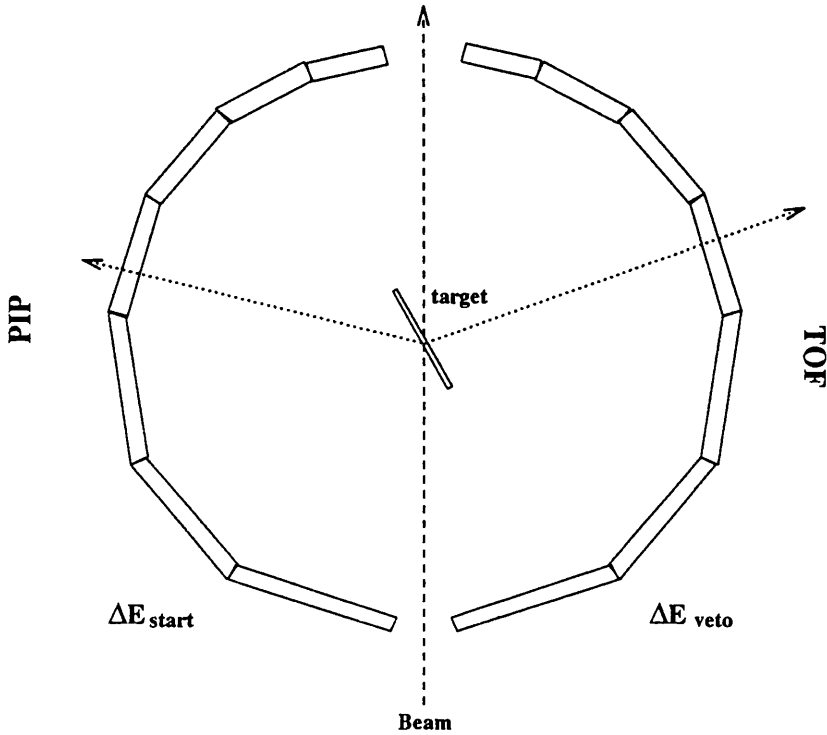


Figure 2.7: A schematic diagram of the  $\Delta E$  ring.

only four of the seven  $\Delta E_{start}$  elements which covered the angular range of PIP were used in the trigger.

The  $\Delta E$  detectors on the TOF side,  $\Delta E_{veto}$ , are used for particle identification. During the  $(\gamma, NN)$  experiment the electronic trigger demands a signal from the TOF detector disregarding the  $\Delta E_{veto}$ . During off-line analysis if a signal is present in any part of  $\Delta E_{veto}$  then it will be classed as a charged particle, otherwise it is classed as a neutral particle.

## 2.4.2 PIP

PIP is a charged particle detector specifically for the detection of pions and protons. In this experiment it is used for detecting protons. It has a five layer segmented structure, made from plastic scintillator of the type NE110 figure(2.8). The front layer consists of four vertical scintillators ( $\Delta E_2$ ) each of dimension 0.2

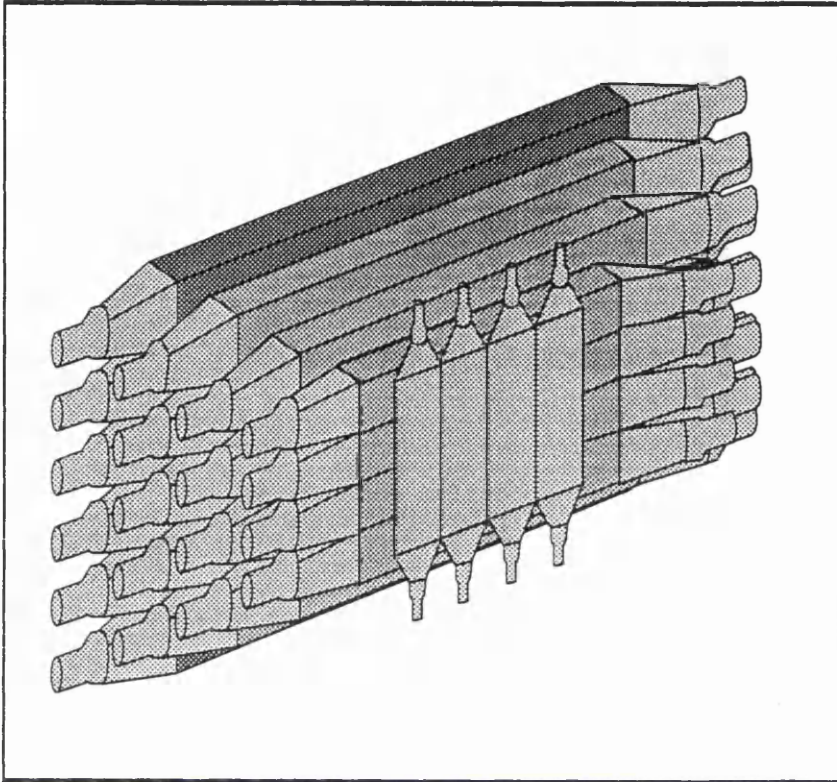


Figure 2.8: A schematic diagram of PIP

$\times 42 \times 20\text{cm}^3$ . This is followed by four horizontal banks of successively larger E layers. These have dimensions shown in table[2.1]. The design allows the solid angle of PIP to be defined by the front  $\Delta E_2$  layer. All the scintillators have a photo-multiplier(PM) tube attached to both ends. To reduce 'end' effects, light guides are included between the scintillator and the PM tube. Each block is individually wrapped to prevent light leaks. The whole structure is boxed in a 5mm steel casing and is supported by a steel framework. The wall of the casing acts as a barrier against low energy charged particles and also as another defence against light leaks.

E layer	no of blocks	block L×D×H (cm)
E1	4	100 × 11.0 × 13.5
E2	4	130 × 17.5 × 17.5
E3	5	160 × 17.5 × 17.5
E4	6	190 × 17.5 × 17.5

Table 2.1: *Dimensions of the PIP E blocks*

### 2.4.3 TOF

This is an array of 96 NE110 plastic scintillators. It is primarily for the detection of neutrons and protons using the time-of-flight technique. Each scintillator has dimensions  $300 \times 20 \times 5\text{cm}^3$ , with a PM tube attached to both ends of each bar, figure(2.9). TOF can be arranged in 12 separate stands with 8 bars of scintillators to one stand. This design makes the TOF detector very versatile, allowing it to cover selected phase space for different experiments. In this experiment four stands are grouped together as shown in figure(2.10) to increase the neutron detection efficiency. Since the neutron is uncharged it cannot produce ionisation in the scintillator directly and detection relies on neutron reactions, such as proton knockout reaction, which then produces ionisation. Such reactions could occur anywhere along the neutron's path through the scintillator. The thickness of the scintillator thus puts a limit on the neutron energy resolution via the uncertainty in the neutron's flight-path, resulting in uncertainty of the neutron's time-of-flight.

### 2.4.4 Experimental Setup

In order to get the maximum angular coverage without compromising too much on detector resolution the experiment has to be done in three stages. The setups

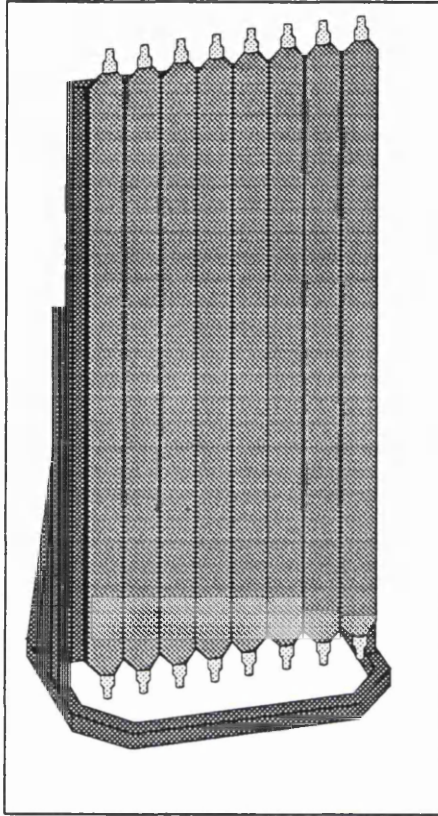


Figure 2.9: *Schematic diagram of a TOF stand.*

are shown in figures(2.10,2.11,2.12).

In earlier experiments [8],  $^{12}\text{C}(\gamma, NN)$  breakup has shown strong back-to-back angular correlation in the CM frame of the photon and the nucleon pair. The three setups have PIP-TOF placed in a complementary back-to-back geometry with the laboratory frame to maximize the detection of the NN pairs. The  $\Delta E$  ring that surrounds the target is not drawn here. The total polar angle coverage of PIP for the three setups are  $22.7^\circ$  to  $156.7^\circ$  and for TOF are  $10.5^\circ$  to  $153.4^\circ$ . The wide angular coverage allows a good comparison with theoretical predictions of the angular distribution of the  $^{12}\text{C}(\gamma, NN)$  cross section.

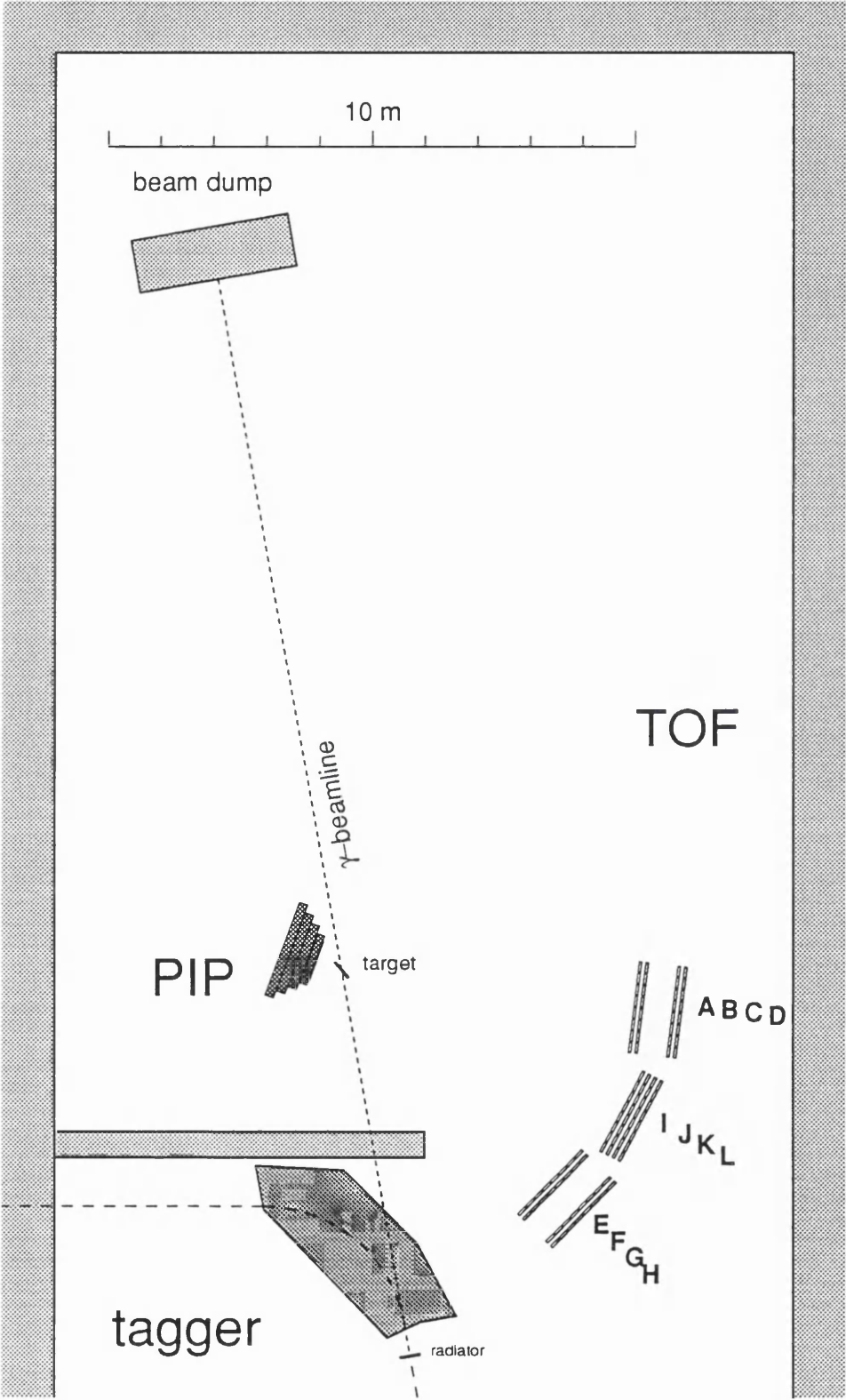


Figure 2.10: Experimental layout for PIP at FORWARD angle.

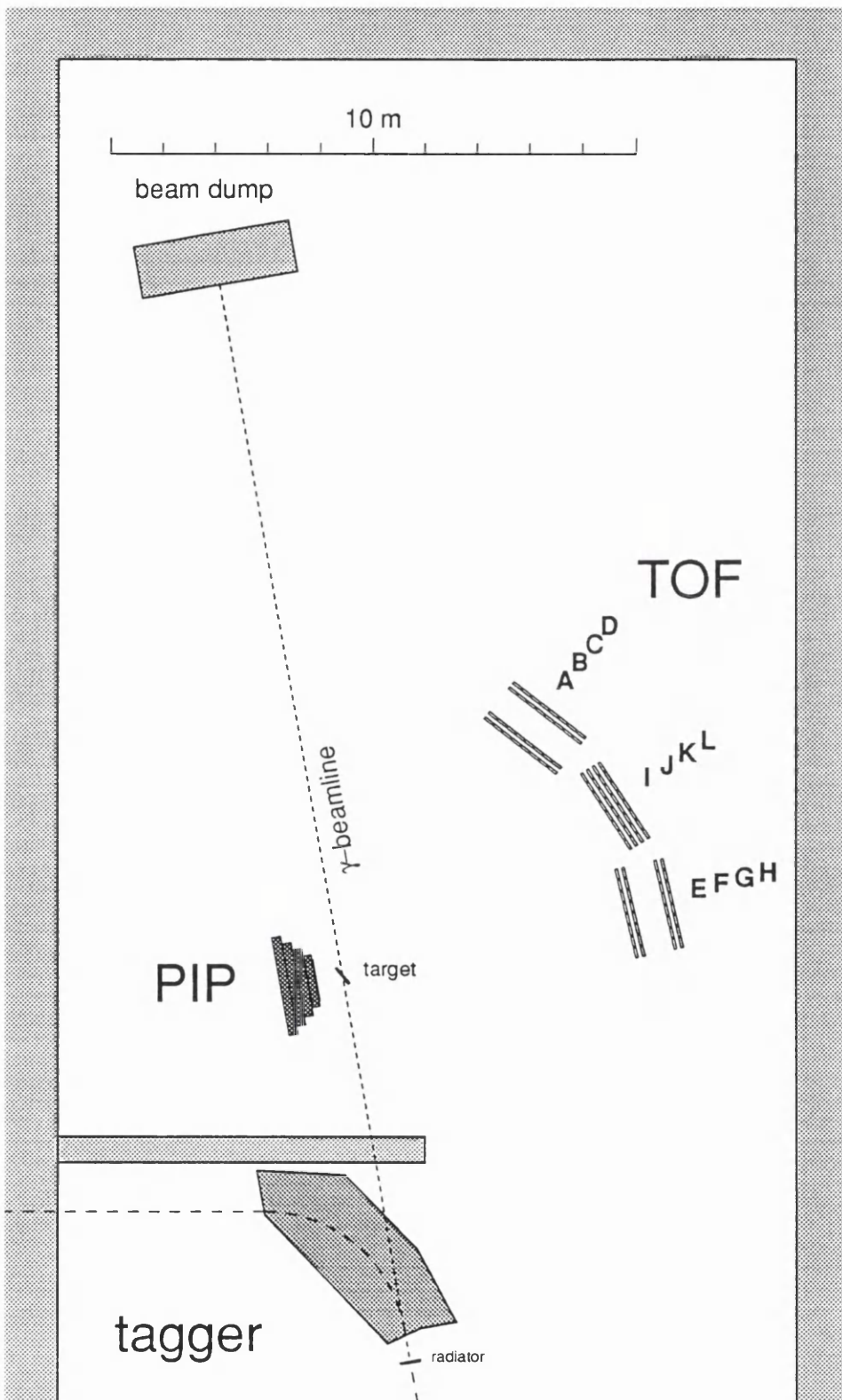


Figure 2.11: *Experimental layout for PIP at CENTRAL angle.*

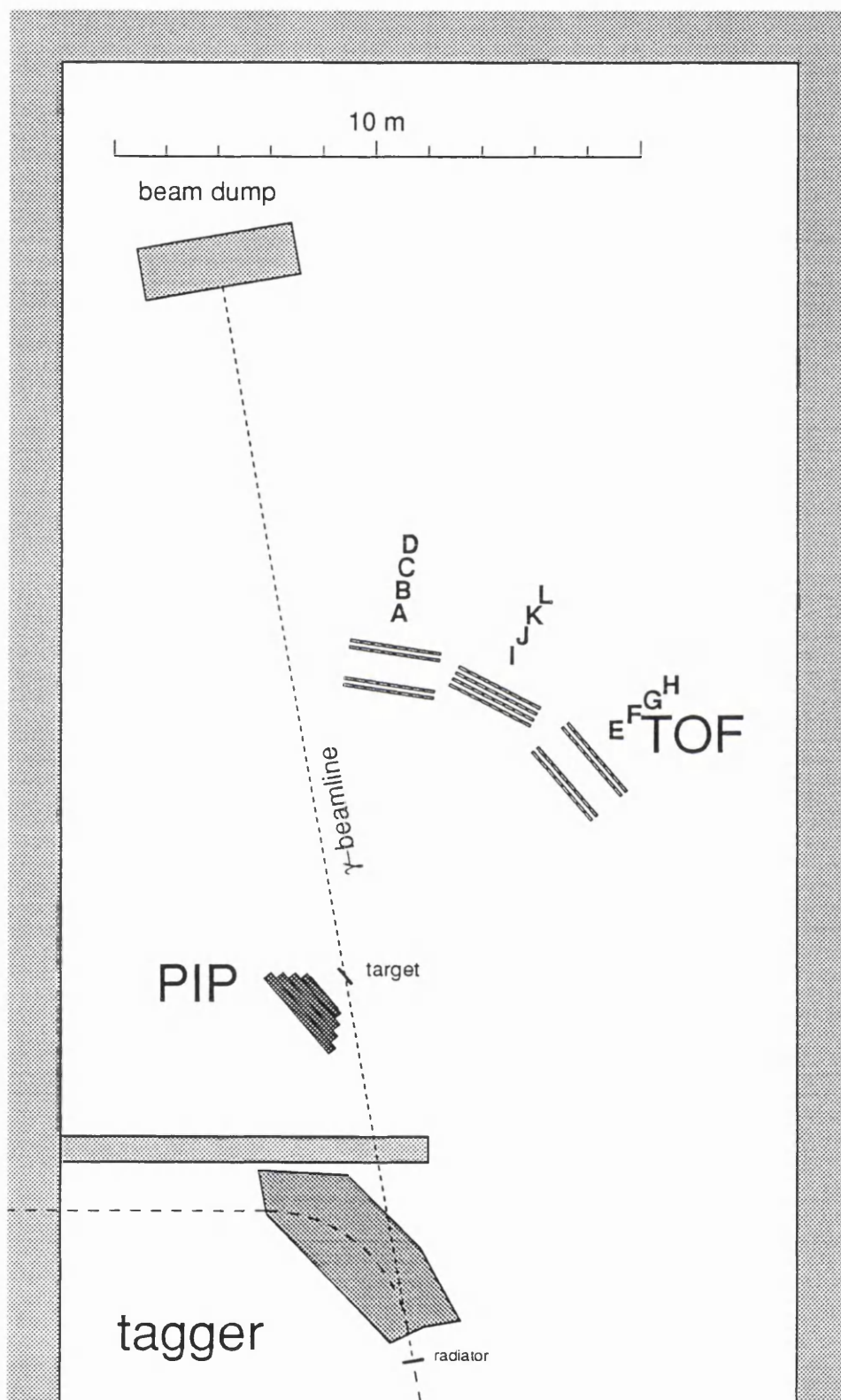


Figure 2.12: Experimental layout for PIP at BACKWARD angle.

## 2.5 Data Acquisition

Amidst the  $(\gamma, NN)$  events that are of interest, there is a background of electrons entering PIP that are caused by atomic processes such as Compton Scattering and  $e^\pm$  pair production. Also there is a large proportion of events ( $\sim 90\%$ ) in which only one particle is detected in PIP and nothing in TOF. Storing all of these events would increase the experimental dead-time and the amount of storage required and would only be thrown out later during off-line analysis. Hence to maximize the efficiency of the data acquisition these background events must be identified and rejected on-line during the experiment. This must be done fast to minimize the experimental dead-time. A system of fast decision trigger logic was devised for this purpose, see section(2.5.4).

### 2.5.1 Event Information

The pulse height signal from a photomultiplier(PM) tube contains both the energy and timing information of the photonuclear event. The timing information is relative to a start time. This start time is provided by the  $\Delta E_{start}$  detector. The above information is sufficient to determine the energies and trajectories of the detected particles.

### 2.5.2 PIP-TOF

To obtain the energy information, the analogue pulse height signals are digitized by Charge-to-Digital Convertors (QDCs). This is done by integrating over the whole pulse with the integration limits (gates) set by the trigger electronics. The QDCs used were the 10-bit Phillips Fastbus 10c2. These are high density modules each housing 32 channels. They have readout thresholds for noise reduction and a fast clear capability for fast triggering [50].

To obtain the timing information the pulse from each PM tube is fed into a leading edge discriminator. This has a preset adjustable threshold. When the pulse from the PM tube rises above the threshold, the discriminator will output a logic pulse. The logic pulse from the 1<sup>st</sup> level trigger which is timed to the  $\Delta E_{start}$  simultaneously starts all the Time-to-Digital Convertors (TDCs). The logic pulse from any PIP-TOF discriminator then provides the stop signal to its associated TDC. The TDCs used were 10-bit Phillips Fastbus 10c6 units. These too are high density modules with 32 channels and fast clear capability. The basic electronics required to do the above tasks is shown in figure(2.13).

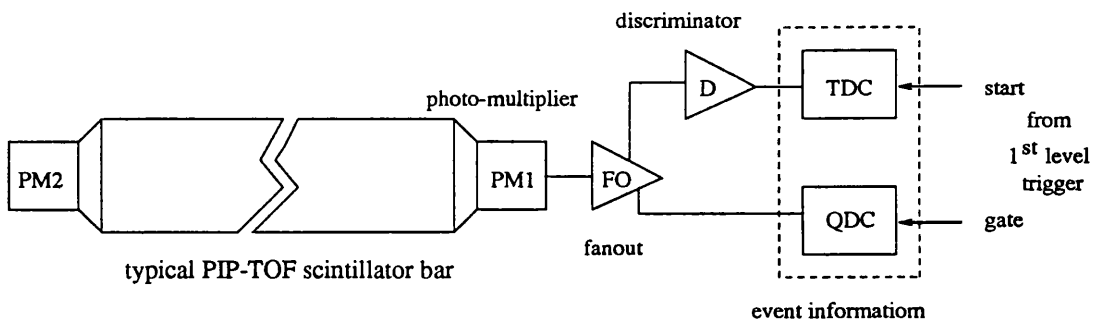


Figure 2.13: Schematic diagram of the electronics circuit.

### 2.5.3 Tagger

For the Tagger timing the 1<sup>st</sup> level trigger provides the common stop signals for all the Tagger TDCs. When an accepted event is identified, 80ns gates are opened on all the 352 TDCs in the Focal Plane Detector (FPD). The individual TDCs get their start signals when an electron is detected in the associated channel in the FPD. The signal from the FPD is timed so that all detected electrons which have undergone bremsstrahlung radiation and is in coincidence with the photonuclear reaction at the target will arrived at the FPD within the 80ns gate. A ‘prompt’

time region within the gate corresponds to an electron detected in the FPD in coincidence with an accepted event detected in the PIP-TOF detectors. The use of 'gated' scalers which in the absence of a stop signal continuously clocks up the number of electrons detected avoiding the need for dead-time correction in determining the photon flux.

#### 2.5.4 Trigger Logic

The trigger electronics were constructed using high density programmable CA-MAC logic and control modules. It allows remote computer controlled setting of discriminator thresholds and more importantly the trigger decoder.

The trigger decoder used is the Lecroy 4508 Programmable Logic Unit (PLU). This unit is the heart of the decision making process. Essentially the unit allows a maximum of eight logic inputs and eight logic outputs. Any combination of the inputs can be selected and programmed to produce any combination of outputs. Here the inputs are the various triggers used and the outputs are used to initiate the various different tasks to be done. The trigger used must be able to select out events of interest which are:

- protons in PIP with an associated particle in TOF.
- cosmic events in PIP and
- TOF flasher events from its LEDs.

The latter two types of events are intended for calibration purposes and gain monitoring.

### 1<sup>st</sup> level trigger: fast triggers

The triggering is split into three levels of decision making. The purpose of the 1<sup>st</sup> level trigger is to make a fast and simple decision. Figure(2.14) shows the trigger inputs to the 1<sup>st</sup> level PLU decoder and the resulting outputs. It has three active

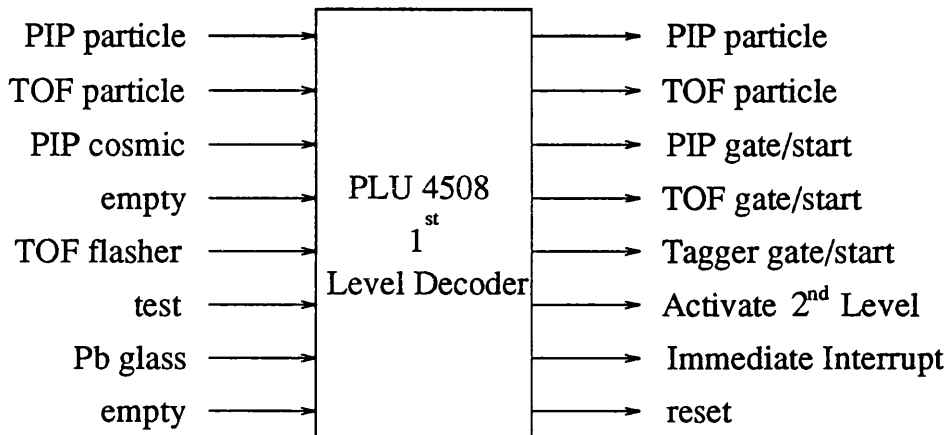


Figure 2.14: *The 1<sup>st</sup> Level, Fast Trigger*

triggers:

- The PIP particle trigger: This identifies charged particles in PIP which originate from the target. This is ensured by demanding a coincidence between the  $\Delta E_{start}$ , the PIP  $\Delta E_2$  and the E1 layer. This is the first stage of the  $(\gamma, pN)$  event selection.
- The cosmic trigger: Cosmic muons can be easily detected by PIP. They are identified by a coincidence of the top and bottom block in both the E2 and E3 layers. For the E1 layer due to its proximity to the target a cosmic trigger is identified by requiring a coincidence of all four blocks in the layer. This ensures that the charged particle entered PIP vertically and is unlikely to have originated from the target. These top-bottom coincidence pattern

are identified by another Lecroy 4508 PLU, figure(2.15). The E4 layer was not used in the cosmic trigger.

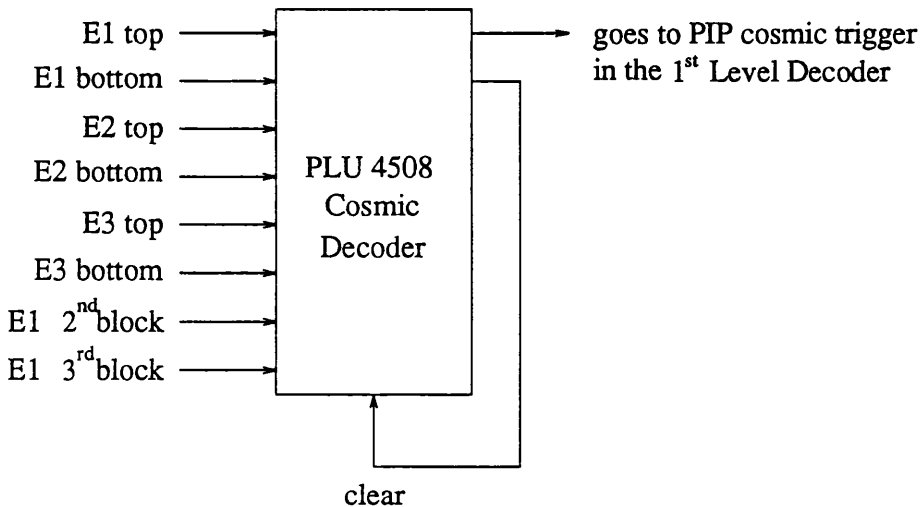


Figure 2.15: *The Sub-1<sup>st</sup> Level, Cosmic Trigger*

- TOF flasher trigger: This is solely for monitoring the stability of the TOF PM tubes. A constant amount of light is flashed to each PM tubes by a Light Emitting Diode(LED). The consistency of the LED output is monitored by a high stability PIN diode [51]. The whole flasher system is driven by an oscillator which also drives the flasher trigger.

The above three triggers are the active triggers used during data taking to provide the inputs for the 1<sup>st</sup> level decoder. Apart from the lead glass trigger which was used for tagging efficiency runs, the rest of the 1<sup>st</sup> level decoder inputs were made redundant. With the arrival of any trigger inputs the PLU is immediately latched(disabled). This prevents further trigger inputs ensuring the events are processed one at a time.

The outputs of the decoder will essentially result in three different tasks.

- When the PIP particle trigger is raised, all the ADCs are then gated so that analogue to digital conversion can begin. The second level decoder is then activated where further decisions will be made.
- When either the cosmic trigger or the TOF flasher trigger is raised then ADC gates are provided to either the PIP or TOF detector respectively. These two triggers are complete on their own and do not required any further decisions to be made. The data acquisition computer is then interrupted and it will proceed with the read out of all the ADCs and TDCs followed by the storage of the event. The ADCs are then cleared and the system reset.
- When more than one trigger is present at the same time then the event is rejected. All the ADCs are fast cleared and the system reset for the next event.

### **2<sup>nd</sup> level trigger : electron reject**

The purpose of the 2<sup>nd</sup> level trigger is to reduce the large background of electrons in PIP produced in Compton scattering of the photons and  $e^\pm$  from pair production. This is done by applying an on-line diagonal cut of the  $\Delta E_2$ -E on a 2-D plot. As electrons and pions have relatively very low stopping powers compared to protons a  $\Delta E_2$ -E plot of the signals from the  $\Delta E_2$  and E1 layers shows the electrons to be located at the bottom left corner. The diagonal cut shown in figure(2.16) is achieved by demanding the weighted analogue sum of the pulses from  $\Delta E_2$  and E1 layers; say  $ay$  and  $bx$  respectively, to be above a certain discriminator threshold. Thus an event is accepted if

$$ay + bx \geq c \quad (2.3)$$

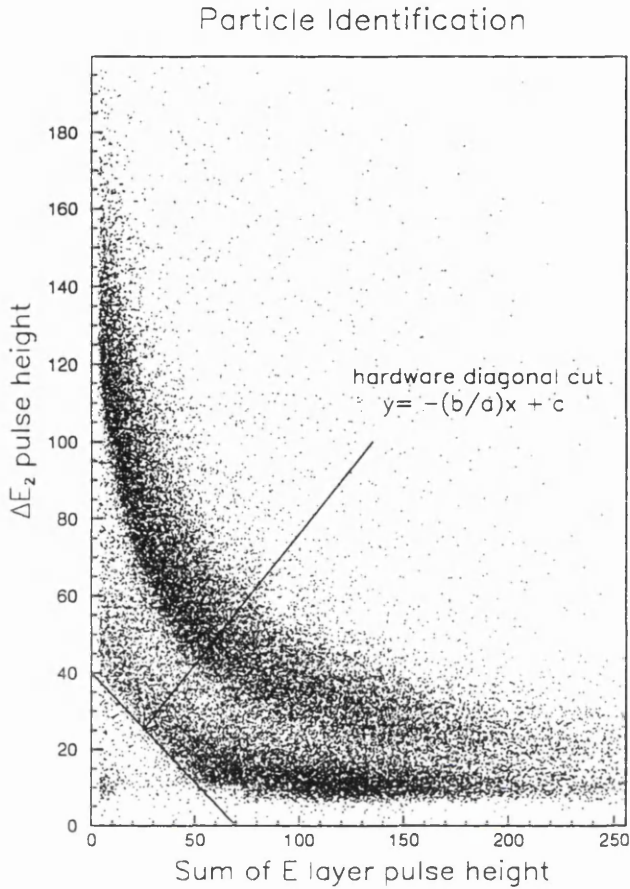


Figure 2.16: Plot  $\Delta E_2 - E_1$  for particle identification.

and the line corresponding to the cut is

$$y = -\frac{b}{a}x + c \quad (2.4)$$

where  $a$  and  $b$  are the weights that determine the slope of the cut. This can be adjusted using attenuators, and the position of the line is determined by  $c$  which is the threshold set on the discriminator.

Just using the  $\Delta E_2 - E_1$  sum alone would cut out some high energy protons that reach the E2 layer so an E1-E2 cut is used to rescue these events. Very high energy protons that reach E3 stand a chance of being cut out by the diagonal cuts. In this case the E3 signal on its own is used to bypass the diagonal cuts. There is also a  $\Delta E_{start} - E_1$  cut included in the trigger. This cut is set more conservatively

than the other diagonal cuts due to the poorer pulse height resolution in the  $\Delta E_{start}$  detectors. Figure(2.17) shows the schematic logic circuit employed to do the above task. If an event satisfies the diagonal cut conditions in the electron-

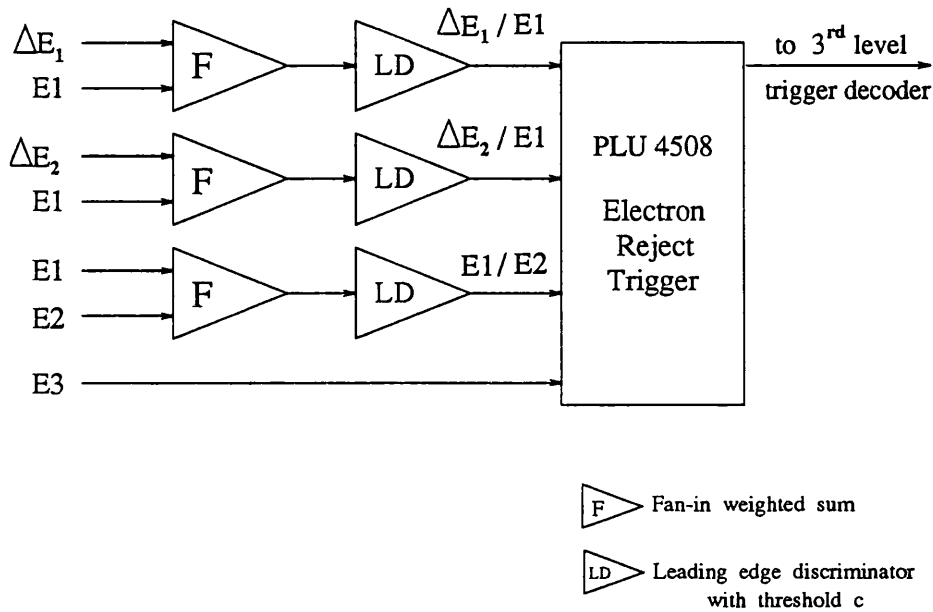


Figure 2.17: The 2<sup>nd</sup> Level: Electron reject logic.

reject PLU one output will be generated and this is used as an input to the 3<sup>rd</sup> level decoder. The diagonal cuts can also remove some high energy pions.

### 3<sup>rd</sup> level trigger : final decision

The purpose of the 3<sup>rd</sup> level decoder, see figure(2.18) is to allow a more stringent condition to be applied in selecting the desired ( $\gamma, pN$ ) coincidence events. It essentially has three active triggers, one for each of the three particles involved:

- Input from the electron-reject decoder.
- TOF-OR trigger; this is a gated OR of all 96 TOF bars. Since approximately 90% of the events have a particle in PIP but none in TOF, this trigger dramatically cuts down on experimental dead-time.

- TAGGER-OR trigger; this is gated OR of all 352 FPD elements. At normal data-taking beam current there is usually at least one electron present within the coincidence gate, but this has little effect on the dead time.

The rest of the inputs to the 3<sup>rd</sup> level decoder are either for test purposes or used for other experiments like the Pion experiments [52] and the Phase-Space Survey experiment [53]. The outputs need to activate only two tasks:

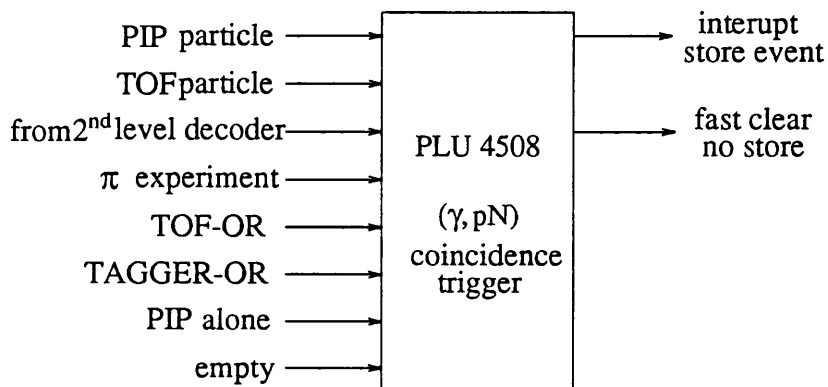


Figure 2.18: *The 3<sup>rd</sup> Level: Final trigger logic.*

- If all three active triggers are raised the output will provide an interrupt signal to the data acquisition computer. All the ADCs are then read out and the event stored. Then the whole triggering system will be reset ready for the next event.
- If any of the three triggers are missing when the PLU is ‘strobed’, ie its bit pattern read out and processed, then the event is rejected and all the ADCs are fast cleared. The whole system is reset and no interrupt will be generated.

For calibration runs like tagging efficiency or CD<sub>2</sub> runs different trigger requirements were used. For the former only the 1<sup>st</sup> level trigger is used and for the

latter, the TOF-OR requirement in the 3<sup>rd</sup> level trigger was withdrawn.

### 2.5.5 Data Acquisition

For compact and efficient storage of data all QDCs and TDCs values are zero suppressed before they are stored, ie the large number of QDCs and TDCs that did not receive a signal are not stored. The acquisition system is run on an Eltec E7 single board computer housing a Motorola 68040 chip running on OS9 operating system. A VME-bus system is used to control the relevant trigger electronics and data transfer to the storage medium is done via an ethernet TCP/IP connection. The control of the data acquisition is done remotely in the control room outside the experimental hall using a console that connects directly to the E7 via the ethernet. The adjustment of discriminator thresholds and more importantly trigger logic requirements for PLUs are done via the console. It also controls the high voltage power unit to all the PM tubes and the stepping motor which drives the target housing. With this degree of control, calibration runs using the CD<sub>2</sub> target or cosmic runs could be carried out without the need to turn off the photon beam and enter the experimental hall. A DEC-VAX work station is used for the initial storage of the data onto disk. This is then transferred onto exabyte tapes. The work station allows an on-line preliminary analysis and monitoring of the incoming data. The effects of the electron-reject triggers can be seen immediately on the work station, and fine-tuning on the diagonal cuts can be done using the console. The software for the on-line analysis is written in 'C'. It contains routines primarily designed to examine and monitor the workings of all the detectors, allowing an overview of the progress of the experiment. A more thorough and sophisticated set of routines were used for the later off-line analysis.

## **Chapter 3**

# **Detector Calibration**

## Introduction

The information given by the QDCs and TDCs are all in the form of channel numbers. To obtain useful physical quantities from these, all the detectors must be calibrated. Dedicated calibration runs are needed to calibrate some aspects of the detectors. The methods used to carry out these calibration runs and the techniques used in extracting the required calibration parameters are discussed in this chapter.

### 3.1 Pedestal Subtraction

There is a constant DC input current in each of the QDCs used in the PIP-TOF detectors. Even if there is no signal present in a particular QDC (when an event has been accepted) the input to that QDC will still be integrated over the set gate time. The resulting integrated charge gives rise to a ‘pedestal’. In a data taking run a readout threshold is set slightly above this pedestal to suppress the storage of these null signal QDCs, saving processing time and storage space. Special pedestal runs are done with all the readout thresholds removed so that all PIP-TOF QDCs are readout and stored. Some contain pulse height information but most just contain the pedestal value,(figure 3.1).

For a pulse from a particle in a detector, the true pulse amplitude  $x$  (in channels) is equal to the QDC value  $Q$  minus its pedestal,  $ped$ :

$$x = Q - ped \quad (3.1)$$

### 3.2 Discriminator Thresholds

The discriminator thresholds set the hardware acceptance of the detectors. Their purpose is to weed out low energy background and electronic noise. They are

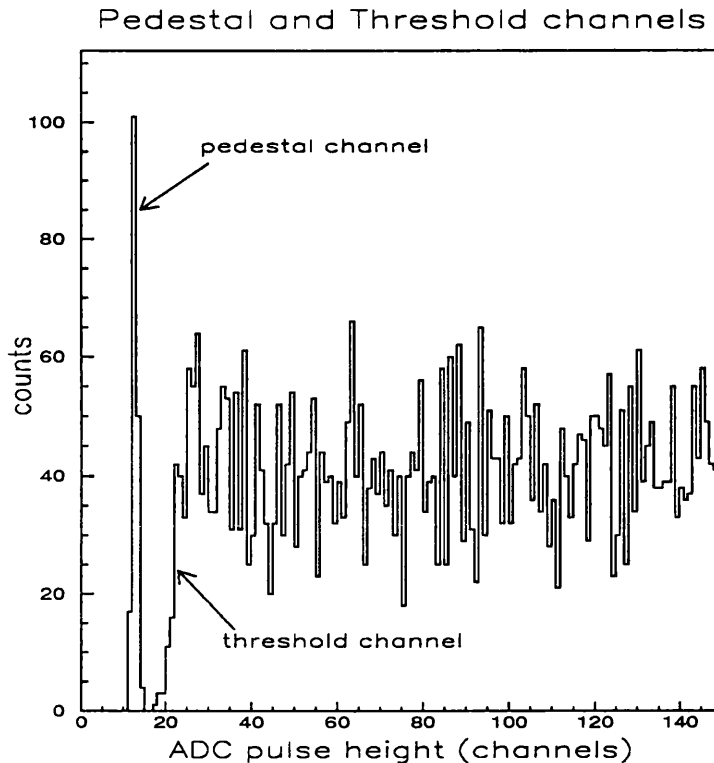


Figure 3.1: *Pedestal and readout threshold; combined plot of two separate runs showing the relative position of the pedestal and threshold channels.*

set as low as possible to widen the acceptance of the detectors for low energy particles. The timing of the STOP signal in all the PIP-TOF TDCs are affected by the 'walk' effect in the Leading Edge Discrimination (see walk below). One of the parameters required to make a correction to the walk is the pulse height threshold of the discriminator. The threshold values for each discriminator in PIP-TOF can be determined by plotting the associated QDC pulse height values on the condition that the corresponding TDC does not have a null value i.e. the QDC pulse is greater or equal to the threshold. The threshold channel of the associated discriminator is easily read from such a plot. Figure(3.1) is a combined plot of a pedestal run and a threshold run, showing their relative position (channel values) in a typical QDC spectrum.

### 3.3 Walk Correction

In all the PIP-TOF detectors the TDC stop signals are generated when the pulse height signal from the PM tubes rises above the associated discriminator threshold. Leading edge discriminators were used for reasons of low cost and high channel density. The stop signals they produce have a small pulse height dependence called ‘walk’. Figure(3.2) illustrates this dependence. As the time profile of

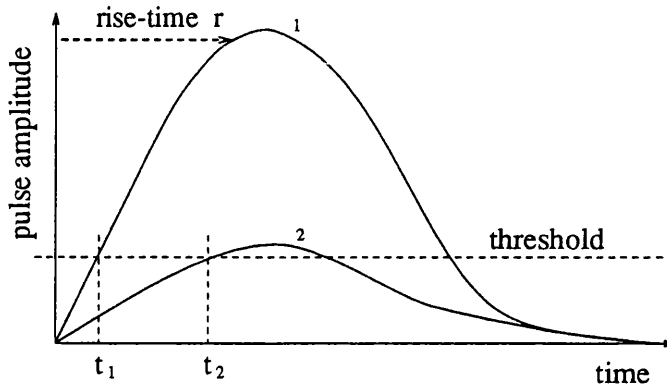


Figure 3.2: *The effect of ‘Walk’*

the pulse is approximately parabolic and independent of amplitude, the effect is that larger pulses reach the threshold at an earlier time than a smaller pulse even if both start at the same time. This causes the discriminator to produce a logic signal at an earlier time for a larger pulse (pulse 1). Based on the work of Annand [54, 55], this walk effect can be corrected with the following parameterization

$$t_{corrected} = t + r \left( 1 - \sqrt{\frac{a_o}{a}} \right) \tag{3.2}$$

where  $a$  is the measured pulse height from the associated QDC,  $a_o$  is the discriminator threshold and  $r$  is the rise-time defined as the time for a pulse to go from 10% to 90% of its maximum height. For each TDC its associated discriminator threshold  $a_o$  is fixed leaving  $r$  as the only free parameter. To obtain the rise-

time  $\tau$  of the pulses produced by various detector elements requires a variety of different techniques.

The rise-time for each start-detector element can be established by plotting its analogue sum QDC *vs* any one Tagger TDC. The Tagger uses high/low dual threshold discriminators which exhibit negligible walk. A plot of the pulse height from a start detector *vs* a Tagger TDC is shown in figure(3.3). The Tagger TDC

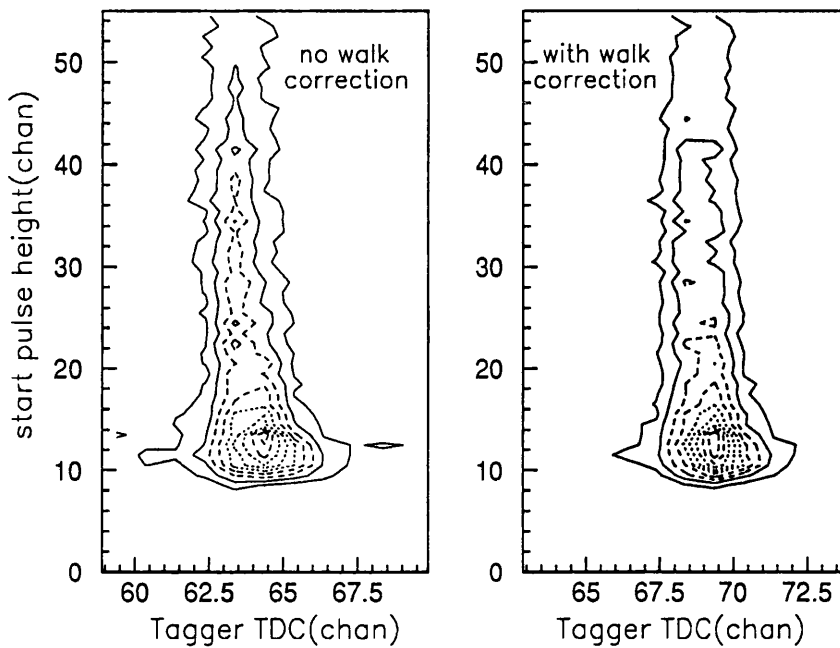


Figure 3.3: Walk correction to the  $\Delta E_{start}$

value recorded depends on the walk in the start detectors, the transit time of the photon from the radiator to the target and the time the associated bremsstrahlung electron takes to reach the Tagger FPD. The latter two are assumed constant since the photon and the recoil electron are relativistic. There is also a small dependence on the energy of the charged particle produced in the target, since a finite time is required for the charged particle to reach the start detector. This variable flight time must be accounted for before the correct walk rise-time can

be obtained. To do this a first order energy calibration was estimated using two body kinematics with data from a deuterium target (see energy calibration below). Protons were selected using the  $\Delta E_2$  vs E pulse height plot, figure(3.4). See also figure(2.16). Once the energy of the proton is known its flight time

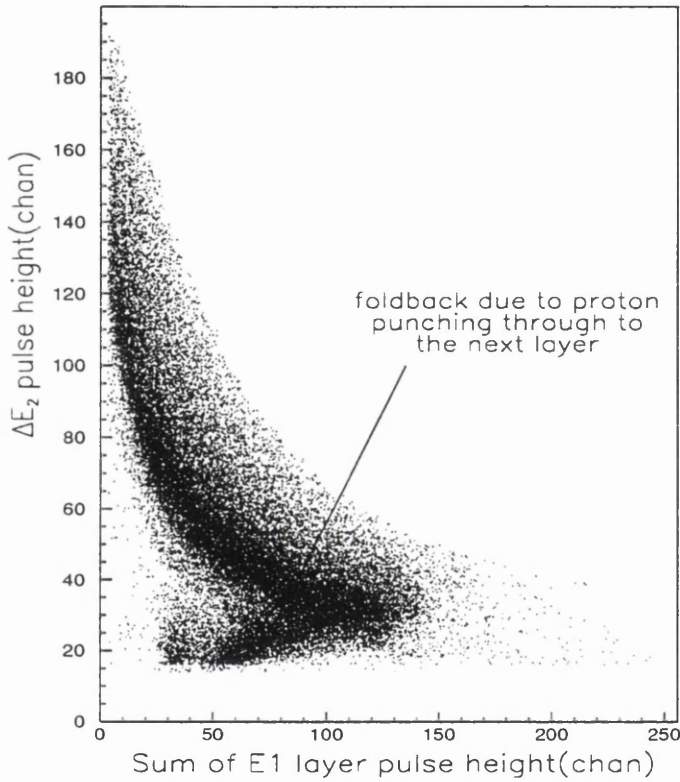


Figure 3.4: *Proton selection*

$\Delta t_{flight}$  can be deduced. The variation of  $\Delta t_{flight}$  for proton energy from 25MeV to 150MeV is  $\sim 0.3$ ns. The remaining effect in figure(3.3 left) is due solely to the walk. The start detector rise-time is then adjusted to minimize the walk. A rise-time of typically 3.5ns was found, and the walk corrected timing is shown in figure(3.3 right).

The rise-times for the rest of PIP were estimated using plots of the mean PIP TDC values vs their associated mean QDC values [56]. The TDC values were

corrected for the proton flight time from the target to each element of PIP and for the light propagation time in the scintillator to the PM tubes. To calculate the latter an effective velocity along the scintillator was determined from the TDC time difference spectrum (see position calibration). Rise-times of  $\sim 6$ ns were found for the E1 layer.

For the TOF walk corrections, a special calibration was carried out where the intensity  $a$  of the LED flasher unit was varied over the dynamic range covered by the QDC. The LED unit also triggers the TOF TDC start. The variation of the TDC signals with the flasher intensity are solely due to the walk. A plot of TDC *vs*  $\sqrt{a}$  has gradient  $\sqrt{r^2 a_o}$ , where  $a_o$  is the known TOF pulse height threshold [57].

### 3.4 Start Detector

The start detector  $\Delta E_{start}$  has several purposes. One is to measure the relative timing of the reaction products w.r.t the Tagger FPD signals so as to optimize the separation of ‘prompt’ and ‘random’ events. Another purpose is to provide a reaction start time for the time-of-flight for the particle detected in TOF. For both of these purposes corrections  $t_{start}$  are applied which have three contributions; the walk  $\Delta t_{walk}$ , the proton flight time  $\Delta t_{flight}$  (see above), and  $\Delta t_{align}$ , which is the alignment of all  $\Delta E_{start}$  elements. For each  $\Delta E_{start}$  element the start time is

$$t_{start} = \Delta t_{walk} + \Delta t_{flight} + \Delta t_{align} \quad (3.3)$$

To obtain the  $\Delta t_{align}$  parameters for the Tagger, one Tagger channel is used and its TDC value is plotted for each of the  $\Delta E_{start}$  elements given the condition that only that particular element has a signal. To obtain the  $\Delta t_{align}$  parameters for the TOF detector, the same method is used as for the Tagger. Here a single TOF bar is used and the mean of its TDCs is plotted for each  $\Delta E_{start}$  element.

The reference point is the position of the ‘gamma flash’ peak, which is due to relativistic particles caused by atomic scattering processes (see T-zero calibration below).

## 3.5 Tagger

The energy of the electron detected in the Tagger corresponds to its hit position along the FPD. The energy associated with the electron’s trajectory was calculated [58] using the spectrometer’s magnetic field profile, which is accurately mapped and the field strength is measured by a NMR probe, set up permanently inside the spectrometer. Given the initial electron beam energy of 855MeV and the measured final bremsstrahlung electron energy on the FPD, the photon energy is then the difference of the two values.

The TDC spectrum of all the 352 elements of the FPD has a coincidence peak which is due to the detected electron being correlated with the photonuclear reaction detected in PIP. Figure(3.5 left) shows an aligned spectrum of the OR of all 352 Tagger TDC spectra. Applying the start time  $t_{start}$  correction the aligned Tagger TDC spectrum can be sharpened further giving a better prompt to random ratio as shown in figure(3.5 right).

## 3.6 PIP

### 3.6.1 Position Calibration

When a particle enters a scintillation block the timing from each of the TDCs connected to PM tubes at either end will have contribution from the start time  $t_{start}$ , cable delay time  $t_c$ , light propagation time in the scintillator  $t_p$  and the

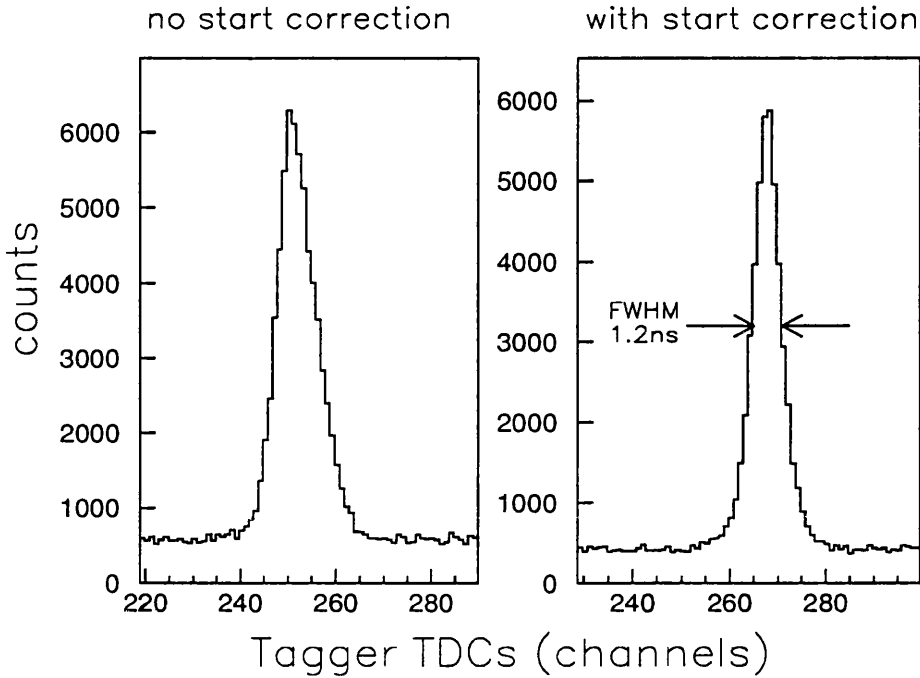


Figure 3.5:  $\Delta E_{start}$  correction to Tagger TDCs

particle flight-time from the target  $t_{flight}$ , so for :

$$TDC1 = t_{start} + t_{c1} + t_{p1} + t_{flight} \quad (3.4)$$

and 
$$TDC2 = t_{start} + t_{c2} + t_{p2} + t_{flight} \quad (3.5)$$

since  $t_{start}$ , and  $t_{flight}$  are the same for both TDCs, taking the difference of the TDCs for a detector block gives:

$$TDC1 - TDC2 = (t_{p1} - t_{p2}) + constant \quad (3.6)$$

and with 
$$\frac{x}{v} = t_{p1} ; \frac{l-x}{v} = t_{p2} \Rightarrow \left( \frac{2x-l}{v} \right) = t_{p1} - t_{p2} \quad (3.7)$$

where  $v$  is the effective velocity of the scintillation light along the block,  $x$  is the hit position along the block and  $l$  is the length of the block, therefore this gives

$$x = m(TDC1 - TDC2) + k \quad (3.8)$$

The calibration parameters  $m$  and  $k$  for each block are found by exploiting the segmented design of PIP. To calibrate each E1 block four time difference spectra were accumulated by demanding a coincidence with each  $\Delta E_2$  block as shown in figure(3.6). The four spectra are then superimposed together figure(3.7 left).

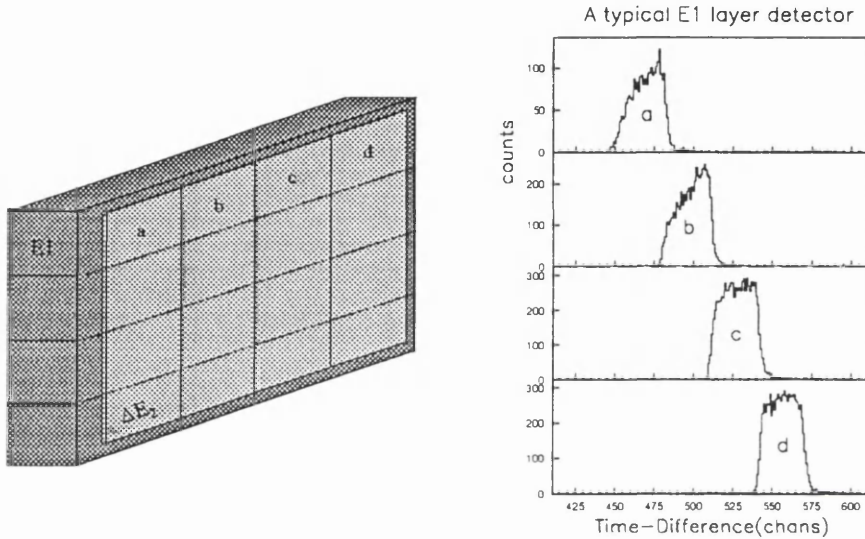


Figure 3.6: *Position calibration method*

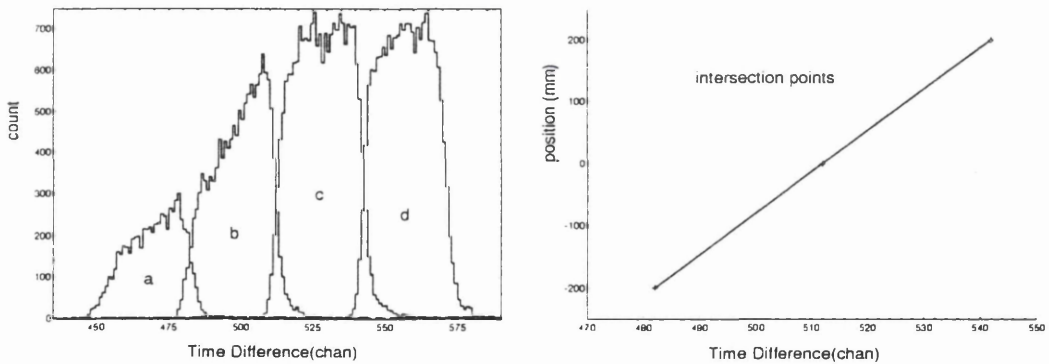


Figure 3.7: *Position calibration parameters*

The centre of overlap then corresponds to the joins between the  $\Delta E_2$  blocks, the positions of which are known. The gradient  $m$  in equation(3.8) can be obtained by a fit to the plot of the position(mm) vs time difference(channels), see figure(3.7 right). The constant  $k$  was chosen so that the centre of each block has  $x = 0$ .

The same method is used for calibrating E2 and E3 layers. Also for the  $\Delta E_2$  layer the same method was used but now demanding coincidence with separate E1 blocks. There is a geometrical effect as illustrated in figure(3.8), plus a slight particle energy dependence which needs to be taken into account. In these cases for the E1 layer there is an  $\sim 11.0$  MeV threshold set on its discriminator, i.e 11.0 MeV of energy is required to be deposited in the E1 layer to generate the TDC STOP. A 30MeV proton will, on average, traverse a range of  $\delta x \sim 5$ mm in depositing 11.0MeV of energy. This results in  $z \sim 202$ mm instead of 200mm which is the effective z dimension of  $\Delta E_2$  strip. Table(3.1) shows other calculations. The

proton energy(MeV)	11MeV threshold range(mm)	effective z(mm)
30	$\sim 5$	202
50	$\sim 8$	203
100	$\sim 14$	205

Table 3.1: *Distance proton traversed into detector before generating a TDC STOP*

maximum proton energy that stops in the E1 blocks is  $\sim 130$ MeV and since the average proton energy is  $\sim 50$ MeV for the photon energy range analysed(120MeV to 400MeV), a constant correction  $\delta z = 3$ mm was used giving z values of 203mm. For the E2 layer the geometrical effect gives  $z' = 252$ mm plus the additional  $\delta z$  of 3mm. The same principle applies to E3. The E4 layer was not used in the present analysis. Protons were selected for all the PIP position calibrations. The value of  $\delta z$  differs markedly with particle types. For the E1 layer, using just protons rather than all events reveals time-difference values to be out by  $\sim 0.2$ ns at the overlap between c and d and between a and b which translates to  $\sim 14$ mm.

With the y and z coordinates of the particle trajectory deduced from  $\Delta E_2$  and E1 blocks respectively and the x coordinate is measured from the target to

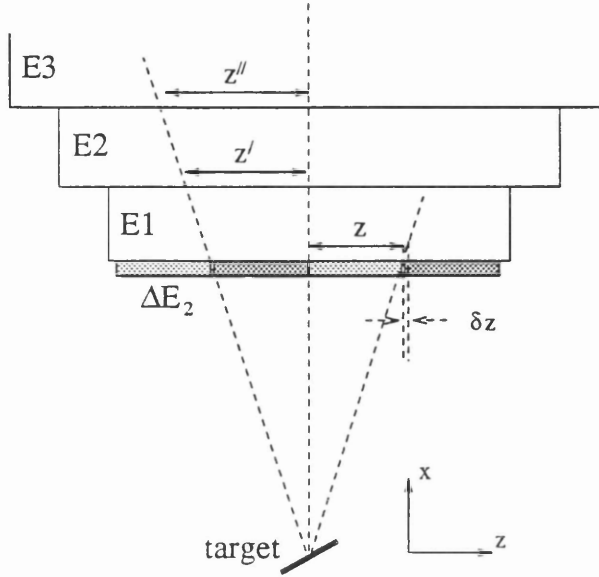


Figure 3.8: Geometrical effect in the Position calibration

the front face of the detector, the three cartesian coordinates were then projected onto the same plane (front face of E1) before they are transformed to obtain the corresponding spherical polar coordinates.

### 3.6.2 Cosmic : Droop Correction and Alignment of Gains

The light  $L$  generated by a charge particle is attenuated as it propagates along the block. The attenuation is approximately exponential so that

$$QDC1 \approx g_1 L \exp^{-\left(\frac{x}{k}\right)} \quad (3.9)$$

$$QDC2 \approx g_2 L \exp^{-\left(\frac{l-x}{k}\right)} \quad (3.10)$$

where  $x$  is position along the block,  $l$  is the length of the block,  $k$  is the decay constant and  $g_1, g_2$  are gains of the PM tubes. Taking the geometrical mean(gmean) will give a good first order position independent pulse height measurement.

$$\sqrt{QDC1 \times QDC2} \approx L \exp^{-\left(\frac{l}{k}\right)} \quad (3.11)$$

$$\Rightarrow \quad gmean \approx L \quad (3.12)$$

There is a residual droop in the gmean that amounts to  $\leq 3\%$  see figure(3.9). This is corrected using a parabolic function obtained from cosmic muon events. A cosmic event is identified when all the blocks in a given layer have signals. Since cosmic muons are minimum ionizing, after correction for the pathlength traversed the average energy deposited will be a constant and independent of position along the bar. Figure(3.9) shows the peak channel cosmic gmean for 13 positions along an E2 block.

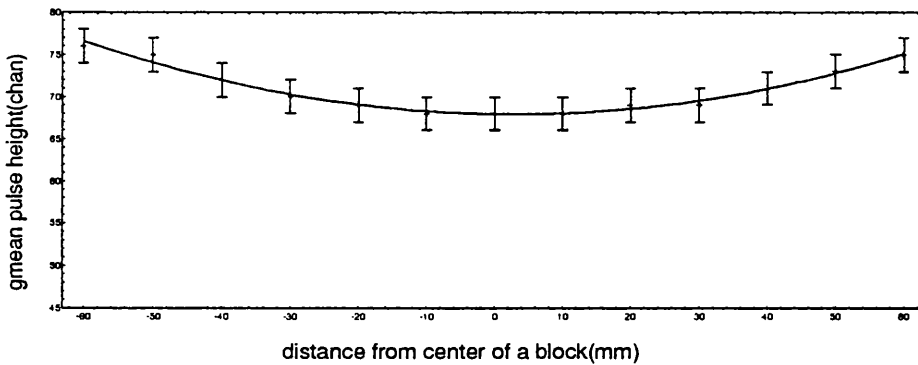


Figure 3.9: *Pulse height attenuation: Droop effect*

The droop corrected cosmic pulse height is used to match the gains of all the PIP blocks. This allows the whole of PIP to be treated as one large scintillator.

### 3.6.3 Energy Calibration

For a charged particle that stops in a plastic scintillator the relationship between the total light output  $L$  and the energy deposited is non-linear due to a quenching effect and has the form

$$L(E) = a_1 E - a_2 (1 - \exp(-a_3 E^{a_4})) \quad (3.13)$$

where  $E$  is the particle's incident energy,  $L$  is total light output, and the coefficients  $a_1, a_2, a_3, a_4$  are particle and scintillator medium dependent. This is known as Birk's law [59, 60]. The quenching effect is particle dependent though it scales simply with particle mass. Consequently equation(3.13) becomes significantly non-linear at incident energies below  $\sim 12\text{MeV}$  for protons in NE110 see figure(3.10). For this experiment the energy threshold in PIP was set at  $\sim 11\text{MeV}$ ,

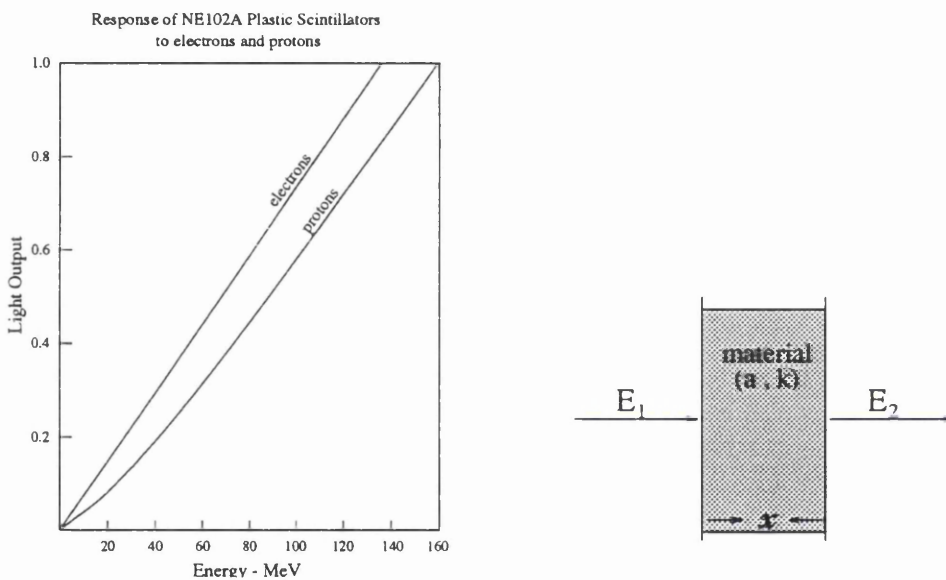


Figure 3.10: *Light output function:Energy loss through a material, plot shows response of NE102A which is similar to NE110 [61].*

any particles with incident energy below that were not measured. Thus the range of measured particles are predominately in the linear range of equation(3.13) which may be approximated as

$$L(E) = a_1 E - a_2 = a_1(E - E_o) \tag{3.14}$$

$$\implies E = a_o L(E) + E_o \tag{3.15}$$

where  $a_o = \frac{1}{a_1}$ . The quenching effect is absorbed in the constant  $E_o$  which together with  $a_o$  is obtained by the calibration process described below.

For a proton to reach PIP it traverses through the target, the air and various scintillator wrappings all of which will cause the proton to lose energy. In a material the range  $R$  traversed by a proton with an initial energy of  $E$  can be parameterized [61] as :

$$R = aE^k \quad (3.16)$$

where  $a, k$  are parameters for various materials. The extra range for a proton of energy  $E_1$  compared to a proton of energy  $E_2$  ( $E_1 > E_2$ ) is given by

$$x = R_1 - R_2 \quad (3.17)$$

where  $R_1$  is the range for energy  $E_1$  and  $R_2$  is the range for energy  $E_2$ . Rearranging the above two equations gives:

$$E_2 = \left[ E_1^k - \frac{x}{a} \right]^{\frac{1}{k}} \quad (3.18)$$

where  $E_2$  is the energy with which a proton of initial energy of  $E_1$  emerges from a material of thickness  $x$ , see figure(3.10). For the thin  $\Delta E_{start}$  and  $\Delta E_2$  transmission detectors the pulse height resolution is relatively poor. So the energy loss within these layers is calculated using the above range method.

The energy calibration in PIP is obtained by using the two body breakup reaction of deuterium,  $D(\gamma, p)n$ . The data is obtained in a separate run with a  $CD_2$  target. With the known photon energy from the Tagger and the measured proton angle, the proton energy from the deuterium breakup can be calculated. All the energy losses of the proton were then taken into account as it emerges from the target until it reaches the front face of E1. This 'calculated' energy  $E_{cE1}$  was then plotted against the measured (droop corrected and gain matched) gmean for particles that stopped in the E1 layer, see figure(3.11). In this figure the pulse height response of all the blocks in PIP are aligned, and if more than one block in E1 registers a pulse above threshold their gmeans are summed together. The calibration parameters in equation(3.15) can then be obtained from the plot.

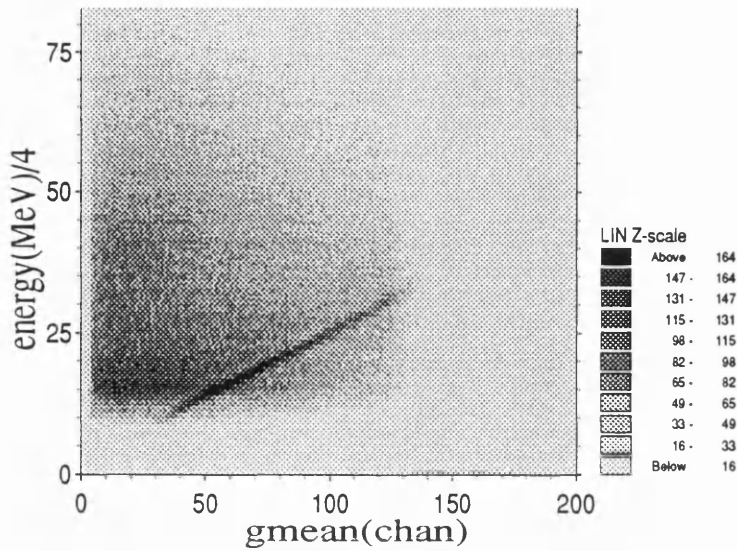


Figure 3.11: *Measured gmean of pulse amplitude vs Calculated energy for protons which stop in the PIP E1 layer.*

To calibrate the E2 layer, protons that stop in E2 layer were selected. The pulse height gmean in all E2 blocks are then summed together and converted into energy using parameters from the E1 layer calibration. Working back to the E1 layer the energy lost in the wrapping between the E1 and E2 layers is added on. The corrected energy is then converted back to an equivalent gmean value and summed with the total gmean of layer E1. A plot of the gmean vs  $E_{cE1}$  is then made and the calibration parameters for the E2 layer can be fine tuned. Using a similar procedure the energy calibration has been extended to the E3 layer, but E4 has not been calibrated as no data from E4 have been analysed. Figure(3.12) shows the result of the above procedure.

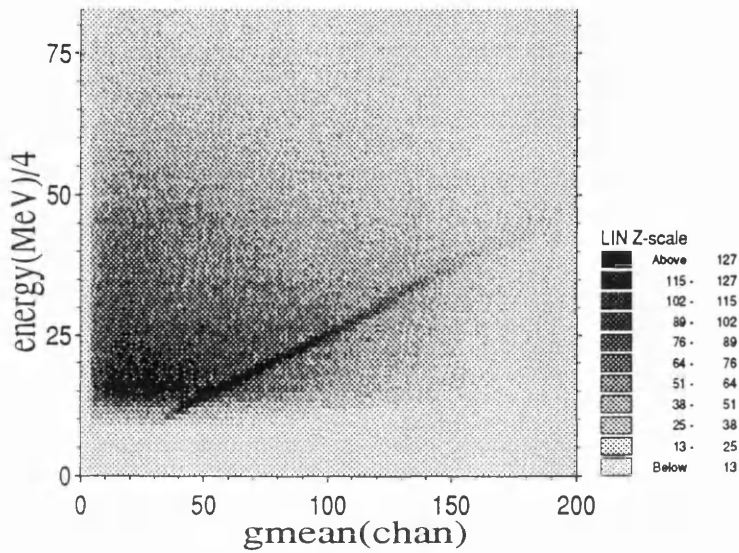


Figure 3.12: Measured *gmean* vs Calculated energy for *E1+E2+E3* layers.

### 3.7 TOF

#### 3.7.1 Position Calibration

The physical position of each bar was measured accurately using an ultra sound device. This gives a good measurement of the polar angle for particles detected in TOF, whose average distance from the target was  $\sim 5.5\text{m}$  in this experiment. The vertical hit position is needed to get the particle flight distance and it is required for bars that are close to the z-axis (i.e. the beam line), to obtain an accurate polar angle. The vertical position along each TOF bar was calibrated simply by taking the half height at both ends of its time difference spectra to correspond to the physical ends of the bar, figure(3.13). A cross check on the position calibration was done by exploiting the asymmetric beam height along the bar as depicted in figure(3.14). A plot of the particle's flight path, shows this asymmetric effect. Two points can be used to cross check the calibration. One, the shortest flight path is at the beam height level and the other point is

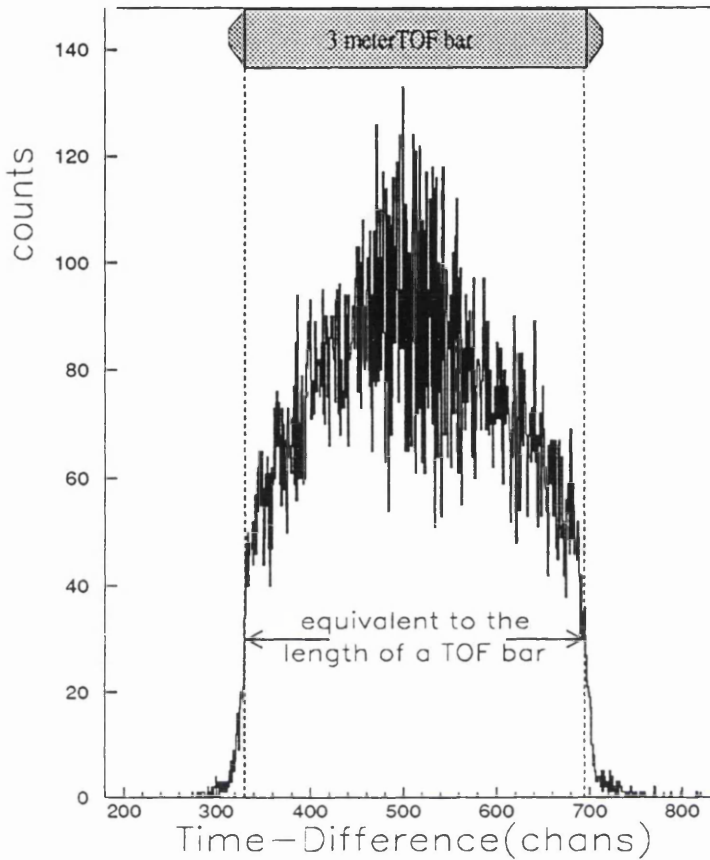


Figure 3.13: *TOF position calibration*

the sudden dip in figure(3.14 left) which corresponds to the flight-path at height  $a$  and  $b$ , since only the portion of the bar above  $a$  can contribute to the larger values of the flight-path.

### 3.7.2 Proton Detection

The TOF side proton selection is done with a cut on a plot of the total pulse height *vs* time of flight for the front layer of each bank of TOF detectors. In order to sum all the pulse heights in the various layers to get better particle selection, the gain of the TOF bars must be aligned. This was done using the 'punch through' point of relativistic charged pions. Since these are minimum ionizing

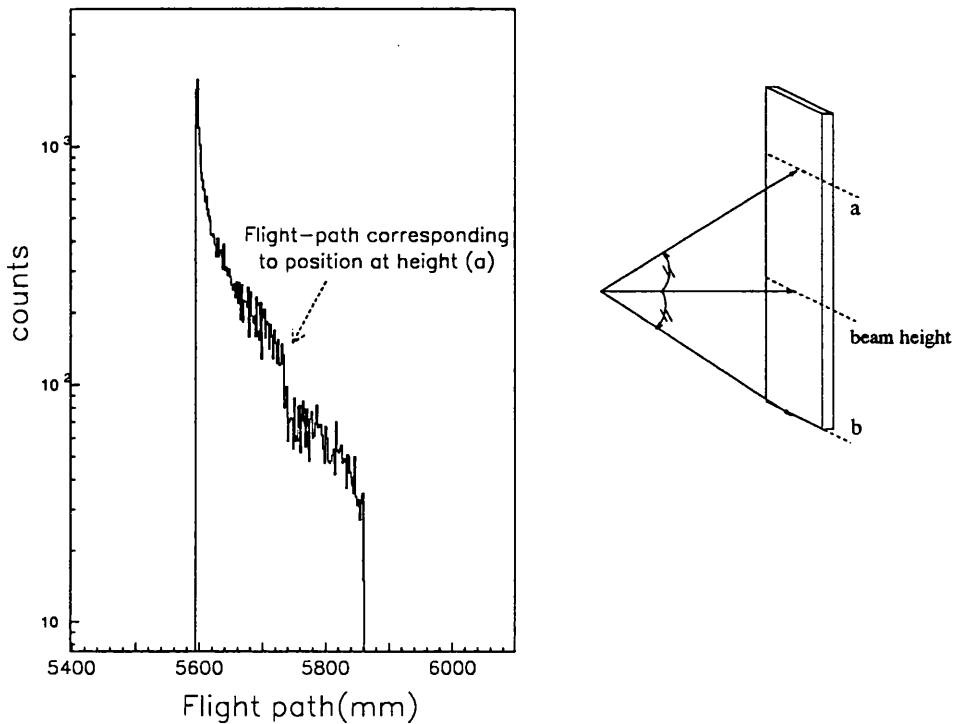


Figure 3.14: *Cross check of TOF position calibration.*

particles the energy they deposit will be same for each bar hence they can be used as a reference point. These pions are selected bar by bar by cutting on the pion ridge, see figure(3.15).

For protons that just punch through a TOF bar the energy deposited is at its maximum. Since the TOF pulse height gains are set comparatively high in order to detect the relatively small pulse height neutron events, protons that deposit large amounts of energy (especially those close to one end of a bar) will cause the corresponding QDC unit to overflow. The data acquisition will then 'see' the content of the QDC as equal to zero. This missing QDC, if not corrected, will cause the event to be thrown away, leaving a depleted region as shown by the circle in figure(3.15). The fraction of events with one or both QDC missing is < 5%.

Since it is the timing information that is used to calculate the proton energy,

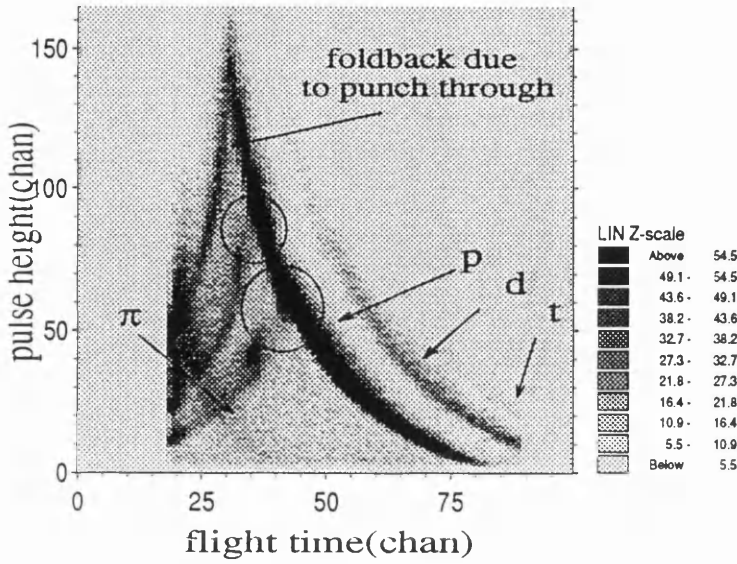


Figure 3.15: TOF charged particle identification

accurate QDC pulse heights are not critical. Hence events with a missing QDC can be ‘rescued’ by estimating the pulse height of the missing QDC. This is done by first assuming the observed pulse amplitude  $a$  falls exponentially with distance  $x$  along a block length  $l$ . The detected pulse height at either end is given as:

$$a_1 = g_1 A \exp\left(-\frac{x}{k}\right) \tag{3.19}$$

$$a_2 = g_2 A \exp\left(-\frac{l-x}{k}\right) \tag{3.20}$$

where  $k$  is a decay constant and  $g$  is the gain of the PM-tubes. With the gains matched and taking the ratio of the above equation gives

$$\left[ \log\left(\frac{a_1}{a_2}\right) \right] \times \left(-\frac{k}{2}\right) = x - \frac{l}{2} \tag{3.21}$$

or  $\implies$  
$$ph = \log\left(\frac{a_1}{a_2}\right) \times ph1 + ph0 = position \tag{3.22}$$

where  $ph1 = -\frac{k}{2}$  and  $ph0 = \frac{l}{2}$ . Using ‘good’ events where  $a_1$  and  $a_2$  and the hit position are known the parameters  $ph1$  and  $ph0$  can be found for each bar by plotting  $(ph - position)$  against  $position$ . Figure(3.16 left) shows the plot for

a typical TOF bar. The slight curving tails at both ends shown are due to the

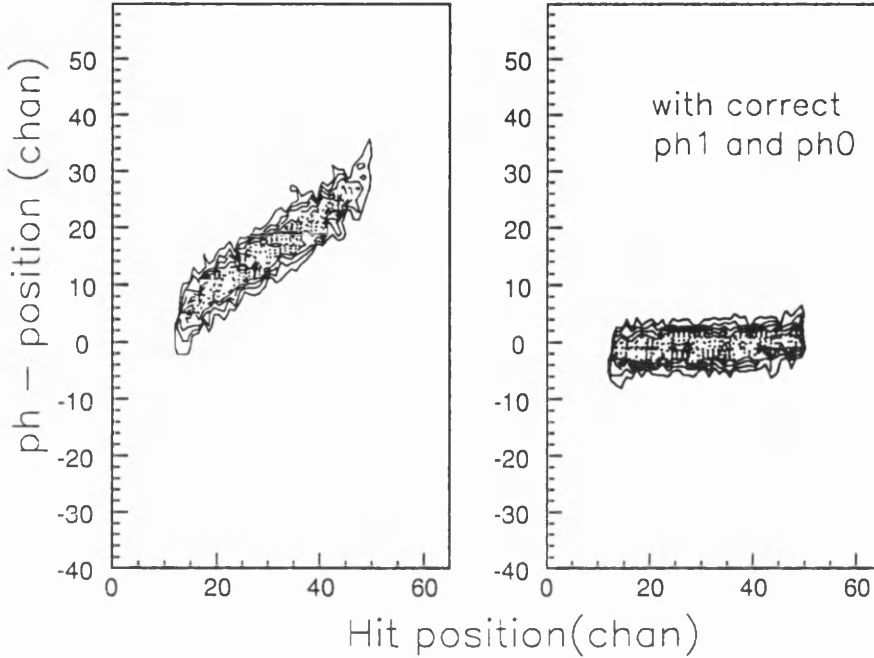


Figure 3.16: *TOF missing QDC correction*

pulse height signal deviating from the exponential assumption above. The value of  $ph1$  is found by adjusting the slope of the ridge until it is horizontal, and the offset  $ph0$  is given by the condition that  $(ph - position) = 0$ . Figure(3.16 right) shows the result plotted with the correct values of  $ph1$  and  $ph0$ .

Since position  $x$  are given by the TDCs, once the parameters  $ph1$  and  $ph0$  are known then if either  $a_1$  or  $a_2$  is missing an approximate value can be found using equation(3.22). With the missing QDC events now retained, the gaps (circled areas of figure 3.15) are smoothed out as shown in figure(3.17).

### 3.7.3 Timing: Channels to ns

The TOF TDC calibrations (channels to nanoseconds) are done using a high precision crystal pulser. The pulser signals are fanned directly into all the TOF

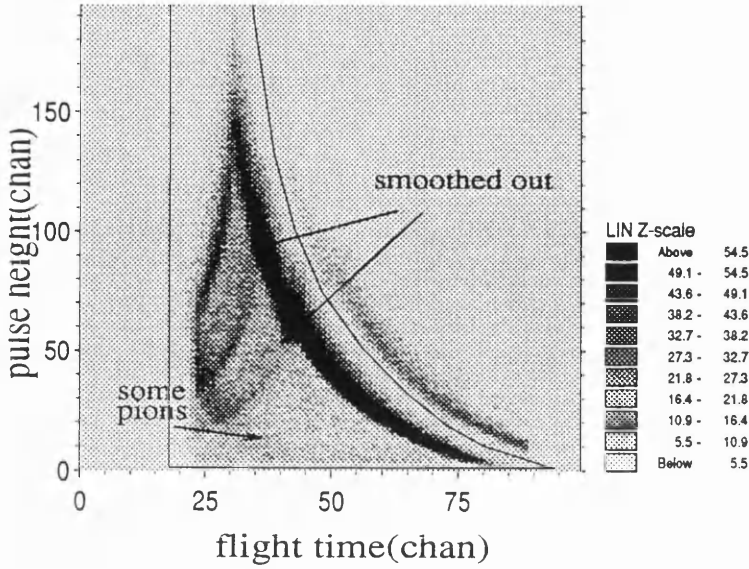


Figure 3.17: TOF charged particle identification: with missing QDC correction.

TDCs. It starts and stops all the TDCs with pulse signals that are precisely multiples of 2.2ns. Figure(3.18 top) shows a typical TOF TDC pulser spectrum, each spike is 2.2ns apart. A straight line fit was obtained for each TDC. The fit was done over the region of possible time-of-flight for our TOF setup.

### 3.7.4 T-zero : Time-of-Flight

The time-of-flight of a particle from the target to a TOF bar is obtained from the mean of its TDCs, using equations(3.4,3.5) above, taking the mean of the TDCs is :

$$t_{mean} = t_{flight} + t_{start} + constant \tag{3.23}$$

$$\Rightarrow t_{flight} = t_{mean} - t_{start} - constant \tag{3.24}$$

where the  $t_{start}$  is given in equation(3.3). Here  $t_{start}$  takes account of the proton flight time to the  $\Delta E_{start}$ , the alignment and walk correction of the  $\Delta E_{start}$ (see start-detector). The constant in the equation is due to cable delays and signal

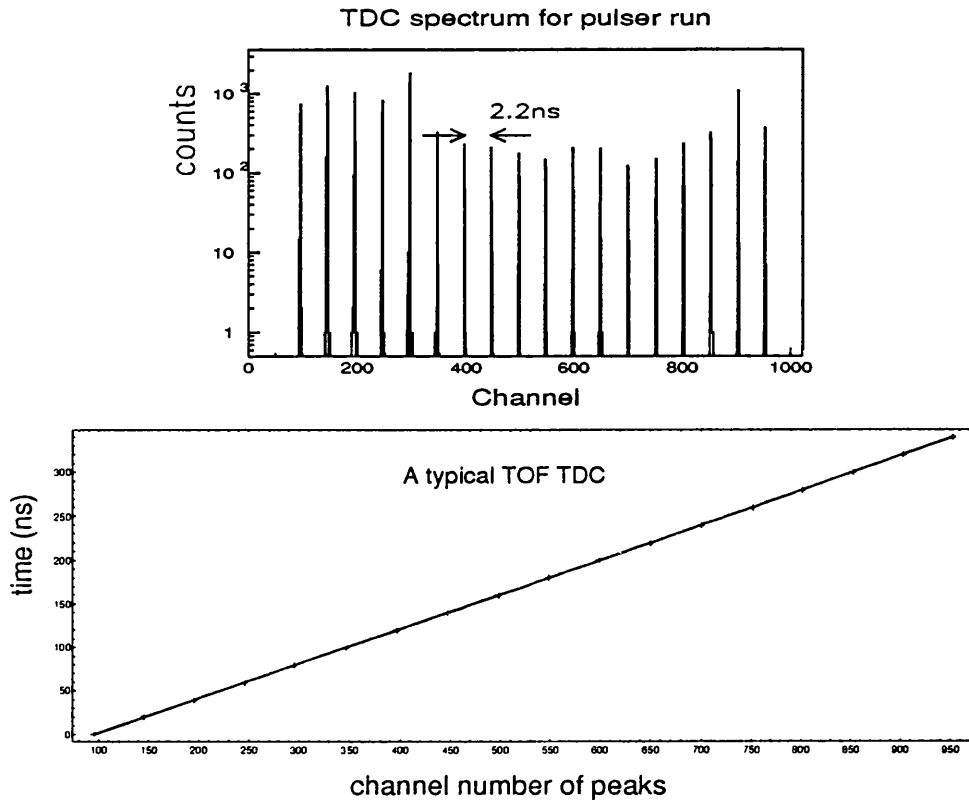


Figure 3.18: *TOF timing calibration: channels to ns*

propagation times and must be subtracted from  $t_{flight}$  to obtain the actual flight time of the particle from the target to the TOF bars. This constant is effectively the time zero,  $t_{zero}$ . To obtain  $t_{zero}$ , relativistic ‘gamma flash’ events were used. These correspond to electrons and photons produced in atomic scattering in the target. The speed of these particles is  $\sim c$  and given the flight path ( $D$ ) from the hit position the actual flight time of the gamma flash from the target to the TOF bar is given by :

$$t_{rel} = \frac{D}{c} \tag{3.25}$$

Plotting a spectrum of the time of flight,  $t_{flight}$  of the gamma flash particles and subtracting  $t_{rel}$  from  $t_{flight}$  for each event will project all the relativistic particles to the zero time of flight channel, i.e. the TDC channel which could be observed if the flight path were zero, figure(3.19). The actual time of flight from the target

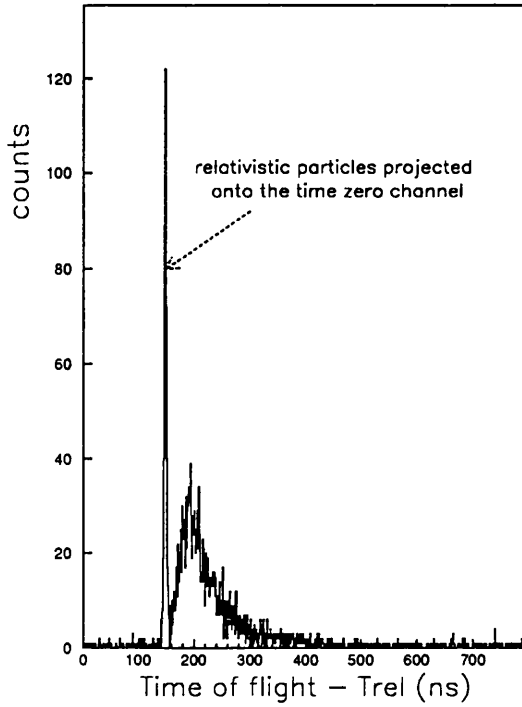


Figure 3.19: *TOF  $t_{zero}$  time-of-flight spectrum*

to the TOF bars is then given by :

$$t_{flight} = t_{mean} - t_{start} - t_{zero} \tag{3.26}$$

for all detected particles.

With the time of flight of the particle, its kinetic energy  $T$  can be calculated using

$$T = m \left( \frac{1}{\sqrt{1 - \beta^2}} - 1 \right) MeV \tag{3.27}$$

where  $m$  is the rest mass of the particle in MeV,  $\beta = v/c$  where  $v = D/t_{flight}$ . For neutrons the values of  $T$  obtained in this way are accurate, but for charged protons a correction must be applied since they lose energy in flight through the air (see data analysis).

## 3.8 Detector Performance

For all three experimental setups all the important calibration parameters are checked using the two body breakup kinematics of the  $D(\gamma, p)n$  reaction. With all the available calibration parameters the two body breakup kinematics are over-determined. Knowledge of the photon energy and one of the nucleon polar angles is sufficient to calculate all the other kinematical variables. Comparing calculated variables with the same directly measured variables allows the calibration to be independently checked and fine tuned. By taking their difference the resolution of the detector can be obtained.

### 3.8.1 Missing Energy

The first step required is to select out the deuterium breakup events from the carbon breakup. This was done by selecting on the reaction ‘missing energy’ which is defined as :

$$E_{miss} = E_{\gamma} - T_p - T_n - T_{recoil} \quad (3.28)$$

where  $E_{\gamma}$  is the photon energy,  $T_p$  and  $T_n$  are the kinetic energies of the proton and neutron, and  $T_{recoil}$  is the kinetic energy of the recoiling system which is zero for deuterium. For the carbon data  $T_{recoil}$  is calculated from the energy and momentum of the detected proton, neutron and photon. The definition can also be written as :

$$E_{miss} = E_x - Q \quad (3.29)$$

where  $E_x$  is the excitation energy of the recoiling system, again for deuterium this is zero. The  $Q$ -value of the reaction for deuterium is :

$$Q = M_D - m_p - m_n = -2.22MeV \quad (3.30)$$

Figure(3.20) shows the missing energy  $E_{miss}$  spectra obtained from a  $CD_2$  target. The calculation assumed a deuterium breakup rather than a carbon breakup,

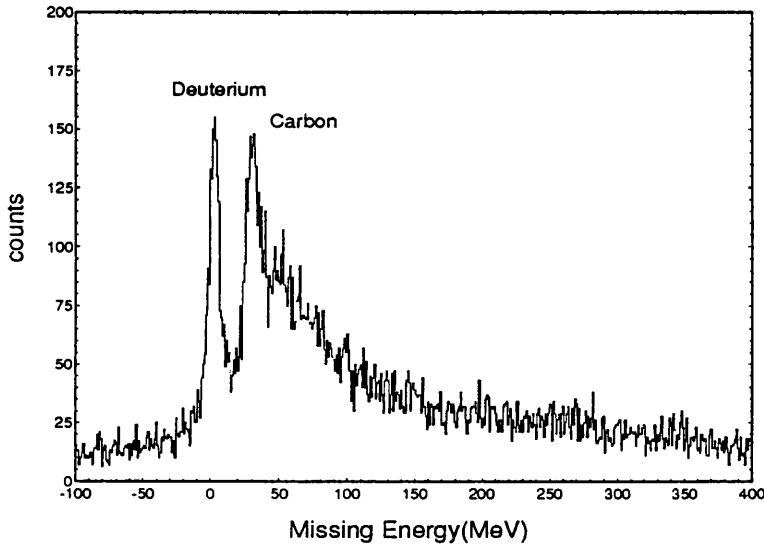


Figure 3.20: *Double arm  $CD_2(\gamma, pn)$  missing energy spectrum*

hence the peak from the deuterium as shown in the plot is at the correct missing energy of 2.2MeV. The carbon peak shown is slightly offset due to the assumption  $T_{recoil} = 0$ .

### 3.8.2 Energy and Angular Resolution

Cutting on the 2.2MeV peak allows deuterium events to be separated from the carbon events. Replotting the proton calibration (cf figure 3.12) now shows a much cleaner deuterium ridge, see figure(3.21). The width of this ridge can be obtained by plotting the difference between calculated (using two-body kinematics) and measured values. Since in the experiment the best determined parameters are the photon energy  $E_\gamma$  and the neutron angle  $\theta_n$ . Using these two variables the proton energy  $T_p$  and proton angular  $\theta_p$  resolutions can be obtained as shown in figure(3.22). The measured values of  $E_\gamma$  and  $\theta_n$  have uncertainties of 2MeV and

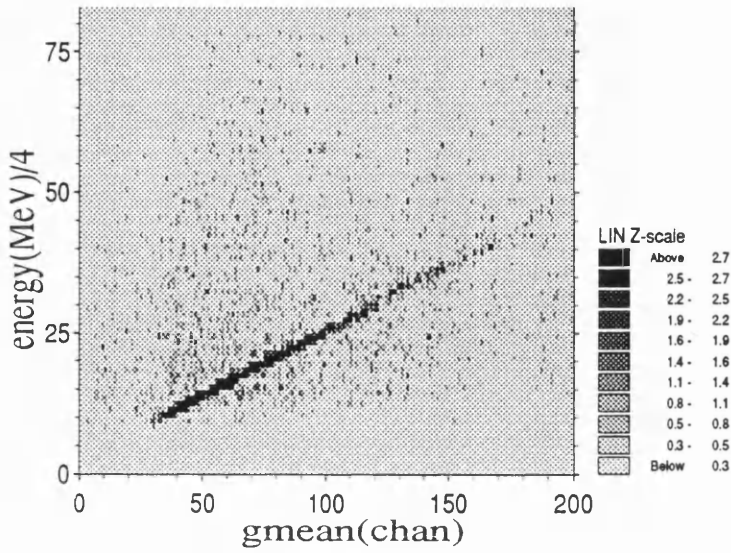


Figure 3.21: *Deuterium ridge cut on missing energy*

$2^\circ$  Full Width Half Maximum(FWHM) respectively, so all calculated variables will have this uncertainty folded in. The uncertainty  $\sigma_{calculated}$  for  $\theta_p$ ,  $T_p$  and  $T_n$  is calculated by error propagation. For example consider  $\theta_p$  where,

$$\theta_p = f(E_\gamma, \theta_n) \tag{3.31}$$

$$\Rightarrow \sigma_{calculated}^2(\theta_p) = \left[ \left( \frac{\partial f}{\partial E_\gamma} \right) \Delta E_\gamma \right]^2 + \left[ \left( \frac{\partial f}{\partial \theta_n} \right) \Delta \theta_n \right]^2 \tag{3.32}$$

where  $\sigma_{calculated}^2(\theta_p)$  is uncertainty in the calculated proton theta angle due to the uncertainty in the photon energy  $\Delta E_\gamma$  and neutron theta angle  $\Delta \theta_n$ . The calculated uncertainty is then subtracted in quadrature from  $\sigma_{difference}$ , which for  $\theta_p$  was found to be  $\sim 4^\circ$  as shown in figure(3.22b). This gives the intrinsic uncertainty of the measured quantity :

$$\sigma_{measured} = \sqrt{\sigma_{difference}^2 - \sigma_{calculated}^2} \tag{3.33}$$

The intrinsic PIP proton polar angular resolution  $\Delta \theta_p$  for all three angular setups was found to be  $\sim 3.5^\circ$ . Alternatively an estimate of the  $\Delta \theta_p$  can also be

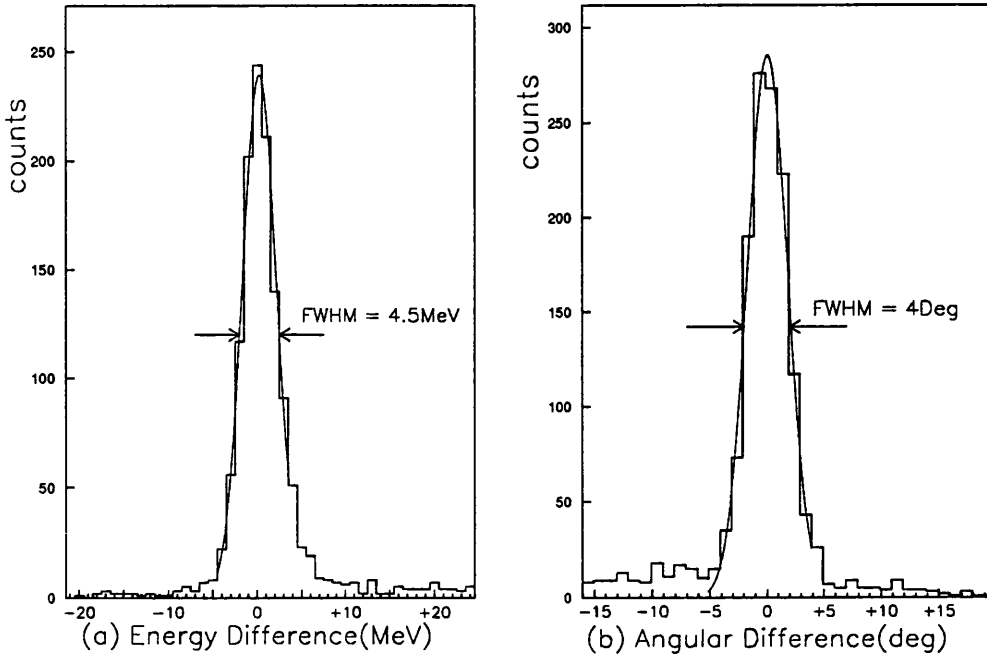


Figure 3.22: (a) PIP proton energy and (b) PIP polar angular resolution: The plots show spectra of the difference between calculated values from two-body kinematics using  $(E_\gamma, \theta_n)$  and the measured values for photon energies of 120 MeV to 400 MeV. The gaussian fit gives  $\sigma_{\text{difference}}(T_p) = 4.5 \text{ MeV}$  and  $\sigma_{\text{difference}}(\theta_p) = 4.0^\circ$ .

determined by the horizontal position resolution of the E1 layer. A position resolution of  $\approx 3 \text{ cm}$  was estimated for E1 layer from the overlap of the time difference spectra, (see previous position calibration figure 3.7). This gives polar angular resolution (at 50 cm from the target) of  $\approx 3.5^\circ$  (FWHM). This is consistent with the above result. The azimuthal angular resolution  $\Delta\phi_p$  was also obtained from an estimate of the vertical position resolution. A value of  $\approx 5.4^\circ$  (FWHM) was obtained.

The intrinsic proton energy resolution for 60 MeV protons was found to be  $\approx 3.0 \text{ MeV}$ . This increases to  $\approx 4.0 \text{ MeV}$  for 100 MeV protons. The overall intrinsic energy resolution folded over the detected proton energy distribution was found to be  $\approx 4.0 \text{ MeV}$  (FWHM), see table (3.2). Such an increase in proton energy has very little effect on the angular resolution.

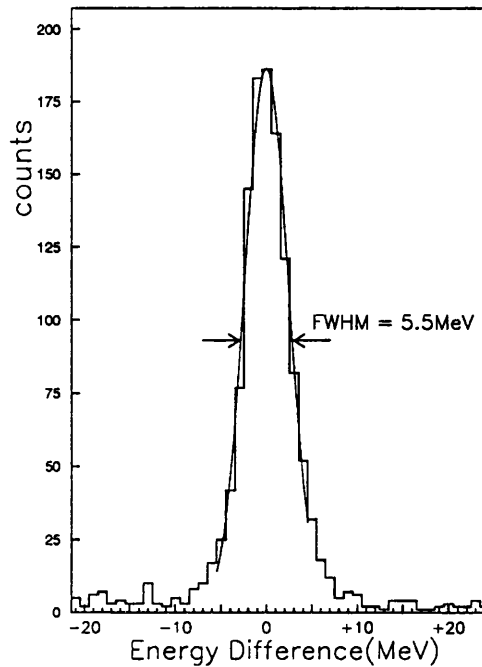


Figure 3.23: Neutron energy resolution. The plot shows spectra of the difference between calculated values from two-body kinematics using  $(E_\gamma, \theta_n)$  and the measured values for photon energies of 120MeV to 400MeV. The gaussian fit gives  $\sigma_{difference}(T_n) = 5.5\text{MeV}$ .

The neutron energy resolution was also determined using  $E_\gamma$  and  $\theta_n$ , see figure(3.23). An intrinsic energy resolution of  $\approx 2.8\text{MeV}$  was obtained for neutron energies of 50MeV at an average flight path of 5.5m. This increases to 5.0MeV at neutron energies of 125MeV. The overall intrinsic resolution folded over the detected neutron energy distribution is  $\approx 5.0\text{MeV}$ (FWHM).

The neutron polar angle resolution is mainly determined by the width of a TOF bar. This being 20cm wide at an average distance of 5.5m from the target gives a resolution of  $\approx 2.0^\circ$ (FWHM). The azimuthal angular resolution was estimated from a plot of the position spectrum of a TOF bar. The width of the rising edge at the ends of the bar gives an estimate of the vertical position resolution. From this an average  $\Delta\phi_n$  of  $\approx 1^\circ$ (FWHM) was obtained.

Finally the missing energy resolution, which has the intrinsic  $E_\gamma$ ,  $T_p$  and  $T_n$  resolutions folded in, was obtained from figure(3.20). A value of 7MeV(FWHM)

was obtained. This is averaged over the range of photon, proton and neutron energy acceptances.

A summary of the detector performance is shown in table(3.2) below. The angular ranges given are measured at beam height, and *fwd*, *cen* and *bck* represents the forward, central and backward angular setups of PIP. The resolutions given are the intrinsic resolutions.

Detector	Particle	Quantity	Acceptance	Resolution(FWHM)
Tagger	$\gamma$	$E_\gamma$	120MeV→400MeV	2MeV
PIP	proton	$E_p$	26MeV→300MeV	4.0MeV
		<i>fwd</i>	22.7° → 101.1°	3.5°
		$\theta_p$ <i>cen</i>	51.3° → 128.6°	
		<i>bck</i>	79.0° → 156.7°	
		$\phi_p$	+22.8° → -22.8°	5.4°
TOF	neutron	$E_n$	≥ 17MeV	5.0MeV
		<i>bck</i>	10.5° → 66.2°	~2.0°
		$\theta_n$ <i>cen</i>	39.6° → 95.4°	
		<i>fwd</i>	99.4° → 153.4°	
		$\phi_n$	162.5° → 192.7°	~1°
Combined		$E_{miss}$	-	7MeV

Table 3.2: Summary of detector performance; the given values of the resolutions are the intrinsic values averaged over the photon energy range 120MeV to 400MeV.

# Chapter 4

## Data Analysis

## Introduction

This chapter sets out the procedures and methods used in extracting the double arm differential cross sections for the  $^{12}\text{C}(\gamma, pn)$  and  $^{12}\text{C}(\gamma, pp)$  reactions. These include methods of particle selection, corrections for detector efficiencies, and random and background subtractions. The analysis was done using the code ACQU which was developed in the Kelvin Laboratory, University of Glasgow by Dr John Annand. ACQU provides the backbone required for data processing. It handles all the necessary input and output of data from main storage devices and it allows the histogramming, storage and display of spectra. The various spectra required and their calculations are the sole responsibility of the users. The results presented in this thesis were analysed largely using the 'C' computing language. This language was chosen for versatility in data handling and ease of debugging. For subtraction of spectra and peak fitting the CERN package PAW was used. Its versatility in scaling and labelling of graphs was exploited for the purpose of data presentation.

### 4.1 PIP Proton Selection

The protons detected in PIP are selected from the background of electrons and pions using the  $\Delta E_2$ -E cut, see previous figure(2.16). Here the E represents the sum pulse height of E1 + E2 + E3 layers. With the pulse height gains of each layer matched, protons with trajectories that straddled two blocks in a layer no longer present a problem and lie inside the  $\Delta E_2$ -E cut. E4 was not used for the purpose of this analysis mainly because within the range of the photon energy analysed, 120MeV to 400MeV, most protons produced would not have enough energy to reach the E4 layer and for those exceptionally few that do reach the E4, the energy and position resolutions would have been severely degraded. The

proton cut also excludes calibration events such as cosmics and TOF flashers which are also collected during the data taking.

## 4.2 TOF Neutron Selection for $(\gamma, pn)$ Events

The TOF side  $\Delta E_{veto}$  detector array covers a solid angle which includes all the TOF bars for all three angular setups, so that all particles reaching TOF must have passed through one of the  $\Delta E_{veto}$  detectors. Charged particles such as  $\pi^\pm$ ,  $p$  and  $d$  will produce a signal in the  $\Delta E_{veto}$  as it passes but due to the relatively thin scintillator thicknesses, neutrons, photons and even relativistic electrons will pass through the  $\Delta E_{veto}$  without leaving a signal above threshold. Any coincidence signal from any of the  $\Delta E_{veto}$  elements with a proton in PIP was identified as a charged particle and rejected for neutron selection (but retained for proton selection see below). Relativistic particles are then rejected by putting a window on the time of flight spectrum see figure(4.1). The lower time-of-flight limit is set by the maximum photon energy to be analysed (400MeV) minus the energy ( $\sim 30$ MeV) required by a proton to reach E1 layer in PIP in order to make an event trigger. This gives a maximum neutron energy of  $\sim 370$ MeV which results in a minimum time of flight slightly less than 26ns at the shortest flight path to TOF. The maximum time of flight limit is set to exclude random events in TOF, see below.

The neutron can interact with the TOF scintillator material and knockout a proton anywhere within a bar and indeed anywhere within a bank of TOF detectors. Sufficiently energetic protons can punch through to subsequent layers leaving signals in each layer. The protons can also be scattered through appreciable angles. This was dealt with by first mapping out the hit pattern for each bank of TOF detectors event by event. Since the induced protons are forward

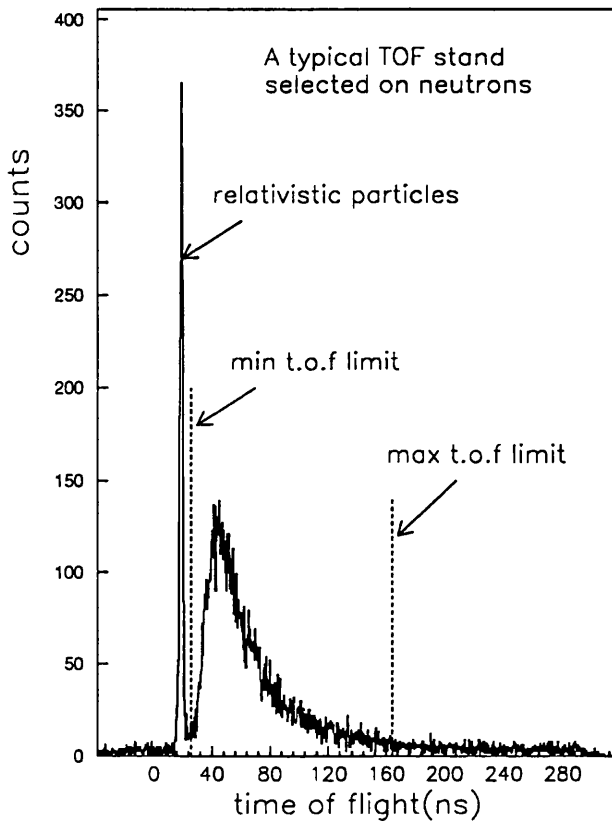


Figure 4.1: *Time of flight window*

peaked, the punch through and scattering hits can be identified if a bar or either one of its adjacent neighbours in the layer immediately in front, viz towards the target, also has a hit. Figure(4.2) shows an exaggerated example of a multi-hits event to illustrate the process. The blacked out bars show where a hit signal is detected. The arrows show what the analysis code will interpret as the bar where the initial neutron interaction took place. Pulse height and timing information from the event will be taken from that bar only. The rest of the hit signals in the same trajectories are made redundant.

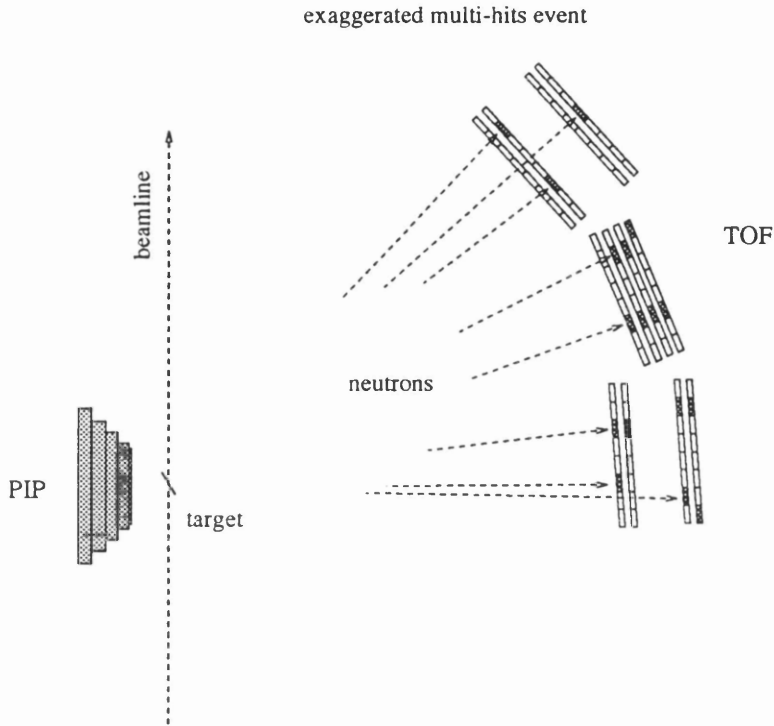


Figure 4.2: *Tracking of neutron induced protons through TOF*

### 4.3 TOF Proton Selection for $(\gamma, pp)$ Events

A charged particle is identified if a signal is present in the  $\Delta E_{veto}$  detector in coincidence with a particle in PIP. The detection efficiency for protons with energies above the TOF detection threshold is taken as 100%. The time of flight limits are the same as for neutron detection. This permits simple comparisons between the  $(\gamma, pn)$  and the  $(\gamma, pp)$  reactions.

Unlike the neutron case, when protons enter a bank of TOF detectors they always leave signals in the front layer of the bank. If the particle is sufficiently energetic it will punch through the front layer and leave signals in the layers behind. Again scattering can occur as it traverses through each layer. Figure(4.3) shows a similar mapping of the hit patterns in each bank of TOF detectors. Only trajectories that have a hit in the front layer are classed as charged particles. The

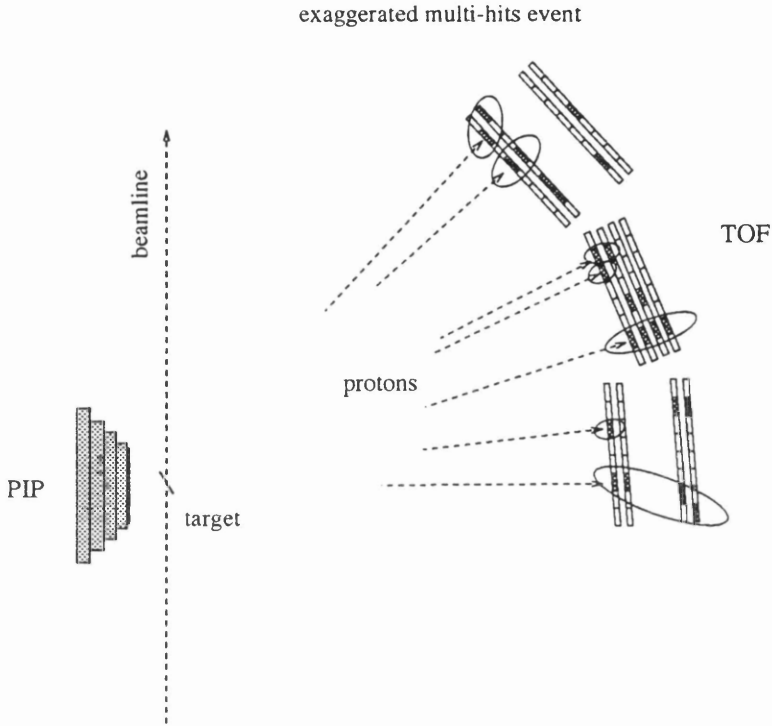


Figure 4.3: *Tracking of protons through TOF*

timing information which is used to calculate the initial energy of the proton is always taken from the hit signals in the front layer. The timing information from the other signals in the same trajectories are made redundant. Here, unlike the case for neutron selection, the pulse height information is also used for particle selection. All the pulse height signals in each proton trajectory are summed together and plotted against the time-of-flight as measured by the front layer. Figure(4.4) shows such a plot, where the pulse height gains of all the TOF PM-tubes have been aligned beforehand. Protons can be selected out cleanly from the deuterons(see previous figure(3.15)) but a relatively small fraction of pions ( $< 5\%$  of all events) lie within the chosen proton cut. The cut includes most of the high energy protons and the small fraction of pions it allows in will be significantly reduced by the missing energy cut applied to the results. Most of the pions have small flight times, and when they are 'misinterpreted' as protons

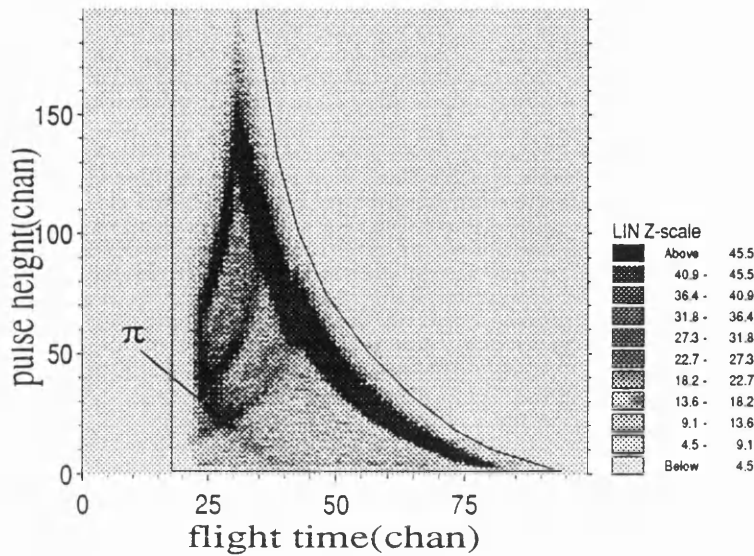


Figure 4.4: *TOF proton selection*

in the  $(\gamma, pp)$  analysis will give incorrectly large  $T_p$  values which in turn results in incorrectly small missing energy values.

The charged protons lose energy in the target, the  $\Delta E_{veto}$  detectors and in the air as they fly towards TOF. This causes the proton to slow down and results in its measured flight time being longer than an equivalent uncharged particle of the same initial kinetic energy. Directly translating this flight time into energy gives a value of  $T_p$  which is ‘averaged’ over the flight path.

A simulation was done to model the slowing down process and an algorithm was devised to correct for the slowing down of the proton, giving the initial  $T_p$  at the target. The simulation starts at the target with a known proton kinetic energy  $T_{p(start)}$  and tracks the proton through the  $\Delta E_{veto}$  detector and then through the air until it reaches TOF. For each small distance  $\Delta x$  it traverses, the proton’s average kinetic energy is calculated taking its energy loss into account, and from this the corresponding flight time  $\Delta t$  for the proton to traverse the small distance

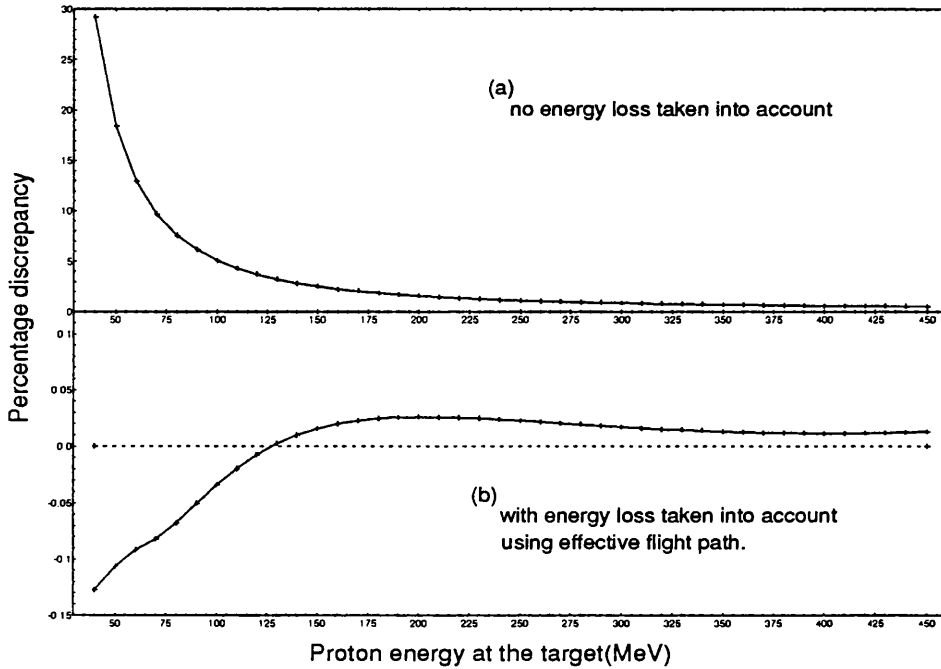


Figure 4.5: *Simulation of proton energy detected in TOF*

$\Delta x$  is calculated and summed from the target to the TOF bar. The integrated flight time  $t_{integ}$  then corresponds to the time-of-flight as measured by TOF. Using  $t_{integ}$  the ‘measured’ kinetic energy of the proton  $T_{p(measured)}$  was calculated. Figure(4.5a) shows a plot of the difference, expressed as a percentage between the proton energy calculated straight from the simulated flight time  $T_{p(measured)}$  and the initial energy at the target  $T_{p(start)}$ .

The algorithm devised essentially modifies the flight path of the measured protons. Given the measured proton energy  $T_{p(measured)}$  the energy it lost during flight from the target to the TOF bar can then be calculated from the modified flight path. The energy lost is then added to the  $T_{p(measured)}$  to give the initial energy at the target. The algorithm is a very good approximation, accurate to within  $\pm 50\text{keV}$  for all proton energies but most of all allows very fast computation. The result is shown in figure(4.5b) where the plot shows the percentage difference

between the initial proton energy  $T_{p(start)}$  and the corrected  $T_{p(measured)}$  calculated using the algorithm.

## 4.4 Random Subtractions

In the raw data the ‘prompt’ region (the region in the timing spectra that corresponds to real coincidence events) will have a contribution due to random events. Random events are caused by spurious particles entering one or other detectors that have no correlation with other particles detected simultaneously. The triple coincidence of the experimental trigger requiring particles to be detected in each of PIP, TOF and the Tagger, significantly reduces the number of random events compared say, to double coincidence experiments. As PIP generates the event trigger which in turn opens the coincidence gate for the Tagger TDCs and the TOF TDCs and QDCs, random events will be evident in these spectra. A method of subtracting the random contribution is to histogram spectra with events taken from the random regions and subtract these spectra from the spectra with events taken from the prompt region [9]. A much neater and overall quicker method of random subtraction adopted here is to assign ‘weights’ to each event. Prompt and random regions in both the Tagger and TOF timing spectrum are defined and assigned positive or negative weights respectively. Events from the separate regions are analysed together and a histogram of the resultant total weights gives a random subtracted spectrum.

### 4.4.1 Tagger Randoms

A spectrum of an OR of all 352 Tagger TDCs forms a sharp peak of width  $\approx 1.2\text{ns}$  FWHM, corresponding to correlated Tagger hits, see figure(4.6). The prompt peak sits on a bed of random events. Within the defined prompt region

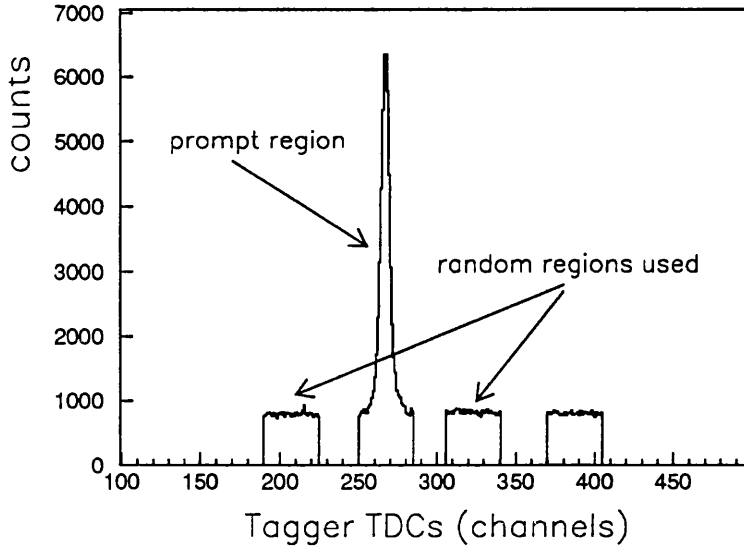


Figure 4.6: *Cuts of Prompt and Random regions in the Tagger timing spectra*

these random events are indistinguishable from the real correlated prompt events and have to be subtracted statistically. All quantities analysed using events in the prompt regions are ascribed a weight

$$w_{prompt}^{\gamma} = + 1.0 \quad (4.1)$$

The two random regions used are shown in figure(4.6). This gives a total random region being twice the width of the prompt region. All quantities analysed from these random regions have a weight;

$$w_{random}^{\gamma} = - \frac{\text{total prompt width}}{\text{total random width}} \quad (4.2)$$

$$\Rightarrow w_{random}^{\gamma} = - 0.5 \quad (4.3)$$

#### 4.4.2 TOF Randoms

Like the Tagger, a plot of the neutron time of flight spectrum also shows a flat random background figure(4.7). The prompt region is defined by considering the minimum neutron time-of-flight which is dictated by the maximum photon

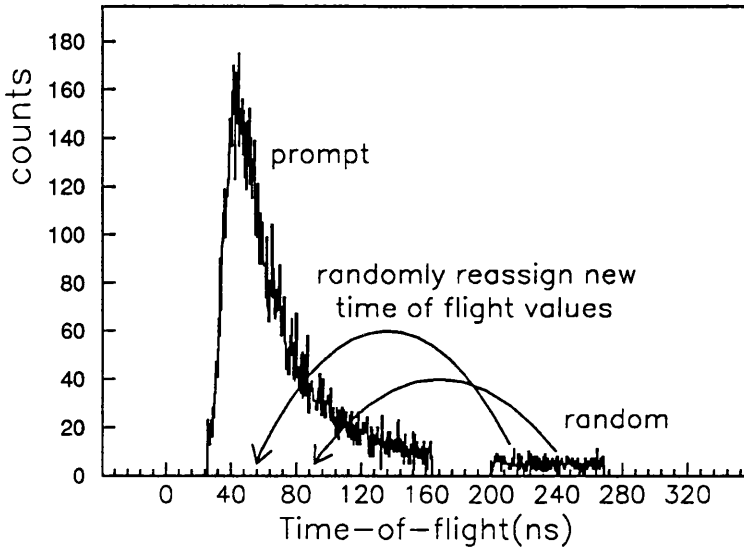


Figure 4.7: *Cuts of Prompt and Random regions in the TOF timing spectra*

energy analysed, and the maximum neutron time-of-flight which is set equivalent to 17MeV (slightly higher than the pulse height threshold of 13.5MeV, where it is dominated by spurious low pulse height background events). The random region to the right of figure(4.7) corresponds to neutron energies below the detector pulse height threshold. The random region chosen is slightly further away from the maximum prompt time-of-flight limit so as to minimize the contribution from small number of very low energy neutrons which are correlated with the trigger but are not analysed. To be useful as a sample randoms in the prompt region, events that fall in this random region must be assigned new time of flight values that lies within the prompt region. These are chosen randomly so as to reduce further any bias from the low energy tail of the prompt region. The events are then analysed in the same way as the events from the prompt region. The weight ascribed to the prompt region is

$$w_{prompt}^n = + 1.0 \quad (4.4)$$

and for the random region

$$w_{random}^n = - \frac{\text{total prompt width}}{\text{total random width}} \quad (4.5)$$

here

$$w_{random}^n = - 2.0 \quad (4.6)$$

## 4.5 Tagging Efficiency

The tagging efficiency  $\epsilon_{tag}$  accounts for the part of the photon flux which is removed by the collimation. The method of measuring the tagging efficiency has been described previously in section(2.2.4). The result(fig 4.8) plotted against the photon energy [63] shows a slight rise with photon energy which is largely due to the fact that the divergence of the photon beam decreases with increasing photon energy allowing more higher energy photons to reach the target. The values of the tagging efficiencies used in the cross section calculation are the individual efficiencies of figure(4.8). This takes into account of the photon energy dependence. There is a small difference ( $\sim 1\%$ ) in the measured tagging efficiencies for the three angular setups. This is on average within the statistical errors, but nevertheless, a separate table of tagging efficiencies was used in each setup.

## 4.6 Neutron Efficiency

Neutrons themselves do not produce ionization in the TOF scintillator. Their detection relies on their probability of interacting with the scintillator material, mainly in proton knockout reactions, which in turn produce scintillation light as charged protons pass through the scintillator. The probability of interaction, and hence the neutron detection efficiency, was modelled with the Monte Carlo code STANTON [59]. The dependence of the efficiency on the incident neutron energy for a single TOF bar is shown in figure(4.9). A pulse height threshold of 7.6MeVee

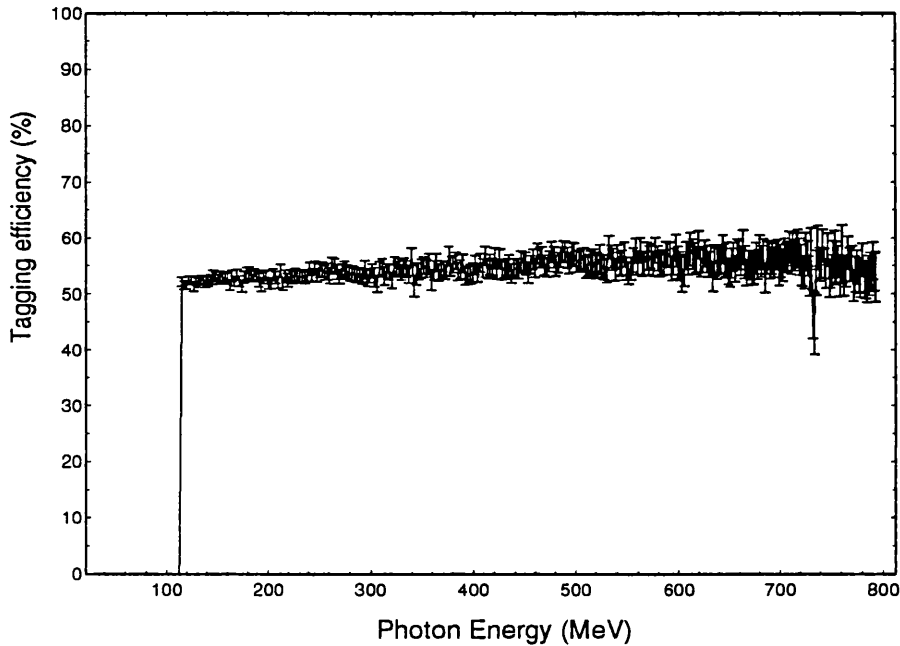


Figure 4.8: *Tagging Efficiency as a function of Photon energy*

was used in STANTON for the detection of the neutrons. The efficiency for  $N$  layers of TOF bars  $\epsilon_n(N)$  can be estimated using the recurrence relation :

$$\epsilon_n(N) = \epsilon_n(N-1) + \epsilon_n^{bar}(1 - \epsilon_n(N-1)) \quad (4.7)$$

with 
$$\epsilon_n(0) = 0.0 \quad (4.8)$$

where  $\epsilon_n^{bar}$  is the efficiency for a single bar, viz a single layer. For the present analysis the neutron detection efficiencies for  $N$  layers of TOF bars ( $\epsilon_n(1, 2, 3$  and  $4)$ ) were modelled separately with STANTON. This provides a more accurate determination of the neutron efficiency.

The neutron solid angle is defined by the front layer of the TOF stand. This ensures an equivalent proton solid angle in TOF, since all charged protons with energy above the pulse height threshold are detected in the front layer. In the case of neutron detection, corrections to the efficiency were applied to the end bars in each stand where the neutron may pass through less than the full set of four

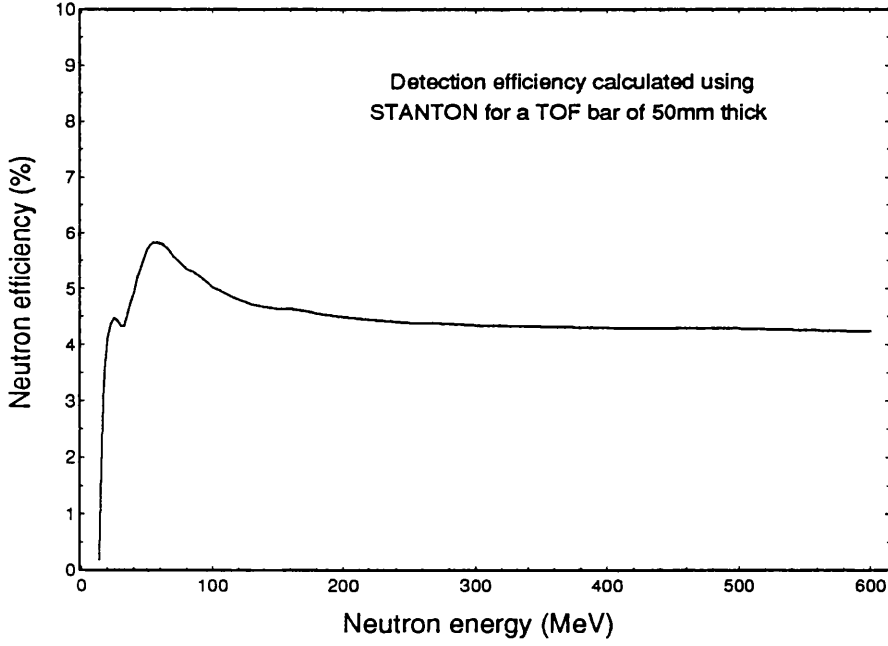


Figure 4.9: *Neutron Efficiency as a function of Neutron energy for pulse height threshold of 7.6MeVee*

layers of scintillator, see figure(4.10). Particles with trajectories lying between 3 and 4 will effectively ‘see’ three layers of scintillator, those with trajectories between 2 and 3 see only two layers of scintillator, and between 1 and 2 see only one layer. The detection efficiency for neutrons with trajectories that go through the 4<sup>th</sup> layer will have a detection efficiency  $\epsilon_n(4)$ :

$$\bar{\epsilon}_n = \epsilon_n(4) \quad (4.9)$$

At the 3<sup>rd</sup> layer the average efficiency for the end bars is :

$$\bar{\epsilon}_n = \frac{a}{l}\epsilon_n(3) + \frac{b}{l}\epsilon_n(4) \quad (4.10)$$

and at the 2<sup>nd</sup> layer :

$$\bar{\epsilon}_n = \frac{c}{l}\epsilon_n(2) + \frac{d}{l}\epsilon_n(3) + \frac{e}{l}\epsilon_n(4) \quad (4.11)$$

and for the front layer end-bar :

$$\bar{\epsilon}_n = \frac{f}{l}\epsilon_n(1) + \frac{g}{l}\epsilon_n(2) + \frac{h}{l}\epsilon_n(3) + \frac{i}{l}\epsilon_n(4) \quad (4.12)$$

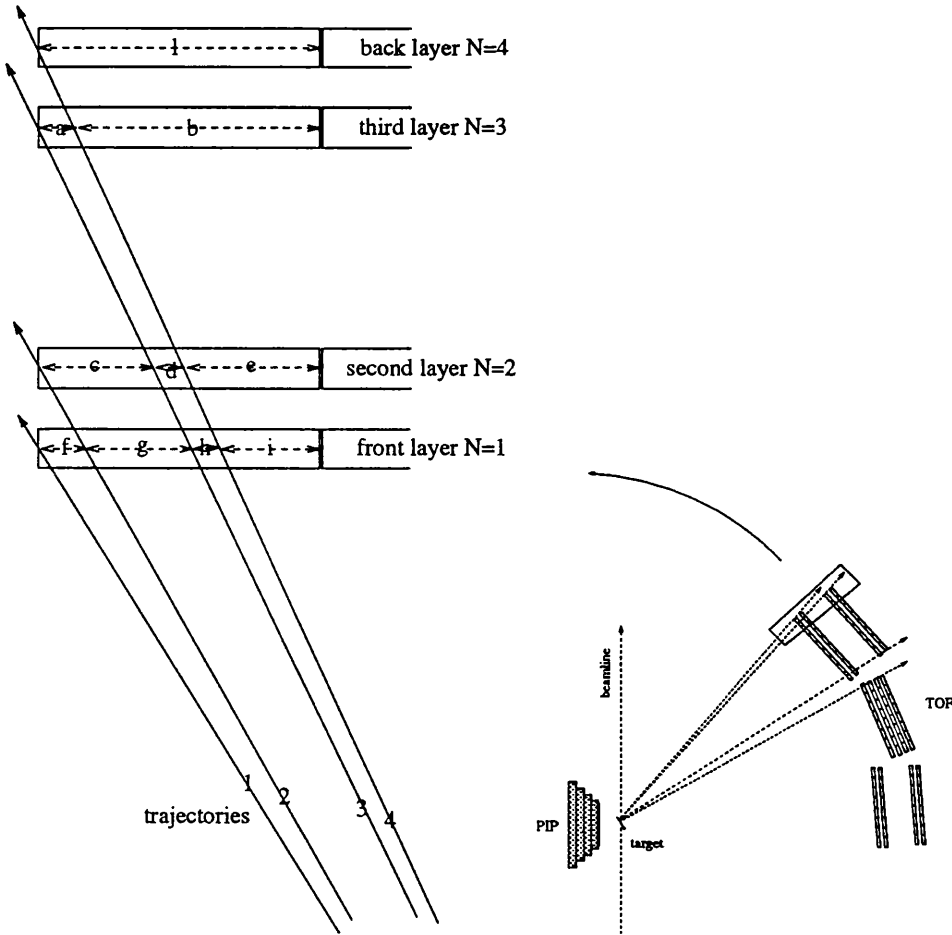


Figure 4.10: *Neutron Efficiency: Edge effects at end bars in each stand*

where  $l$  is the width of a single TOF bar and  $a \rightarrow i$  are the various parts of the bars covered by the trajectories shown in figure(4.10). The above corrections, equations (4.10) to (4.12) only apply to bars at either end of each set of TOF stand. Neutrons detected anywhere in between the end bars effectively see four layers of scintillator. Figure(4.11) shows the neutron efficiency  $\epsilon_n(N)$  vs the incident neutron energy for  $N = 1 \rightarrow 4$ .

There is a small variation of  $< 0.5\%$  in the efficiency along the height of a TOF bar as shown in figure(4.12). This variation in the efficiency is due to the effective increase in the scintillator thickness as the neutron impinges on the scintillator

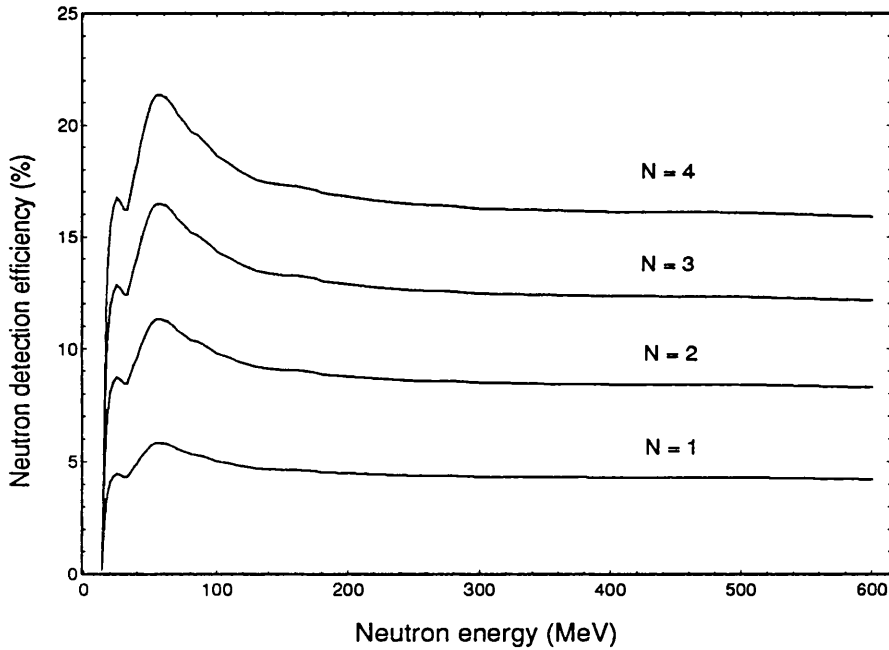


Figure 4.11: Average Neutron Efficiency  $\epsilon_n(N = 1, 2, 3, 4)$

with an increasing angle away from the normal. This is confirmed by the full line, showing the neutron efficiency calculated at the target height and then corrected for the effective increase in the scintillator thickness with height. The result shown in figure(4.12) was obtained with a detection threshold of 7.6MeVee and at a neutron energy of 50MeV.

For the cross section calculation the values plotted in figure(4.11) were used in the form of lookup tables. Edge effects were corrected using equations(4.10,11,12), and the increase in the efficiency as a function of height was corrected using a simple cosine function of the azimuthal angle (with the origin at the target).

## 4.7 Hit Multiplicity : Subevents

Due to the presence of randoms the number of hits in both the Tagger and the TOF detector on average exceeded one for every PIP trigger, when no cut or

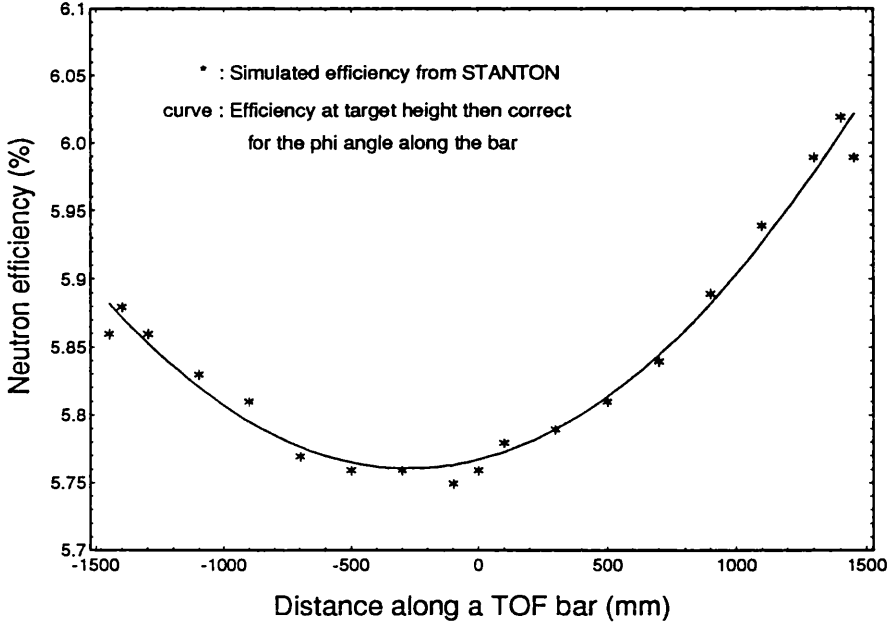


Figure 4.12: Average Neutron Efficiency along a TOF bar

selection on the data was introduced. For each trigger event all the multiple hits detected can be separated and each treated as an individual trigger event, called here a *subevent*. The number of subevents per trigger event is :

$$N_{subevent} = N_{PIP} N_{TOF} N_{TAGGER} \quad (4.13)$$

where  $N_{PIP}$ ,  $N_{TOF}$  and  $N_{TAGGER}$  are the multiplicities in PIP, TOF the Tagger respectively. For each analysed subevent a weight is calculated:

$$\omega^{subevent} = \omega^{PIP} \omega^{TOF} \omega^{TAGGER} \quad (4.14)$$

where  $\omega^{TAGGER}$  and  $\omega^{TOF}$  are the weights due to the particular Tagger and TOF hits and depend on whether the hit lies in the prompt or the random region as discussed above. Particle selection ensures that the PIP multiplicity is always 1 and as PIP makes the trigger its weight  $\omega^{PIP}$  is assigned +1. The histogramming of all the derived quantities for each subevent is incremented by  $\omega^{subevent}$ . The resultant spectra are automatically random subtracted, see for example figure(4.13) which shows a missing energy spectrum.

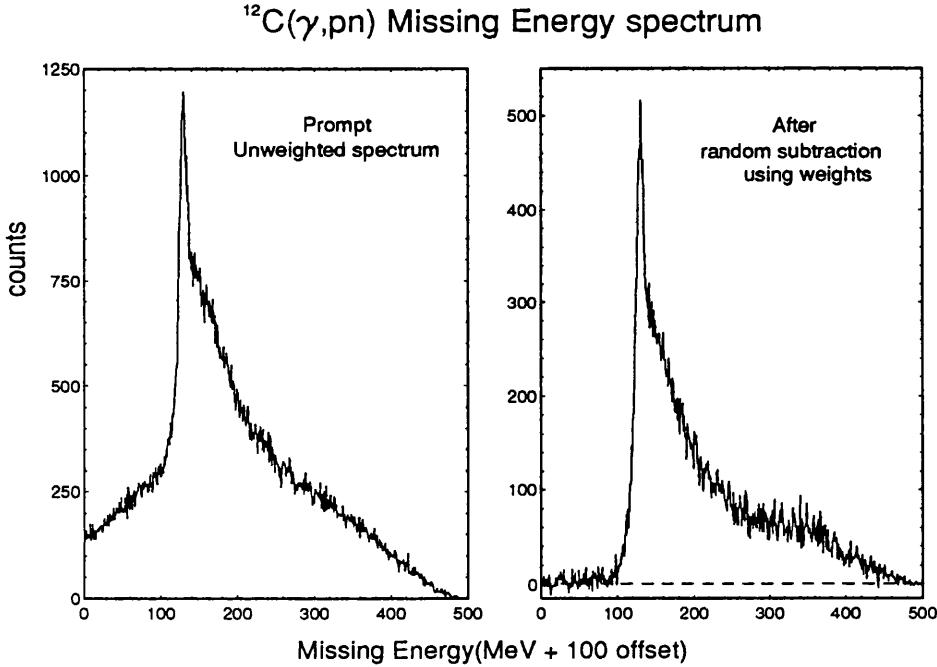


Figure 4.13: *Random subtracted missing energy spectrum*

The detector efficiency described above can also be implemented event by event using weights. The reciprocal of the detector efficiency gives the corresponding detector weight. The weight for each neutron detected is :

$$\omega_{eff}^n = \frac{1}{\bar{\varepsilon}_n(\theta_n, \phi_n, E_n)} \quad (4.15)$$

Some care is needed when treating the detection efficiency as a weight, since as  $\bar{\varepsilon}_n \rightarrow 0$ ,  $\omega_{eff}^n \rightarrow \infty$ ! As shown in figure(4.9) the value of the neutron detection efficiency drops to zero when the neutron energy is less than the pulse height threshold of 13.5MeV. A cut off at a time of flight equivalent to 17MeV neutron energy was set (see section 4.4.2), to avoid very large  $\omega_{eff}^n$  values.

For each Tagger focal plane channel( $i$ ), the number of incident photons reaching the target is given by

$$N_\gamma = N_e(i) \varepsilon_{tag}(i) \quad (4.16)$$

where  $N_e(i)$  is the total number of bremsstrahlung electrons detected in Tagger

focal plane channel( $i$ ). This too can be treated as a photon weight

$$\omega_{eff}^{\gamma} = \frac{1}{N_e(i) \varepsilon_{tag}(i)} \quad (4.17)$$

where  $1/\varepsilon_{tag}$  is the photon tagging efficiency weight and  $1/N_e$ , the bremsstrahlung weight( $\omega_b$ ) is effectively the unfolding of the bremsstrahlung shape of the incident photon. For a photon energy bin of width  $x$  channels the bremsstrahlung weight for channel( $i$ ) becomes :

$$\omega_b = \frac{1}{x N_e(i)} \quad (4.18)$$

this gives the photon weight for focal plane channel( $i$ ) in a photon bin width  $x$

$$\omega_{eff}^{\gamma} = \frac{1}{x N_e(i)} \cdot \frac{1}{\varepsilon_{tag}(i)} \quad (4.19)$$

The total weight of a subevent, viz. the incremental step for all spectra, becomes

$$\omega^{subevent} = \omega^{\gamma} \omega^n \omega_{eff}^{\gamma} \omega_{eff}^n \quad (4.20)$$

where  $\omega^{\gamma}$  and  $\omega^n$  are the *prompt* and *random* weights in the TAGGER and TOF respectively. The total sum of  $\omega^{subevent}$  for all events gives the yield of the reaction with random subtraction, detector efficiencies and bremsstrahlung shape taken into account. For the  $(\gamma, pp)$  reaction, the TOF proton detection efficiency  $\omega_{eff}^p$  is taken as +1. For the present analysis the PIP proton detection efficiency is also taken as +1 for all proton energies. Corrections for the inelastic hadronic reaction of protons in PIP [63] with the scintillator materials is beyond the scope of the present analysis.

## 4.8 Background Subtraction

The air surrounding the target contributes a small fraction to the observed reaction yield. To assess this contribution and in the end to subtract it from the

results dedicated data taking runs where the target was removed from the beam were carried out. In the analysis these ‘target-out’ runs were treated exactly like those with the target in. Random subtraction and detection efficiencies are taken from the same regions and handled in the same way. Suitably normalized background spectra were then subtracted from the ‘target-in’ runs. Here the normalization is automatically taken into account by the bremsstrahlung weights. Figure(4.14) shows the normalized missing energy spectrum from the target-out runs and the resulting background subtracted missing energy spectrum for the  $(\gamma, pn)$  data taken with PIP at the central angle setup and for a photon energy range 110MeV to 500MeV. The contribution of background to the total yield in the missing energy is  $\sim 3.5\%$ .

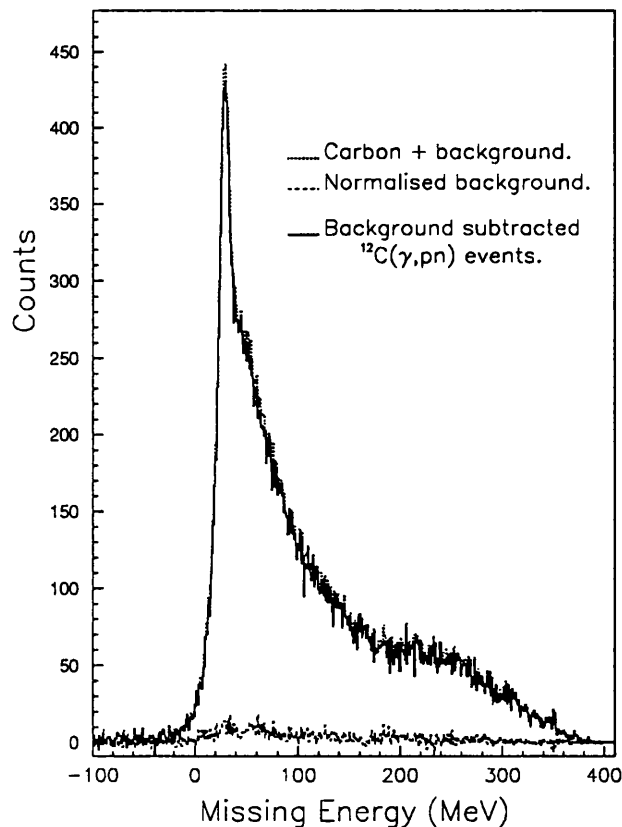


Figure 4.14: *Background subtracted missing energy spectrum*

## 4.9 Cross Section Derivation

The photonuclear reaction probability, i.e. the cross section  $\sigma$  is proportional to the yield of the reaction products,  $Y$ . The yield is in effect the number of reaction events that are measured after random subtractions, and corrections to the detectors' efficiencies have been taken into account. The number of incident photons reaching the target has been accounted for with the bremsstrahlung weight. The yield is then related to the cross section by

$$Y = n_{target} \cdot \sigma \quad (4.21)$$

where  $n_{target}$  is the number of target nuclei per unit area within the beam, and is given by the expression;

$$n_{target} = N_A \cdot \rho_s / A \quad (4.22)$$

Here  $\rho_s$  is the target density in mass per unit area normal to the incident photon beam.  $N_A$  is the Avogadro's number and  $A$  is the atomic mass number of the target, Table(4.1) gives more information on the targets that were used. The

target	$A$	thickness(mm)	$\rho_s(mg/cm^2)$	$n_{target}(cm^{-2})$
CD <sub>2</sub>	16.02	2	432.0	$1.623 \times 10^{22}$
<sup>12</sup> C	12.00	2	664.8	$3.336 \times 10^{22}$

Table 4.1: *Information about the targets used for the experiment : here the  $n_{target}$  values for the CD<sub>2</sub> target gives the number of Carbon nuclei.*

target was graphite or pre-deuterated polythene CD<sub>2</sub> in the case of calibration runs. They were positioned at an angle  $\theta$  to the beam so as to optimize the energy resolution for the outgoing protons. Hence the effective target area density is given as

$$\rho_s = \frac{t_{target} \cdot \rho}{\sin\theta} \quad (4.23)$$

where  $t_{target}$  is the thickness of the target and  $\rho$  is the target density in mass per unit volume. For this experiment not all of the outgoing reaction products were observed, only those protons that lie within a solid angle  $\Delta\Omega_p$  of PIP and have a coincident neutron that lies within a solid angle of  $\Delta\Omega_n$  of TOF, are recorded. This makes our measurement an average double differential cross section where

$$\frac{d^2\sigma}{d\Omega_p d\Omega_n} = \frac{Y}{n_{target} \Delta\Omega_p \Delta\Omega_n} \text{ (cm}^2/\text{sr}^2\text{)} \quad (4.24)$$

and

$$Y = \sum_{events} \sum_{subevents} \omega^{subevent} \quad (4.25)$$

where  $\omega^{subevent}$  is defined in equation(4.20).

This is measured over the proton energy range from  $\sim 26\text{MeV}$  to  $\sim 300\text{MeV}$  and neutron energy range from  $17\text{MeV}$  to  $420\text{MeV}$ . The cross section was obtained for six photon energy ranges with two cuts on the missing energy from  $20\text{MeV}$  to  $40\text{MeV}$  for emission from the  $1p1p$  shells and  $40\text{MeV}$  to  $70\text{MeV}$  for emission from the  $1s1p$  shells. This gives a total of 12 data sets. Table[4.2] tabulates the above constraints in obtaining the cross section. The cuts in the solid angles  $\Delta\Omega_p$  and  $\Delta\Omega_n$  is described below.

For each data set the three separate angular measurements (refer to figure(2.10,2.11,2.12) ), are combined and divided into a total of 18 angular TOF bins. The ranges of each angular bin are determined by splitting each bank of four TOF layers into two. The average neutron angle  $\theta_n$  is taken at the centre of the group of four TOF bars at beam height, see figure(4.15). Table[4.3] gives the average neutron angle of each TOF bin. For each  $\theta_n$  an associated  $\theta_p$  is calculated using two-body kinematics. A PIP angular bin is then defined with  $\pm 10^\circ$  of  $\theta_p$  values, see figure(4.15). A typical scatter plot of  $\theta_p$  against  $\theta_n$  laboratory angle is shown in figure(4.16). The three angular setups are superimposed together and the dashed lines show the boundaries covered by PIP-TOF for each setup.

Missing Energy Bins	
20MeV $\rightarrow$ 40MeV	40MeV $\rightarrow$ 70MeV
Photon Energy Range	Median Photon Energy
120MeV $\rightarrow$ 150MeV	135MeV
150MeV $\rightarrow$ 200MeV	175MeV
200MeV $\rightarrow$ 250MeV	225MeV
250MeV $\rightarrow$ 300MeV	275MeV
300MeV $\rightarrow$ 350MeV	325MeV
350MeV $\rightarrow$ 400MeV	375MeV

Table 4.2: *Missing Energy and Photon Energy Ranges used in the analysis of the experiment.*

A ‘ridge’, which corresponds to the quasi-deuteron breakup kinematics can be observed spanning the three angular setups. The scatter plot has a missing energy range  $E_{miss}$  of 20-40MeV and a photon energy  $E_\gamma$  range 120-150MeV. The PIP-TOF angular bins used for the cross section calculation are illustrated on the right of figure(4.16). The solid angle is defined from these bins (see below). The plot represents the first (of 12) data sets analysed.

## 4.10 Solid Angle Determination

The  $(\gamma, pn)$  reaction is expected to follow the kinematics of quasi-deuteron breakup. Given the neutron polar angle and the median photon energy the corresponding proton polar angle was determined using a two-body deuterium breakup calculation. Here the photon energies used are the median energy listed in table[4.2]. A Q-value of -34MeV was used to simulate a nucleon pair originating from the  $p$ -shell of  $^{12}\text{C}$ .

Average Neutron Polar Angle $\theta_n$ at beam height(deg)		
PIP at backward	PIP at central	PIP at forward
13.9	42.9	102.8
22.9	51.9	111.7
33.3	63.5	122.7
41.9	72.0	131.1
53.7	82.9	141.3
62.8	92.0	150.1

Table 4.3: Table of  $\bar{\theta}_n$  used for evaluating corresponding  $\bar{\theta}_p$

With a given neutron angle, the value of the corresponding proton angle  $\theta_p$  calculated from the two-body quasi-deuteron breakup, changes with photon energy due to the reaction kinematics. Therefore, for each  $\theta_n$  value in table[4.3] there are six  $\theta_p$  values corresponding to the six photon energy bins, see figure(4.16). A list of the  $\theta_p$  values and the corresponding proton solid angle  $\Delta\Omega_p$  and neutron solid angle  $\Delta\Omega_n$  are given in appendix A.

The neutron solid angle  $\Delta\Omega_n$  is determined by the front layer of the group of four TOF bars. For protons the solid angles  $\Delta\Omega_p$  were calculated with a  $\theta_p$  bin width of  $\pm 10$  degrees about the mean  $\theta_p$  angle that corresponds to each TOF bin and taking  $\Delta E_2$  layer of PIP as the other limiting boundary. On the basis of a back-to-back kinematics, the azimuthal range of PIP is  $\sim 1.5$  times larger than TOF. Hence all calculated  $\Delta\Omega_p$  needs to be reduced by 1.5. All solid angles were calculated by integration

$$\Delta\Omega_{p,n} = \int_{\theta,\phi} \sin\theta \, d\theta \, d\phi \quad (4.26)$$

This is illustrated in the schematic diagram of figure(4.15). With the TOF detectors being at an average distance of 5.5m, a group of four bars each 20cm wide

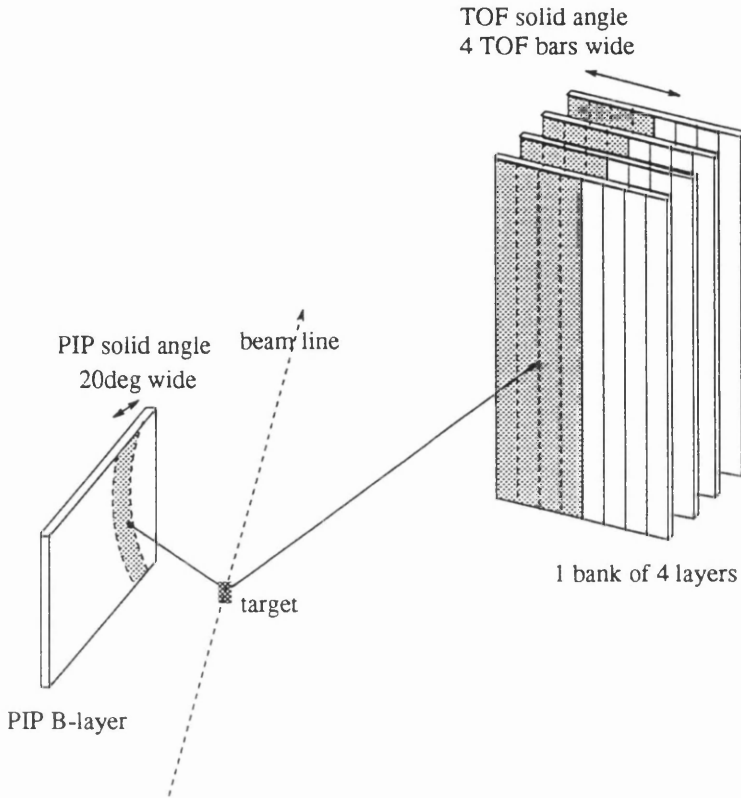


Figure 4.15: *Illustrative diagram for determining  $\Delta\Omega_n$  and the corresponding  $\Delta\Omega_p$*  gives a neutron polar angular spread of  $\sim 8.4^\circ$ . Based on a back-to-back center of mass breakup, this will give a similar  $8.4^\circ$  spread for the proton polar angle  $\theta_p$ . A choice of  $\pm 10^\circ$  about the average  $\theta_p$  is sufficient to span the width of the ridge, the spreading of which is due to the initial nucleon motion.

## 4.11 Dead TOF bars

Throughout the experiment there were a maximum of 6 dead TOF bars out of the 96 in total. These were excluded in the analysis and this in turns leaves ‘holes’ in the TOF banks. The treatment of these dead bars depends on whether the particle involved is a neutron or a proton.

For neutron detection the presence of say 1 dead bar out of a bank of 16 will cause a reduction in the yield of approximately  $1/16$ . This is the case if the dead bar happens to be at the back layer, but if it is in any of the three layers

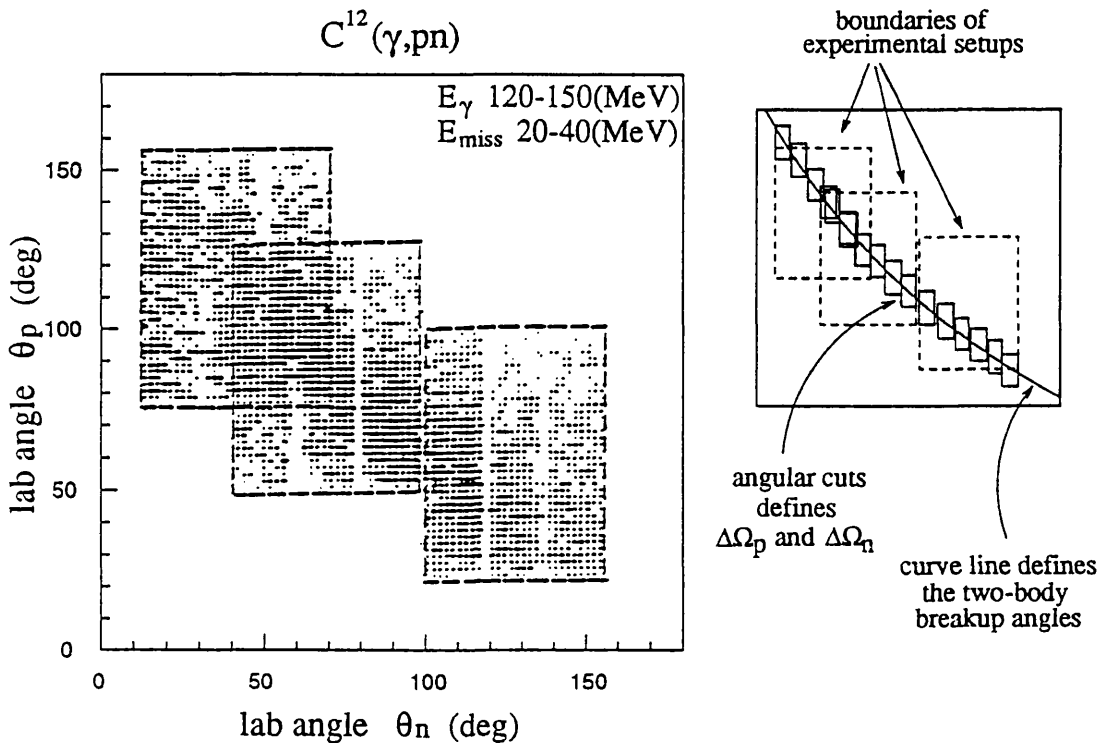


Figure 4.16: *Combined scatter plots illustrating the angular cuts*

in front then the factor  $1/16$  will be slightly too high. This is due to knocked out protons scattering from a dead bar into a live bar in the next layer. If the dead bar was originally live the scattered proton firing the next layer would be thrown out by the tracking procedure, but since the dead bar is excluded in the analysis scattered protons from it are accepted as a hit by the next layer. These scattered events from the dead bar are difficult to distinguish from the real neutron induced proton event in the live bars. A quantitative assessment of the extent of the scattering into the next layer was done by looking at the average number of hits detected in neighbouring bars both with and without the tracking procedure imposed. With the tracking procedure only hits at the start of the tracks are kept. Without tracking, all the hits in all the tracks are kept. So, say for the second layer with tracking the average number of hits is  $c$ , then without

tracking the average number of hits will be  $c + \delta c$ . This is the same as if the corresponding bar of the layer in front was dead. For a bank of 16 bars with 1 dead bar say, then the appropriate correction factor  $f$  to the total yield is:

$$f = \frac{16}{15 + \delta c/c} \quad (4.27)$$

where the average value of  $\delta c/c \sim 0.282$ .

Since for proton selection the proton energies are calculated using the timing information of the front layer, then as long as the bars in the front layer are live then any dead bars in the succeeding layers will not affect the overall yield in the TOF bank. The tracking procedure for proton selection only accepts events if the particle has a hit in the front layer. The calculated time of flight and the gmean pulse height from the front layer alone is sufficient to ensure that the event will stay inside the TOF proton cuts (see previous fig4.4) and be identified as a proton. Now if the dead bar is in the front layer events will be discarded by the proton tracking procedure even if the proton punches through and leaves signals in the next layer. Hence correction to the yield in a TOF bank is required for protons only if any front bars are dead. For one dead front bar in a bank of 4, the correction factor  $f$  is simply  $4/3$ . A table of correction factors are given in appendix B.

## 4.12 Correction for PIP energy Threshold

At mean photon energies of  $\sim 135\text{MeV}$ , the measured proton energy distribution shifts towards lower energies with increasing proton polar angle  $\theta_p$ . Hence the cut-off effect of the detectors' energy thresholds becomes increasingly more important with increasing  $\theta_p$ .

The extent of the threshold cut off was assessed for each angular bin for the data obtained with the photon energy bin of  $135 \pm 15\text{MeV}$ . A Monte Carlo 2N

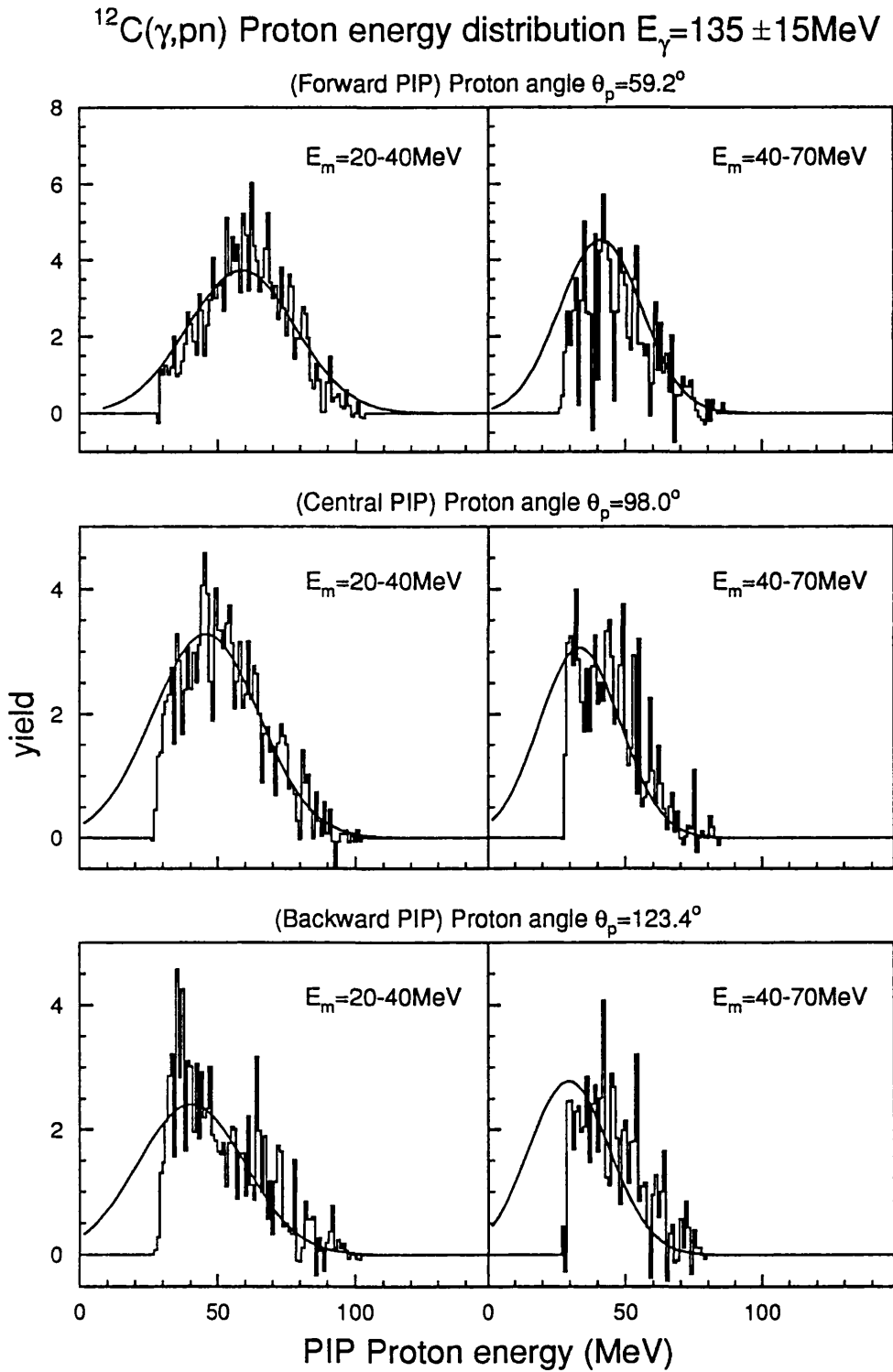


Figure 4.17: Threshold cut off on PIP proton energy distributions: sample distributions of the measured proton energy (histograms) is shown with PIP at forward, central and backward angles selecting on  $59.2^\circ$ ,  $98.0^\circ$  and  $123.4^\circ$  respectively. Correction factors are averaged over the two missing energy regions, 20-40 MeV (left) and 40-70 MeV (right). The corresponding predicted distributions from the  $2N$  model are shown by the gaussian fits (curves).

breakup model [9] was used to predict the proton energy distribution that would be measured if PIP had zero energy threshold. The same PIP-TOF detector geometries, angular cuts and missing energy cuts were applied in the 2N model as in the experimental data. Also the same neutron energy threshold of 17MeV was used with no proton energy threshold. The predicted distribution is smoothed with a gaussian and is scaled to fit the actual measured proton energy distribution, see figure(4.17). The ratio of the total counts under the gaussian to the number of counts under the gaussian above the PIP proton threshold gives the correction factor for undetected events. As expected the cut off is larger at increasing proton angle and missing energy. Correction factors for the two missing energy regions were obtained and applied individually to each angular bin.

The effect of the PIP threshold cut off for all the higher photon energy bins is negligible. Also for comparison with theoretical models, the detectors' threshold effects can be easily incorporated into the model. Hence for the purpose of comparison with existing theoretical calculations in the following chapter, energy threshold corrections were only carried out on the measured data for the 135MeV photon energy bin. The correction factors obtained are tabled in appendix C.

### 4.13 Experimental Uncertainties

The statistical errors of the experiment can be handled relatively simply since they follow a simple probability law. For a spectrum bin containing a total sum of  $S$  counts, its contributions can be written as:

$$S = \omega_1 c + \omega_2 c + \omega_3 c + \dots \omega_N c \quad (4.28)$$

here  $\omega$  is the weight assigned for each entry or event and  $c$  is the condition of the event. In our case there are 4 conditions; prompt-prompt( $c = +1$ ), random-prompt( $c = -1$ ), prompt-random( $c = -1$ ), and random-random( $c = +1$ ) for the

Tagger and the TOF hits. For the case where the spectrum bin has  $N$  events and all the weights are equal to unity then the error of the sum is simply  $\sqrt{N}$ . Now due to the need to subtract statistically random events and to correct for various detector efficiencies the weight  $\omega$  event-by-event is no longer equal to unity. With the increment of the spectrum bin being the normalized weight  $\omega_i$  for the  $i^{th}$  event, the total sum in the bin is now

$$S = \sum_{i=1}^N \omega_i^{subevent} \quad (4.29)$$

where  $\omega^{subevent}$  is given in equation(4.20). The associated statistical uncertainties of the sum  $S$  is then given as:

$$\Delta S = \sqrt{\sum_{i=1}^N (\omega_i^{subevent})^2} \quad (4.30)$$

The systematic uncertainties of the experiment which were propagated through from the uncertainties of the various calibration procedure and alignment measurements have to be assessed individually.

- For the tagging efficiency  $\varepsilon_{tag}$ , an average uncertainty over the whole photon energy region for this experiment was found to be  $\sim 1.5\%$ .
- The sum of the scaler counts in the Tagger has an associated statistical error, but since the sum count is very large, its error can be neglected.
- The target density  $n_{target}$  was precisely weighed and measured. The target angles are set with a computer controlled stepping motor. Both contributions are estimated to be  $< 1\%$ .
- The calculated proton solid angle in PIP has uncertainties stemming from the uncertainties in the position of PIP and the neutron polar angle which reflects the uncertainties in the position of the TOF stand. The position of PIP relative to the target is aligned to better than  $< \pm 2mm$  in the three

cartesian axes. The neutron polar angles which were used to calculate the PIP solid angle as well as the neutron solid angle, are measured to  $< \pm 1\%$ . This makes the element of solid angles for PIP-TOF to be accurate to  $\sim 1\%$ .

- For the neutron detection efficiency  $\epsilon_n$ , the authors of the Monte Carlo code STANTON [59] quote an uncertainty of  $\sim 5\%$  in their result. For proton detection the efficiency is taken as 100% for proton energies above threshold.

For the  $(\gamma, pp)$  measurement the total systematic uncertainty is  $\sim 3\%$ . For the  $(\gamma, pn)$  measurement the systematic uncertainty is dominated by the uncertainty in the neutron detection efficiency, giving a total systematic uncertainty of  $\sim 6\%$ .

There are other sources of uncertainty like the inelastic energy lost of protons in PIP. This effect leads to a lower measured proton energy and increases the number of protons in the low energy region at the expense of the high energy region. These inelastic processes have been studied by Measday and Richard-Serre [65] and their results suggest that  $\sim 3.3\%$  of 50MeV protons will be affected rising to  $\sim 26\%$  for 200MeV protons. However, no correction was made in this analysis, as the effect is not expected to grossly change the shape of the angular distribution, although for the highest photon energy bin it means that the absolute cross section are underestimated by up to  $\sim 26\%$ .

## **Chapter 5**

# **Results and Discussion**

## 5.1 Introduction

The experimental results are presented in this chapter. For both the  $(\gamma, pn)$  and  $(\gamma, pp)$  reactions, the angular distributions are plotted in the form of double differential cross sections as a function of the neutron laboratory angle measured with TOF. This is mainly because of the ease with which the TOF polar and solid angles can be defined. The exceptions to this are figures(5.1 and 5.2) in which the cross sections are plotted as a function of the proton laboratory angle measured with PIP. This is done to allow comparisons to be made with the limited existing theoretical calculations.

At present there are no theoretical calculations available that allow a direct comparison with the present  $^{12}\text{C}$  results. Although detailed calculations for  $^{16}\text{O}(\gamma, pn)$  (as discussed in chapter 1) are available for some particular photon energies, they can at best provide a general indication of the contributing processes. Nevertheless some conclusions can still be drawn regarding the importance of interference effects between the various terms in the pion currents and with heavier mesonic currents.

The present measured data cover an extensive photon energy range  $E_\gamma$  from 120MeV to 400MeV in six photon energy bins. Emission of  $NN$  pairs from the  $(1p1p)$  and  $(1p1s)$ -shells were isolated with missing energy cuts  $E_m$  20-40MeV and 40-70MeV respectively. These are presented separately. A similar set of results for  $(\gamma, pp)$  reaction is also presented with the same  $E_m$  cuts and  $E_\gamma$  ranges as applied to the  $(\gamma, pn)$  reaction, but no theoretical calculation is yet available for comparison. The photon energy range at which the theoretical calculation for  $^{16}\text{O}(\gamma, pn)$  was performed limits comparisons with the present results to the lowest photon energy bin of  $135\pm 15\text{MeV}$ . Though no calculations are yet available, changes in the relative contributions from the different mechanisms particularly at

higher photon energies should provide information on their relative importance.

Results for the  $\sigma(\gamma, pp)/\sigma(\gamma, pn)$  ratio in  $^{12}\text{C}$  as a function of photon energy are also presented. This is plotted for missing energy cuts 20-40MeV, 40-70MeV and 20-70MeV which correspond to  $NN$  pair emission from (1p1p), (1p1s) and (1p1p & 1p1s) shells. Comparisons are made with previous data from Bonn, Toyko and earlier results from MAMI-A and MAMI-B experiments. The  $\sigma(\gamma, pp)/\sigma(\gamma, pn)$  ratio as function of TOF-side laboratory angle for the 20-70MeV missing energy region is also presented.

## 5.2 $(\gamma, pn)$ and $(\gamma, pp)$ Angular Distributions

### 5.2.1 Method of Presentation

A 2-D plot of proton angle versus neutron angle as measured in the laboratory frame for  $(\gamma, pn)$  breakup shows a clear ridge which arises due to the strong angular correlation between the emitted nucleon pairs, see figure(4.16). This back-to-back correlation results in the shape of this ridge being determined by the two-body breakup kinematics. Theoretical calculations by Ryckebusch *et al* predict that the intensity distribution along the ridge, ie the height of the ridge as a function of angle is sensitive to the microscopic reaction mechanisms involved. The method in sampling the intensity distribution along the ridge in the present experiment is described in section(4.9) and illustrated on the right of figure(4.16). The following shows the results of the measured intensity distribution along the top of the ridge plotted as a function of one of the measured nucleon angles.

Each point on the ridge is averaged over a range of photon energies and nucleon angles. For a given photon energy  $E_\gamma$  and say a given neutron angle  $\theta_n$ , the experiment measures a distribution of proton angles, centered about  $\theta_p^{peak}$  which corresponds to the angle given by the two-body kinematics (with the adjusted

Q-values):

$$\theta_p^{peak} = \theta_p(E_\gamma, \theta_n). \quad (5.1)$$

A kinematic shift in  $\theta_p$  was carried out event by event which essentially aligns the proton angular distributions to the distribution centered at  $\bar{\theta}_p^{peak}$  where

$$\bar{\theta}_p^{peak} = \theta_p(\bar{E}_\gamma, \bar{\theta}_n). \quad (5.2)$$

where  $\bar{E}_\gamma$  and  $\bar{\theta}_n$  are the mean photon energy and mean neutron angle of the bin.

The corrected proton angles are therefore given by

$$\theta_p^{corr} = \theta_p^{meas} + (\bar{\theta}_p^{peak} - \theta_p^{peak}) \quad (5.3)$$

where  $\theta_p^{meas}$  is the measured proton angle for that event. The angular shift was only applied to events that lay within the photon energy cuts and neutron angular cuts. This correction has only a small effect on the magnitude of the cross section in each data bin, giving rise to a  $\sim 3\%$  increase. Although the width of the ridge becomes narrower, it has a negligible effect on overall the shape of the angular distribution.

### 5.2.2 Comparison of $(\gamma, pn)$ data with Gent Calculations at low Photon Energy

A comparison between the present  $^{12}\text{C}(\gamma, pn)$  results and published theoretical calculations for  $^{16}\text{O}(\gamma, pn)$  is made in figures(5.1 and 5.2). The data points in both figures are the same. The figure is split into two parts for clarity of comparison with the theoretical predictions. The data are taken from the  $135 \pm 15 \text{ MeV}$  photon energy bin with a missing energy cut of 20-70 MeV which includes contributions from both (1p1p) and (1p1s) pairs. The double differential cross section is plotted as a function of the PIP-side proton polar angle. The data shows good continuity across the three angular setups.

The theoretical calculations shown were discussed in chapter 1 (figures 1.13 and 1.14) and are taken from Vanderhaeghen *et al* [3]. They were performed under specific coplanar kinematic conditions at photon energies of 100MeV in (5.1) and at 140MeV in (5.2). Both calculations use a fully unfactorized approach and the cross section values correspond to the top of the ridge(see section 1.5.3, figure 1.13a), ie the maximum cross sections. Also the calculation is summed over both  $s$  and  $p$ -shell hole states and integrated over the nucleon outgoing momentum.

Figure(5.1) shows the predicted  $\pi$ -meson exchange current contributions calculated at  $E_\gamma=100\text{MeV}$ . The dotted line shows the contributions due to the  $\pi$  - *seagull* term only, the dashed line shows the result due to the  $\pi$  - *pion-in-flight* term alone and the solid line shows the coherent sum from the two terms. The calculated values have been reduced by 54% (see below). It is immediately clear that the 'dip' predicted at around  $80^\circ$  caused by the interference between the seagull term and pion-in-flight term is not present in the data.

The inclusion of the heavier  $\rho$ -meson exchange current is shown in figure(5.2). Here the  $\pi$ -current (dotted line) includes both the seagull and pion-in-flight contributions. The  $\rho$ -current (dashed line), has only the seagull contribution. The full line, showing the resultant interference gives a much better representation of both the shape and magnitude of the measured data. Again the absolute magnitude of the calculations has been reduced by 54% for the following reasons.

Firstly the calculation includes the breakup of the (1s1s) pairs whereas the data shown only has contributions from the (1p1p) and (1s1p) pairs. Also the calculation used  $^{16}\text{O}$  as the target nucleus which has approximately twice as many possible  $pn$  pairs as there are in the  $^{12}\text{C}$  nucleus. A first order estimate may be obtained based on the relative number of  $pn$  pairs. The ratio of all the possible  $pn$  pairs in  $^{16}\text{O}$  to the number of (1p1p) and (1p1s)  $pn$  pairs in  $^{12}\text{C}$  is 2:1. But, as discussed in section(1.4.4) calculations[26] have shown that the relative strength

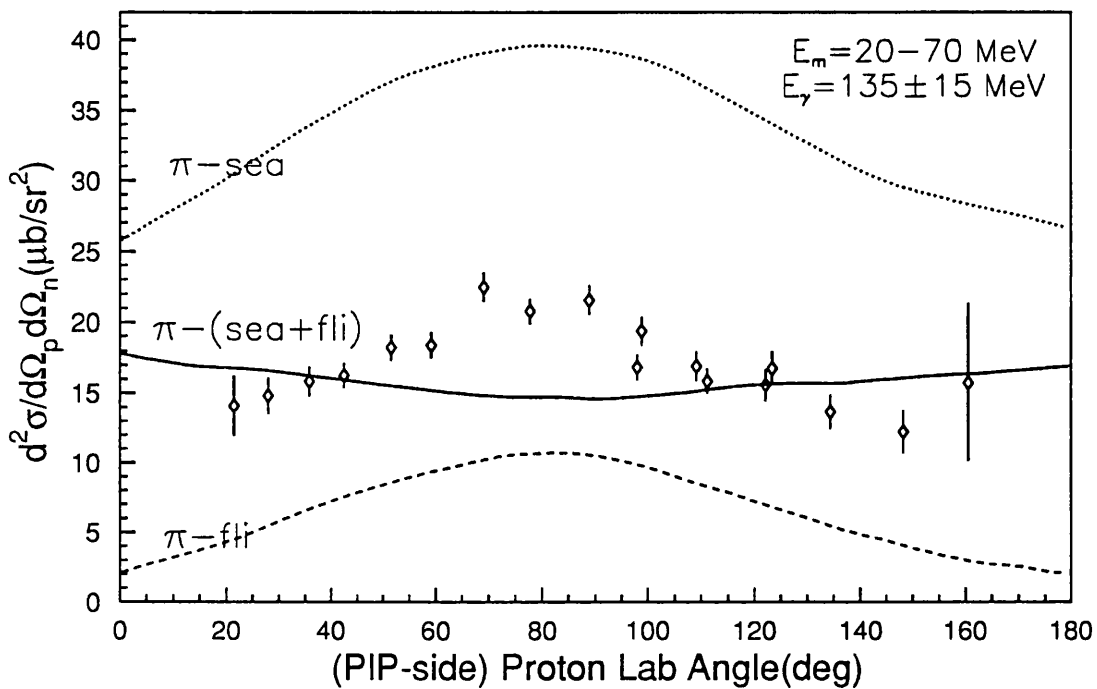
$^{12}\text{C}(\gamma, pn)$  Angular Distribution

Figure 5.1: Comparison of  $^{12}\text{C}(\gamma, pn)$  experimental results for photon energies  $E_\gamma = 120-150 \text{ MeV}$  and missing energies  $E_m = 20-70 \text{ MeV}$  with  $\pi$ -meson contributions calculated by the Gent group [3] for  $^{16}\text{O}(\gamma, pn)$  at  $E_\gamma = 100 \text{ MeV}$  in coplanar kinematics. The magnitude of the calculations has been reduced by 54%, see text. The dotted line shows the contribution from the seagull term, the dashed line shows the pion-in-flight term and the solid line is their coherent sum.

from the different  $2h$  states does not follow directly the number of relative  $pn$  pairs in each subshell. This was supported by experimental evidence, from MacGregor *et al* with  $^{16}\text{O}$ [9] and McGeorge *et al* with  $^{12}\text{C}$ [10]. The average cross section ratio of the  $^{16}\text{O}(\gamma, pn)$  to  $^{12}\text{C}(\gamma, pn)$  reaction for photon energy  $E_\gamma=80\text{-}130\text{MeV}$  is approximately 4:3. Hence a reduction factor of 1.33 was applied to the theoretical  $^{16}\text{O}$  cross sections.

There are additional effects due to the difficulty in determining precisely the solid angle in double arm coincidence measurements. For the analysis of the present experimental data the kinematics of the  $(\gamma, NN)$  reactions are restricted by assuming the nucleon pairs were emitted back-to-back(see section 4.10). For all three angular positions of the present experiment the PIP detector, at an average distance of 500mm from the target with a full height of 420mm, has an azimuthal angular coverage  $\sim 1.5$  times larger than the TOF detectors which is at an average of  $\sim 5500\text{mm}$  from the target with a full height of 3000mm. This in turn means that the effective PIP solid angle is overestimated by a factor of  $\sim 1.5$ .

The theoretical calculation plots the values of the maximum cross section for a given proton angle, whereas the present analysis each data point is averaged over a discrete angular bin. The measured cross section obtained is hence always less than the maximum. The extent of this effect depends on the detector geometries. For angular bins that have the detectors fully inside the back-to-back kinematical region the difference between the maximum value and that of the average values is  $\sim 10\%$ . For angular bins where the detectors are partially inside the kinematic regions the effect is much larger and difficult to assess. This affects mainly the angular bins at each end of the angular range covered by each PIP angle setting. Taking the above considerations into account a total reduction factor of  $\sim 2.2$ , ie 54% was therefore applied to the Gent calculations.

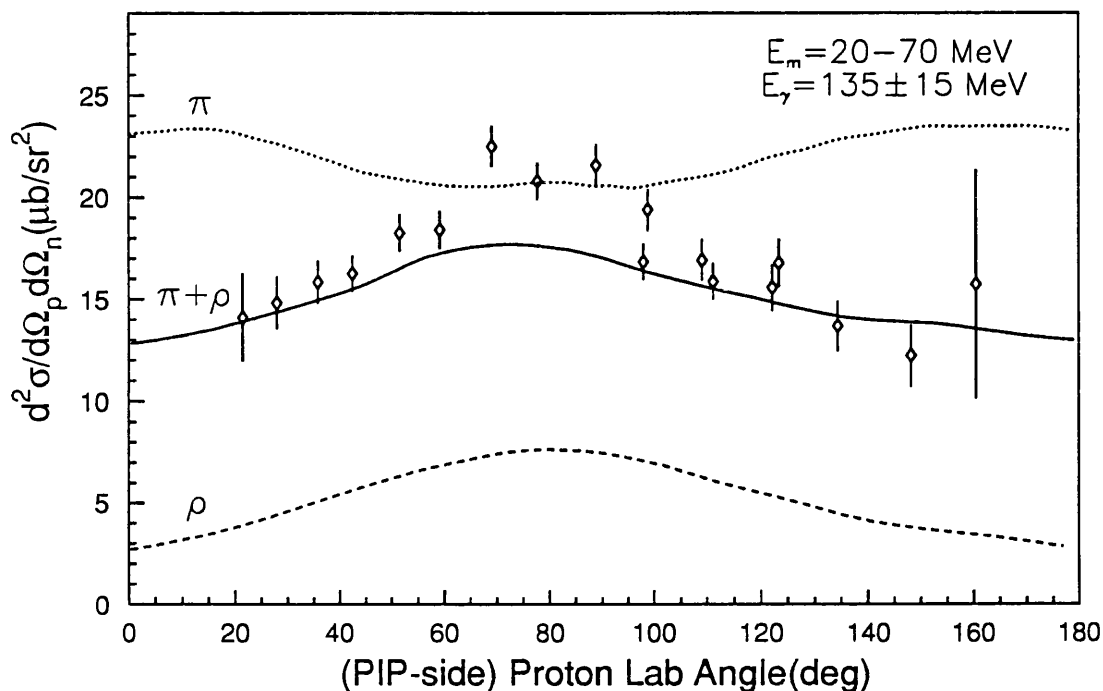
$^{12}\text{C}(\gamma, pn)$  Angular Distribution

Figure 5.2: Comparison of  $^{12}\text{C}(\gamma, pn)$  experimental results with the inclusion of  $\rho$ -meson exchange contribution for photon energies  $E_\gamma=120\text{--}150\text{MeV}$  and missing energies  $E_m=20\text{--}70\text{MeV}$  with theoretical calculations from the Gent group [3] for  $^{16}\text{O}(\gamma, pn)$  at  $E_\gamma=140\text{MeV}$  in coplanar kinematics. The magnitude of the calculations has been reduced by 54%, see text. The dotted line represents the contribution from the  $\pi$ -meson current with both the seagull and pion-in-flight term. The dashed line shows the contribution from the  $\rho$ -meson current (taking account of the seagull term only), and the solid line shows the coherent sum of the  $\pi$  and  $\rho$  contributions.

### 5.2.3 Conclusion: Low Photon Energy Region

The shape and magnitude of the angular distribution data for  $E_\gamma=135\text{MeV}$  matches well with the calculation, though the predicted shape is slightly broader and its peak less sharp.

From the above result it can be concluded that there is a strong indication of the role of the  $\rho$ -meson. This is apparent through the strong interference effects. Thus the  $(\gamma, pn)$  reactions, even at low  $E_\gamma=135\text{MeV}$ , are dependent not only on single pion exchange but also on the much shorter range exchange of heavy mesons.

### 5.2.4 Systematics of $(\gamma, NN)$ Angular Distribution

The following results in figure(5.3,4,5,6) present the angular cross section distribution for  $^{12}\text{C}(\gamma, pn)$  and  $^{12}\text{C}(\gamma, pp)$  as a function of the TOF-side laboratory angles. The angular distribution is presented for all data above thresholds.

For the 20-40MeV missing energy bins, all the  $(\gamma, pn)$  angular distributions exhibit a broad peak at  $\sim 80^\circ$  whereas a sharper peak is observed for the 40-70MeV missing energies bins. The shape of the  $(\gamma, pp)$  is markedly different from that of the  $(\gamma, pn)$  in both missing energy regions, also the  $(\gamma, pp)$  strength is much smaller than that for  $(\gamma, pn)$ . This is not surprising since only neutral meson exchange in the  $\Delta$ -resonance channel is expected to contribute to the direct  $(\gamma, pp)$  channel. In the low 20-40MeV missing energy region, there is a 'dip' in nearly all the photon energy bins. This 'dip' region is most obvious at  $E_\gamma=275\pm 25\text{MeV}$  and is in complete contrast to the  $(\gamma, pn)$  case. A flatter distribution might be expected if the  $(\gamma, pp)$  channel were mainly due to  $(\gamma, pn) + \text{FSI}$ . This gives further support that the  $pp$  emission has different basic mechanism, at least at low missing energies.

At higher missing energies the  $(\gamma, pp)$  spectra are much more similar in shape to the  $(\gamma, pn)$  spectra, showing a broad bump with a maximum around  $\theta_p^{TOF} = 60^\circ - 80^\circ$ , although there is still an indication of a minimum at  $\theta_p^{TOF} = 110^\circ - 130^\circ$  for  $E_\gamma$  above 225 MeV. This may be at least partially due to the effects of FSI which generally increase the observed missing energy so that while the low missing energy region is unaffected the higher missing energy may contain some charge exchange FSI contributions.

The comparison with Gent calculation so far showed very encouraging results. It is hoped that a detailed comparison with theoretical calculations on  $^{12}\text{C}$  taking into account the exact geometries and acceptances of the detectors will allow a more exact comparison with all the present data. The effects due to geometries and acceptances of the detectors, which affect both  $(\gamma, pp)$  and  $(\gamma, pn)$  channels in a similar way, can be easily and more accurately taken into account with the theoretical calculations. With the calculations carried out on  $^{12}\text{C}$  nucleus the corrections due to differences in the target nucleus discussed above would not arise.

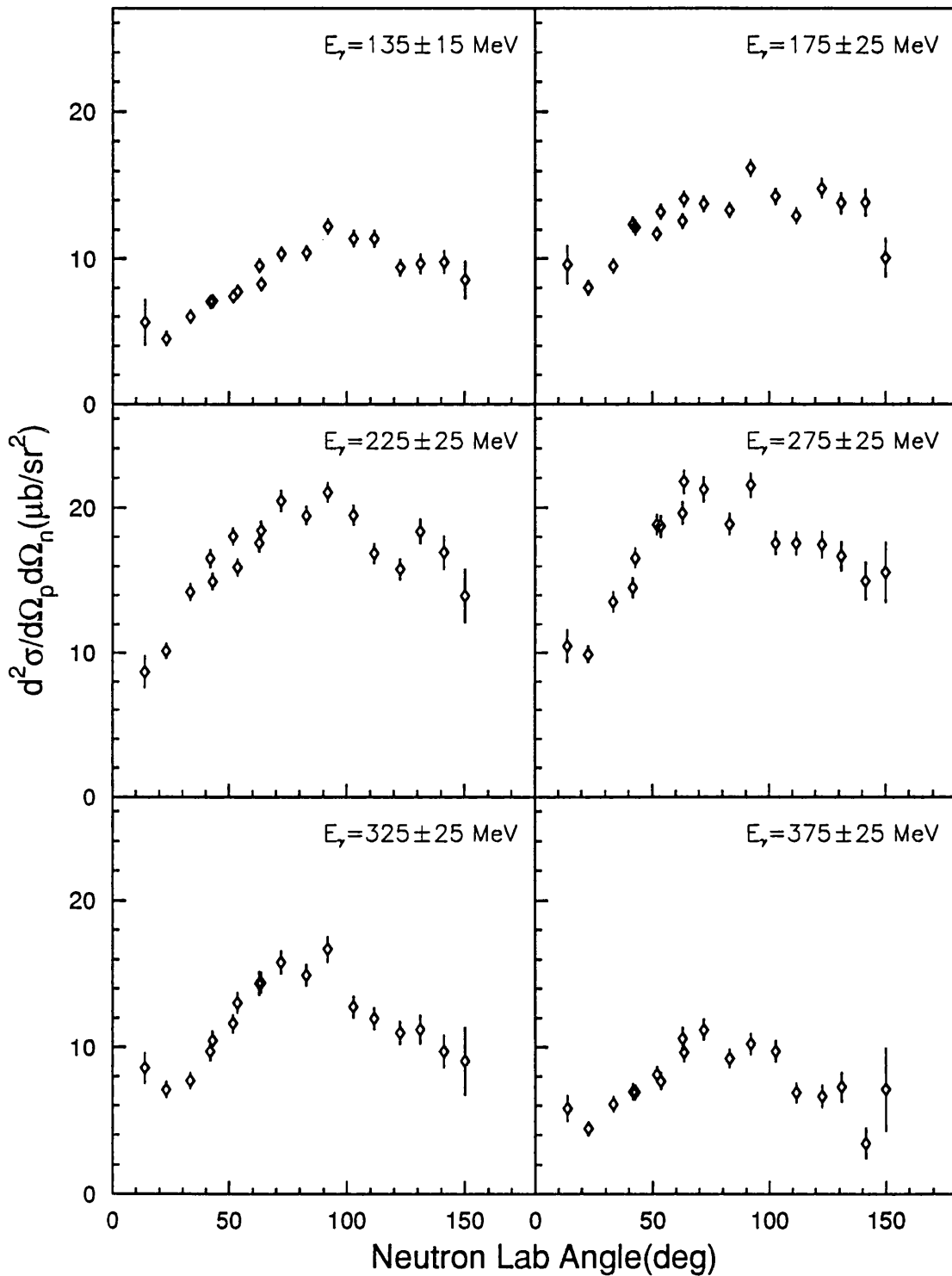
$^{12}\text{C}(\gamma, pn)$  Angular Distribution:  $E_m=20\text{-}40\text{MeV}$ 

Figure 5.3: Angular distribution of  $^{12}\text{C}(\gamma, pn)$  cross section data with missing energy 20-40 MeV, for the photon energy bins 120-150 MeV, 150-200 MeV, 200-250 MeV, 250-300 MeV, 300-350 MeV and 350-400 MeV.

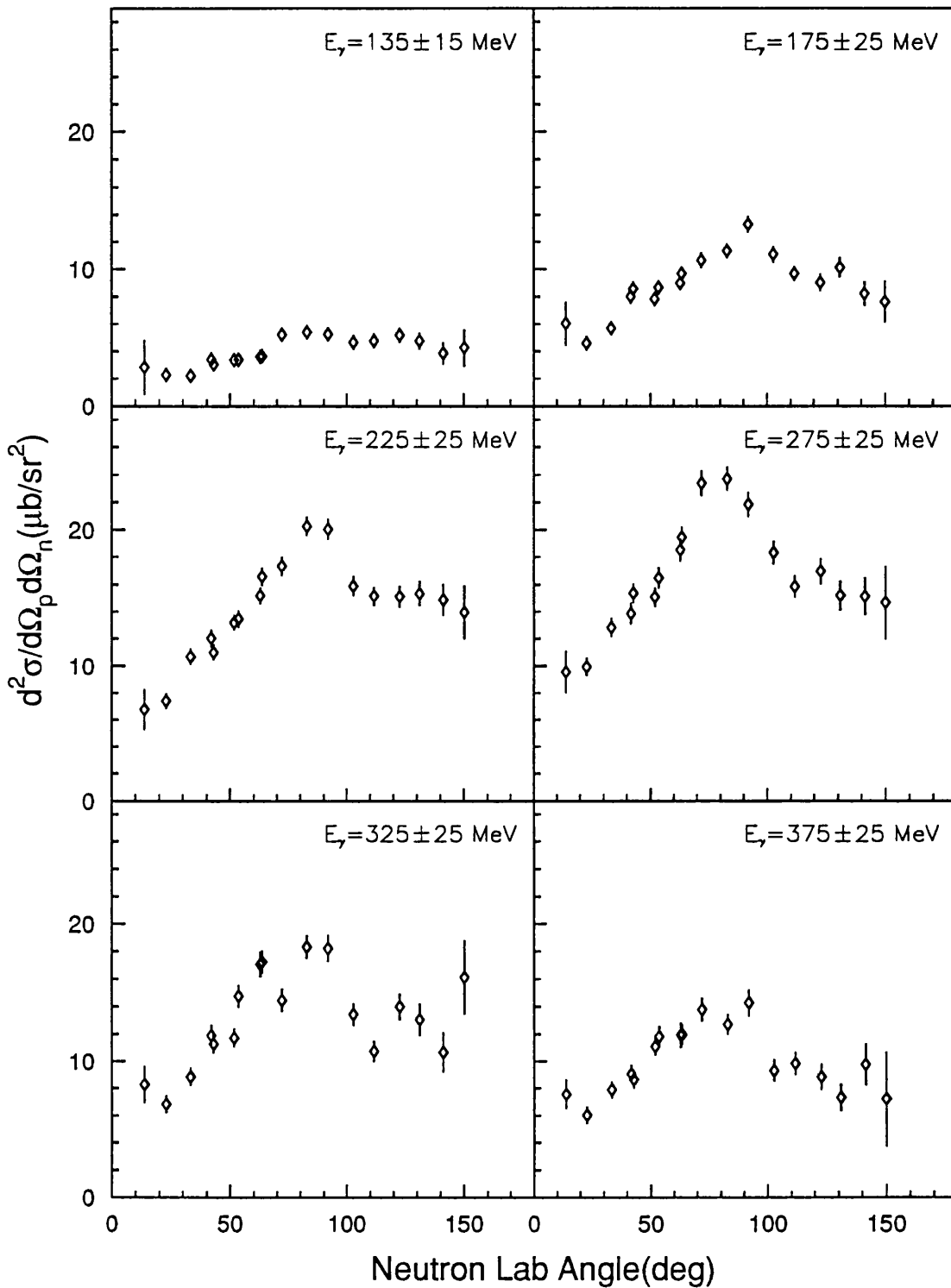
$^{12}\text{C}(\gamma, pn)$  Angular Distribution:  $E_m=40-70\text{MeV}$ 

Figure 5.4: Angular distribution of  $^{12}\text{C}(\gamma, pn)$  cross section data with missing energy 40-70 MeV, for the photon energy bins 120-150 MeV, 150-200 MeV, 200-250 MeV, 250-300 MeV, 300-350 MeV and 350-400 MeV.

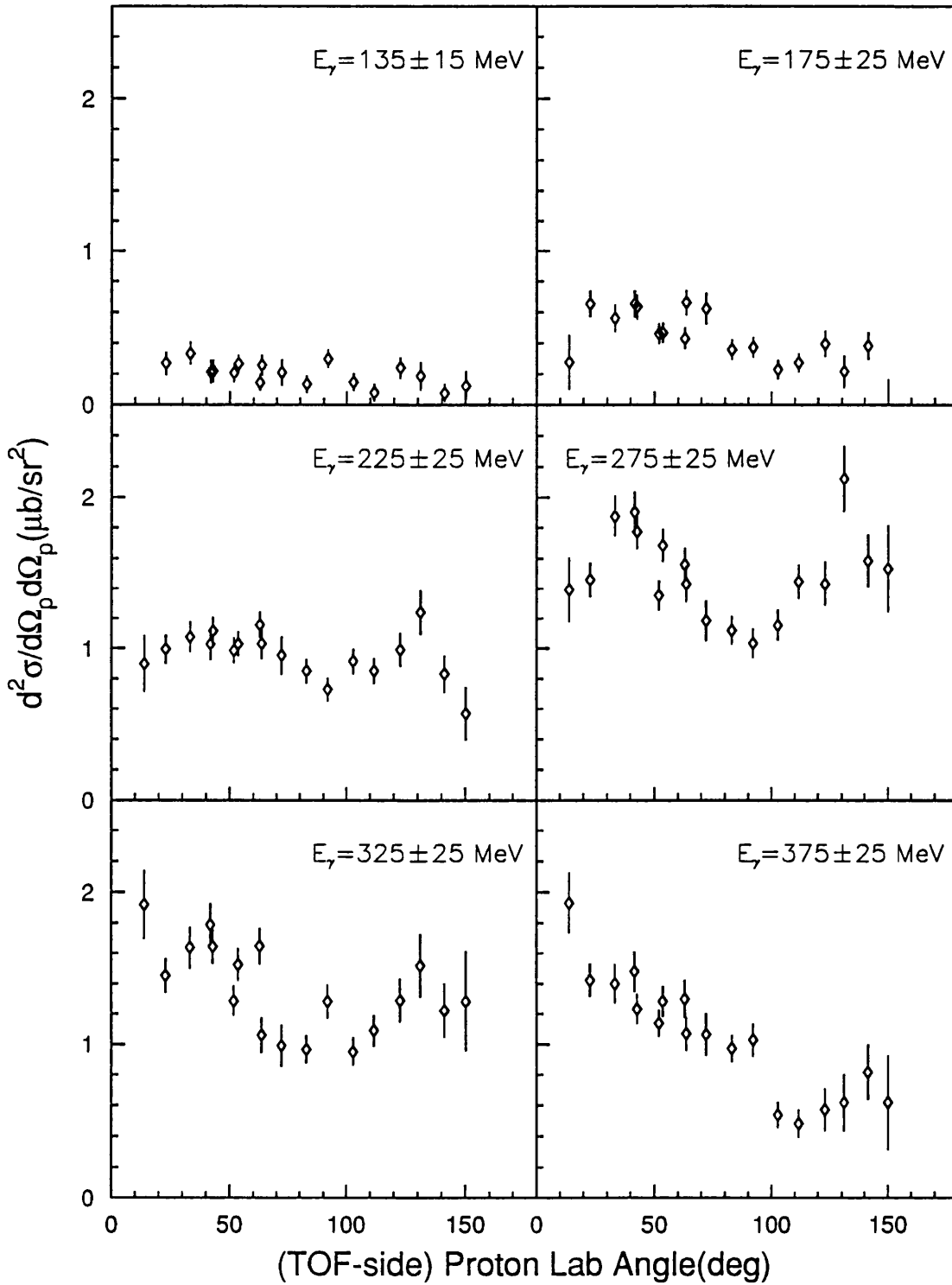
$^{12}\text{C}(\gamma, pp)$  Angular Distribution:  $E_m=20\text{-}40\text{MeV}$ 

Figure 5.5: Angular distribution of  $^{12}\text{C}(\gamma, pp)$  cross section data with missing energy 20-40 MeV, for the photon energy bins 120-150 MeV, 150-200 MeV, 200-250 MeV, 250-300 MeV, 300-350 MeV and 350-400 MeV.

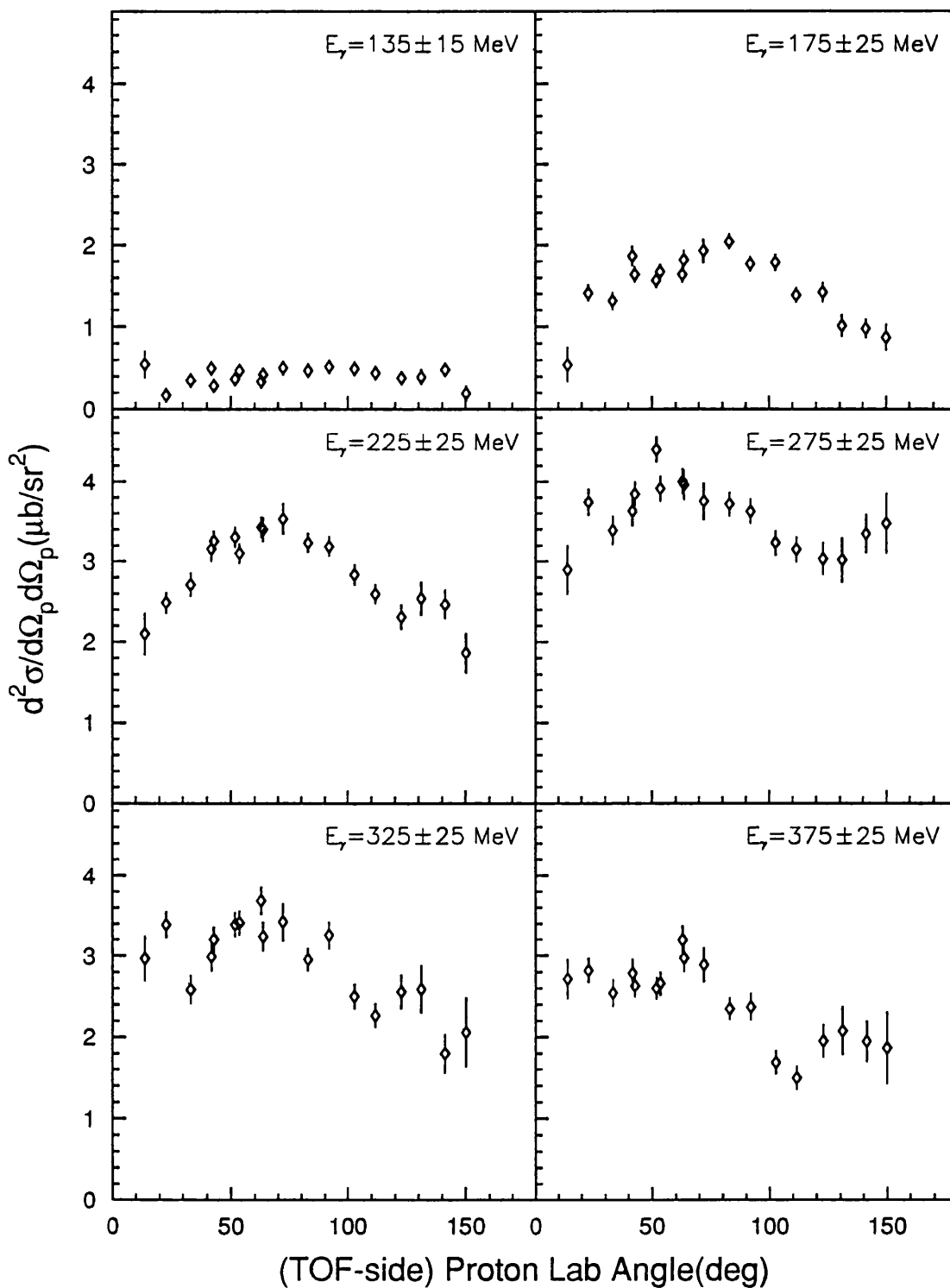
$^{12}\text{C}(\gamma,pp)$  Angular Distribution:  $E_m=40-70\text{MeV}$ 

Figure 5.6: Angular distribution of  $^{12}\text{C}(\gamma,pp)$  cross section data with missing energy  $20-40\text{MeV}$ , for the photon energy bins  $120-150\text{MeV}$ ,  $150-200\text{MeV}$ ,  $200-250\text{MeV}$ ,  $250-300\text{MeV}$ ,  $300-350\text{MeV}$  and  $350-400\text{MeV}$ .

### 5.3 Ratios of $\sigma(\gamma, pp)/\sigma(\gamma, pn)$

The ratio of  $(\gamma, pp)$  to  $(\gamma, pn)$  cross section as a function of photon energy is shown in figure(5.7). The data points are averaged over the same photon energy bins as the cross section results shown in figure(5.3-5.6), and no correction was made for the threshold effects, which are significant only at the lowest photon energy bin. Each data point is also averaged over the whole PIP-TOF angular coverage. Figure(5.7 top) shows the cross section ratios for missing energy cuts 20-40MeV and 40-70MeV. This is compared with calculations from Gent [26] for 2N breakup from the 1p1p(dot-dashed), 1s1p(dashed) and 1s1s(dotted) shells. For the  $(\gamma, pp)$  channel the calculation only has contributions from the  $\Delta$  term with no FSI effects taken into account.

The shape of the two missing energy regions in figure(5.7) showed marked differences. At low missing energies  $E_m=20-40\text{MeV}$ , the cross section ratio increases smoothly with photon energy  $E_\gamma$ , as might be expected due to the suppression of MEC in  $(\gamma, pp)$  channel at low  $E_\gamma$ . As  $E_\gamma$  increases an increasing ratio is expected as the contribution from the  $\Delta$  term increases. Comparison with the calculated 1p1p breakup shows good agreement at low  $E_\gamma$ . The data showed a more rapid rise with increasing  $E_\gamma$  at  $\sim 250\text{MeV}$ . This corresponds to the onset of the  $\Delta$  contribution, suggesting possibly that the  $\Delta$  strength is larger than previously thought.

With missing energy  $E_m=40-70\text{MeV}$ , the measured ratio is approximately a factor of 4-5 times larger than the ratio for the lower missing energy. Also above the  $\pi$  production threshold  $\sim 150\text{MeV}$ , the measured ratio seemed to show a distinct bump on top of a smoothly increasing profile. This may be interpreted as showing the importance of charge exchange FSI at higher  $E_m$  with contributions from  $\text{QF}\pi+\text{FSI}$  processes at higher  $E_\gamma$ .

Figure(5.7 bottom) shows the cross section ratios for missing energy cuts 20-70MeV which include both (1p1p) and (1p1s) pairs. This is plotted along with data from Bonn [20] (triangles), Tokyo [22] (stars), Mainz MAMI-A [10] (solid triangles) and previous Mainz MAMI-B data [66] (circles). Unfortunately the data shown are not directly comparable. The Toyko data are measured at PIP-side proton polar angle  $\theta_p$  of  $30^\circ$  with the 'second' particle detectors covering  $70^\circ$ - $90^\circ$  on the opposite side of the beam. This is outside the back-to-back quasideuteron breakup region. The Bonn data restricts the  $\theta_p$  to  $44^\circ$ - $54^\circ$  but with the 'second' particle detector covering  $41^\circ$ - $131^\circ$ . Both the MAMI-A and MAMI-B data have a smaller  $\theta_p$  range of  $\sim 51^\circ$  to  $\sim 128^\circ$ , but with a much wider range of  $14^\circ$ - $161^\circ$  for the 'second' particle. The previous MAMI-B data were not fully analysed and did not have proper random and background subtractions, though this is not expected to significantly affect the trends of the data.

The present data have detector geometries that maximise the back-to-back emission, and lie above the other results. One reason for this is that at forward and backward angles the measured ratio is significantly larger than at central angles. Figure(5.8) shows the angular distribution of the cross section ratio as a function of TOF-side polar angle (the 'second' particle detector). At central and backward TOF angles, where most of the previous results were concentrated, the ratio is smaller than at forward angles. Taking this into account the differences between the various data sets are reasonable and understandable and the present data are not inconsistent with the previously measured ratios.

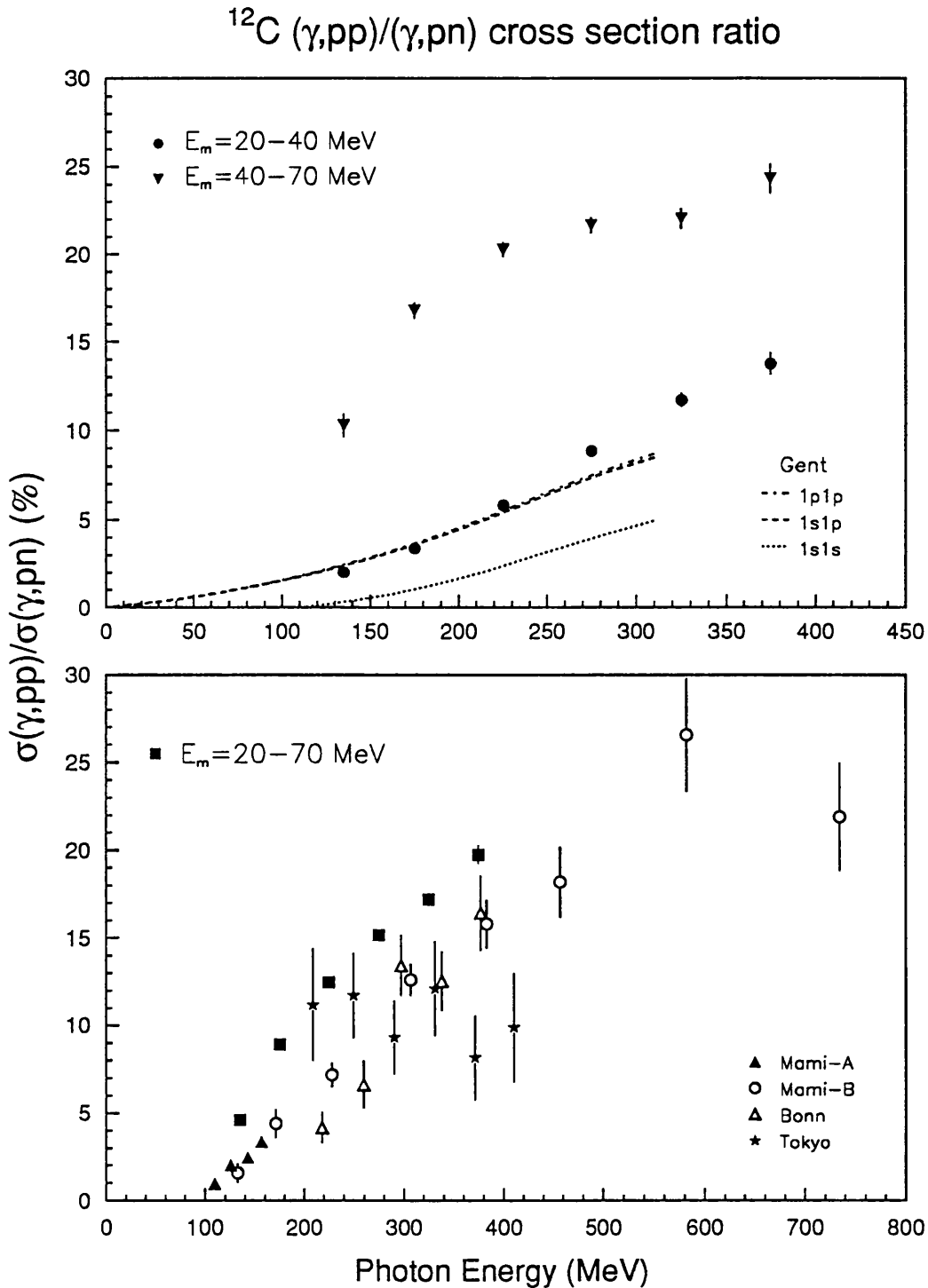


Figure 5.7:  $\sigma(\gamma,pp)/\sigma(\gamma,pn)$  ratio as function of photon energy. The ( $\gamma,pn$ ) and ( $\gamma,pp$ ) cross sections are averaged over the whole PIP-TOF angular coverage. Top diagram shows the present experimental data selecting on missing energies 20-40 MeV (solid circles) and 40-70 MeV (solid inverted triangles). This is compared with calculations from Gent [26] for  $^{12}\text{C}$  ( $pp$ )/( $pn$ ) cross section ratio for the 1p1p breakup (dot-dashed), 1s1p (dashed) and 1s1s breakup (dotted). Bottom diagram shows results with missing energies 20-70 MeV (solid squares) plotted with results from Bonn [20], Tokyo [22] and previous results from MAMI-A [10] and MAMI-B [65], see text.

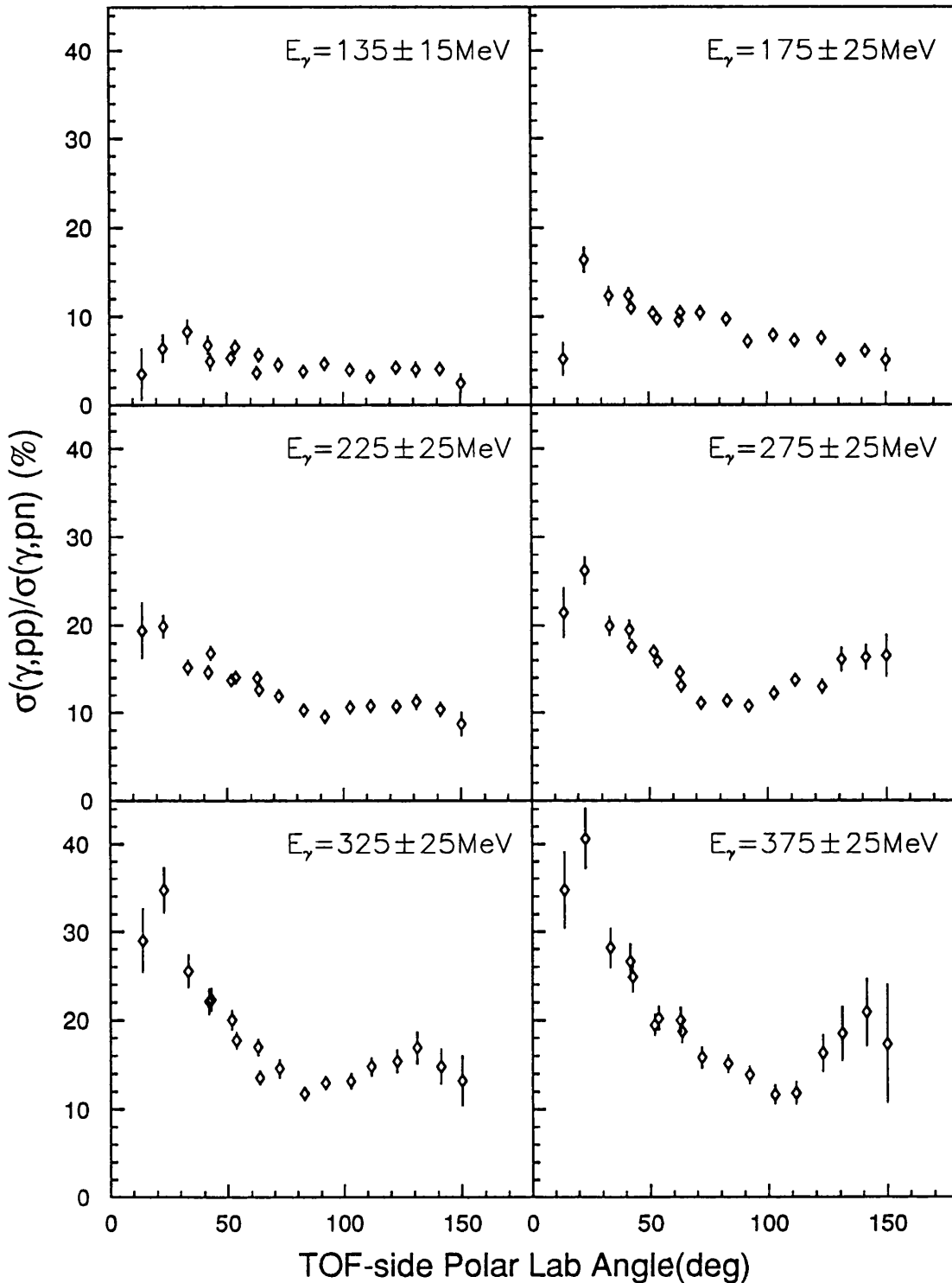
$^{12}\text{C} (\gamma,pp)/(\gamma,pn)$  ratio:  $E_m=20-70\text{MeV}$ 


Figure 5.8: Angular distribution of  $^{12}\text{C} \sigma(\gamma,pp)/\sigma(\gamma,pn)$  ratio with missing energy 20-70MeV, for the photon energy bins 120-150MeV, 150-200MeV, 200-250MeV, 250-300MeV, 300-350MeV and 350-400MeV, see text.

## 5.4 Summary of Experimental Results

Though employing some rather rough first order corrections, the comparison of the theoretical results with the measured data in figure(5.2) shows good agreement both in the shape and the magnitude. The angular distributions of the  $(\gamma, pn)$  and the  $(\gamma, pp)$  reactions show marked differences both in the magnitude and especially in their shapes. While  $(\gamma, pn)$  cases exhibit peaks around central angles, the  $(\gamma, pp)$  cases exhibit 'dips'. The angular distribution of the cross section ratio reflects this behaviour, showing a smaller ratio at the central angles. Comparison of the cross section ratio for missing energy cut corresponding to  $1p1p$  breakup with theoretical calculation, figure(5.7) showed very good agreement at low photon energies with the data, showing a larger ratio in the  $\Delta$ -resonance region. For the higher missing energy corresponding to the  $1s1p$  breakup a much higher ratio was observed in comparison with the theoretical results.

## Chapter 6

## Conclusion

The present angular distribution data is the first of its kind for  $(\gamma, NN)$  photonuclear reactions. Coincidence double arm differential cross sections ( $d^2\sigma/d\Omega_1 d\Omega_2$ ) have been presented as a function of TOF-side laboratory angle for  $^{12}\text{C}(\gamma, pn)$  and  $^{12}\text{C}(\gamma, pp)$  reactions over the (TOF) polar angular range  $13.9^\circ$  to  $150.1^\circ$  for photon energies from 120MeV to 400MeV. For each reaction channel the breakup of nucleon pairs originating from the (1p1p) shells and (1p1s) shells was isolated and the results of their angular distributions presented separately.

The theoretically predicted shape of the  $(\gamma, pn)$  angular distribution agrees well with the general shape of the measured data at low photon energies. The magnitude also agrees well after corrections were applied. Perhaps some variations in the  $\rho$ -meson strength in the theoretical calculation would give a better agreement with the data.

The absence of the 'dip' around  $80^\circ$  is evident in the shape of all the  $(\gamma, pn)$  angular distributions. This strongly suggests an important role for both the  $\pi$ -(*pion-in-flight*) term and more importantly the *seagull* term of the  $\rho$ -meson current because, according to the Gent model, excluding the  $\rho$ -meson contribution will result in a dip at around  $80^\circ$ . This suggests the  $\rho$ -meson exchange has a significant role even at low photon energies. A detailed comparison of the magnitude of the measured angular cross sections with the theory is necessary to give more definitive answers about the relative importance of the interference due to the  $\rho$ -meson and the  $\pi$ -(*pion-in-flight*) term.

For the  $(\gamma, pp)$  case the contributing reaction mechanisms are expected to be very different from the  $(\gamma, pn)$  case. This is shown to be the case by the markedly different shape in their angular distributions. At present there is no model calculation available for comparison with the  $(\gamma, pp)$  results, but it is hoped that once a full comparison with the  $(\gamma, pn)$  results is available work in comparing the  $(\gamma, pp)$  case will follow.

In order to obtain a good comparison in both the shape and the magnitude between the Gent model and the present experiment the best approach is to generate equivalent pseudodata using the Gent model and then to analyse these in exactly the same way as the original experimental data. This involves integrating the PIP-TOF geometries for the three angular setups into the Gent model. The nucleon pairs generated by the model should be tracked from the target through to the scintillator detectors simulating the effect of energy loss and scattering. This ensures that the effect on the results from threshold cuts or detector geometry will apply equally to the pseudodata generated from the theory and to the measured experimental data. Also any possible systematic effects will equally affect both the data and the model predictions.

Full theoretical calculations based on the Gent microscopic model generated as described above will hopefully be available in the near future. A thorough comparison with all the present data will give a more definitive conclusion concerning the importance of various reaction mechanisms, their interference and heavy meson exchange contributions.

# Appendix A

## Table of Results

$^{12}\text{C}(\gamma, pn)$  cross section with  $E_m=20\text{-}40\text{MeV}$

$E_\gamma = 135 \pm 15\text{MeV}$

TOF side ( $n$ )		PIP side ( $p$ )		result
$\theta_{lab}(\text{deg})$	solid angle(sr)	$\theta_{lab}(\text{deg})$	solid angle(sr)	$d^2\sigma/d\Omega_n d\Omega_p(\mu\text{b}/\text{sr}^2)$
102.800	0.0722960	59.224	0.277805	$11.3791 \pm 0.571$
111.700	0.0722018	51.535	0.271025	$11.3747 \pm 0.577$
122.700	0.0638072	42.466	0.255947	$9.3873 \pm 0.569$
131.100	0.0644373	35.818	0.238273	$9.6361 \pm 0.695$
141.300	0.0712122	28.012	0.165438	$9.7537 \pm 0.800$
150.100	0.0705706	21.468	0.087445	$8.5369 \pm 1.295$
42.900	0.0727633	122.159	0.187482	$7.0677 \pm 0.483$
51.900	0.0733384	111.267	0.257381	$7.3989 \pm 0.409$
63.500	0.0653192	98.019	0.273489	$8.2389 \pm 0.447$
72.000	0.0654819	88.867	0.276135	$10.3161 \pm 0.518$
82.900	0.0749560	77.780	0.269932	$10.3891 \pm 0.498$
92.000	0.0747562	69.042	0.257918	$12.2101 \pm 0.552$
13.900	0.0736106	160.505	0.044570	$5.6184 \pm 1.593$
22.900	0.0739018	148.156	0.190088	$4.4825 \pm 0.531$
33.300	0.0657336	134.350	0.258881	$6.0115 \pm 0.449$
41.900	0.0658171	123.402	0.272394	$7.0437 \pm 0.473$
53.700	0.0747291	109.153	0.273674	$7.7190 \pm 0.438$
62.800	0.0758320	98.793	0.263329	$9.5300 \pm 0.474$

Table A.1:  $(\gamma, pn)$  cross sections for  $E_\gamma=135\text{MeV}$  and  $E_m=20\text{-}40\text{MeV}$

$$E_\gamma = 175 \pm 25 \text{MeV}$$

TOF side ( $n$ )		PIP side ( $p$ )		result
theta(deg)	solid angle(sr)	theta(deg)	solid angle(sr)	$d^2\sigma/d\Omega_n d\Omega_p (\mu b/sr^2)$
102.800	0.0722960	56.560	0.276074	$14.2531 \pm 0.577$
111.700	0.0722018	49.102	0.267739	$12.9470 \pm 0.578$
122.700	0.0638072	40.362	0.251329	$14.8004 \pm 0.674$
131.100	0.0644373	33.989	0.230793	$13.7983 \pm 0.732$
141.300	0.0712122	26.539	0.147366	$13.8352 \pm 0.920$
150.100	0.0705706	20.318	0.074395	$10.0535 \pm 1.363$
42.900	0.0727633	119.440	0.222638	$12.1417 \pm 0.532$
51.900	0.0733384	108.307	0.262211	$11.6894 \pm 0.475$
63.500	0.0653192	94.910	0.275176	$14.0798 \pm 0.532$
72.000	0.0654819	85.747	0.275429	$13.7517 \pm 0.555$
82.900	0.0749560	74.745	0.266458	$13.3203 \pm 0.511$
92.000	0.0747562	66.147	0.252600	$16.1732 \pm 0.575$
13.900	0.0736106	159.396	0.055957	$9.5673 \pm 1.309$
22.900	0.0739018	146.417	0.212761	$7.9809 \pm 0.521$
33.300	0.0657336	132.023	0.262676	$9.4882 \pm 0.482$
41.900	0.0658171	120.717	0.274034	$12.3373 \pm 0.521$
53.700	0.0747291	106.158	0.271642	$13.1888 \pm 0.512$
62.800	0.0758320	95.689	0.258449	$12.5855 \pm 0.525$

Table A.2:  $(\gamma, pn)$  cross sections for  $E_\gamma=175\text{MeV}$  and  $E_m=20\text{-}40\text{MeV}$

$$E_\gamma = 225 \pm 25 \text{ MeV}$$

TOF side ( $n$ )		PIP side ( $p$ )		result
theta(deg)	solid angle(sr)	theta(deg)	solid angle(sr)	$d^2\sigma/d\Omega_n d\Omega_p (\mu b/sr^2)$
102.800	0.0722960	53.751	0.273540	$19.4832 \pm 0.706$
111.700	0.0722018	46.551	0.263698	$16.8647 \pm 0.675$
122.700	0.0638072	38.165	0.245936	$15.7845 \pm 0.723$
131.100	0.0644373	32.086	0.216796	$18.3705 \pm 0.861$
141.300	0.0712122	25.012	0.128924	$16.9211 \pm 1.144$
150.100	0.0705706	19.127	0.061117	$13.9647 \pm 1.843$
42.900	0.0727633	116.401	0.247377	$14.9364 \pm 0.582$
51.900	0.0733384	105.038	0.266731	$18.0345 \pm 0.594$
63.500	0.0653192	91.525	0.276092	$18.4264 \pm 0.648$
72.000	0.0654819	82.380	0.273751	$20.4512 \pm 0.707$
82.900	0.0749560	71.502	0.261920	$19.4525 \pm 0.640$
92.000	0.0747562	63.075	0.246250	$21.0235 \pm 0.683$
13.900	0.0736106	158.114	0.070408	$8.6735 \pm 1.144$
22.900	0.0739018	144.424	0.229253	$10.1369 \pm 0.541$
33.300	0.0657336	129.391	0.266367	$14.2265 \pm 0.599$
41.900	0.0658171	117.713	0.275095	$16.5306 \pm 0.632$
53.700	0.0747291	102.859	0.268497	$15.9135 \pm 0.599$
62.800	0.0758320	92.306	0.252225	$17.5954 \pm 0.636$

Table A.3:  $(\gamma, pn)$  cross sections for  $E_\gamma=225\text{MeV}$  and  $E_m=20\text{-}40\text{MeV}$

$$E_\gamma = 275 \pm 25\text{MeV}$$

TOF side ( $n$ )		PIP side ( $p$ )		result
theta(deg)	solid angle(sr)	theta(deg)	solid angle(sr)	$d^2\sigma/d\Omega_n d\Omega_p (\mu b/sr^2)$
102.800	0.0722960	51.348	0.270791	$17.5614 \pm 0.794$
111.700	0.0722018	44.377	0.259771	$17.5382 \pm 0.808$
122.700	0.0638072	36.302	0.240023	$17.4567 \pm 0.910$
131.100	0.0644373	30.476	0.196273	$16.6690 \pm 1.000$
141.300	0.0712122	23.723	0.113624	$14.9698 \pm 1.305$
150.100	0.0705706	18.124	0.048411	$15.5615 \pm 2.061$
42.900	0.0727633	113.652	0.252990	$16.5584 \pm 0.714$
51.900	0.0733384	102.114	0.270039	$18.8098 \pm 0.713$
63.500	0.0653192	88.537	0.276100	$21.7354 \pm 0.800$
72.000	0.0654819	79.434	0.271507	$21.2119 \pm 0.847$
82.900	0.0749560	68.690	0.257306	$18.8527 \pm 0.757$
92.000	0.0747562	60.428	0.230390	$21.5101 \pm 0.840$
13.900	0.0736106	156.910	0.085095	$10.4558 \pm 1.152$
22.900	0.0739018	142.571	0.239560	$9.8763 \pm 0.601$
33.300	0.0657336	126.976	0.269191	$13.5541 \pm 0.708$
41.900	0.0658171	114.990	0.275354	$14.5159 \pm 0.716$
53.700	0.0747291	99.915	0.264894	$18.7079 \pm 0.764$
62.800	0.0758320	89.318	0.246057	$19.6025 \pm 0.795$

Table A.4:  $(\gamma, pn)$  cross sections for  $E_\gamma=275\text{MeV}$  and  $E_m=20\text{-}40\text{MeV}$

$$E_\gamma = 325 \pm 25 \text{ MeV}$$

TOF side ( $n$ )		PIP side ( $p$ )		result
theta(deg)	solid angle(sr)	theta(deg)	solid angle(sr)	$d^2\sigma/d\Omega_n d\Omega_p (\mu b/sr^2)$
102.800	0.0722960	49.239	0.267938	$12.7553 \pm 0.770$
111.700	0.0722018	42.477	0.255970	$11.9467 \pm 0.760$
122.700	0.0638072	34.681	0.233762	$10.9869 \pm 0.819$
131.100	0.0644373	29.078	0.178691	$11.1939 \pm 0.981$
141.300	0.0712122	22.607	0.100567	$9.7141 \pm 1.137$
150.100	0.0705706	17.257	0.037320	$9.0500 \pm 2.323$
42.900	0.0727633	111.121	0.257636	$10.4637 \pm 0.629$
51.900	0.0733384	99.452	0.272440	$11.6139 \pm 0.644$
63.500	0.0653192	85.848	0.275465	$14.4062 \pm 0.728$
72.000	0.0654819	76.801	0.268894	$15.7893 \pm 0.822$
82.900	0.0749560	66.197	0.252696	$14.9214 \pm 0.747$
92.000	0.0747562	58.094	0.200093	$16.6897 \pm 0.890$
13.900	0.0736106	155.764	0.097878	$8.5630 \pm 1.055$
22.900	0.0739018	140.822	0.245588	$7.0863 \pm 0.574$
33.300	0.0657336	124.726	0.271343	$7.6927 \pm 0.582$
41.900	0.0658171	112.481	0.275004	$9.7186 \pm 0.669$
53.700	0.0747291	97.239	0.260986	$13.0374 \pm 0.727$
62.800	0.0758320	86.627	0.213687	$14.3659 \pm 0.809$

Table A.5:  $(\gamma, pn)$  cross sections for  $E_\gamma=325 \text{ MeV}$  and  $E_m=20\text{-}40 \text{ MeV}$

$$E_\gamma = 375 \pm 25 \text{MeV}$$

TOF side ( $n$ )		PIP side ( $p$ )		result
theta(deg)	solid angle(sr)	theta(deg)	solid angle(sr)	$d^2\sigma/d\Omega_n d\Omega_p (\mu b/sr^2)$
102.800	0.0722960	47.358	0.265042	$9.7236 \pm 0.746$
111.700	0.0722018	40.787	0.252297	$6.8773 \pm 0.677$
122.700	0.0638072	33.243	0.227132	$6.6073 \pm 0.780$
131.100	0.0644373	27.842	0.163338	$7.2564 \pm 1.020$
141.300	0.0712122	21.622	0.089204	$3.4451 \pm 1.056$
150.100	0.0705706	16.493	0.028801	$7.1013 \pm 2.847$
42.900	0.0727633	108.765	0.261509	$6.9122 \pm 0.544$
51.900	0.0733384	96.997	0.274132	$8.1218 \pm 0.546$
63.500	0.0653192	83.395	0.274356	$9.6325 \pm 0.642$
72.000	0.0654819	74.415	0.266034	$11.1822 \pm 0.724$
82.900	0.0749560	63.951	0.248134	$9.2181 \pm 0.639$
92.000	0.0747562	56.002	0.173353	$10.2283 \pm 0.759$
13.900	0.0736106	154.660	0.110851	$5.7962 \pm 0.906$
22.900	0.0739018	139.155	0.249433	$4.4265 \pm 0.469$
33.300	0.0657336	122.608	0.272946	$6.0999 \pm 0.548$
41.900	0.0658171	110.143	0.274173	$6.9468 \pm 0.588$
53.700	0.0747291	94.776	0.256862	$7.6715 \pm 0.605$
62.800	0.0758320	84.170	0.181834	$10.5826 \pm 0.793$

Table A.6:  $(\gamma, pn)$  cross sections for  $E_\gamma=375\text{MeV}$  and  $E_m=20\text{-}40\text{MeV}$

$^{12}\text{C}(\gamma, pn)$  cross section with  $E_m=40\text{-}70\text{MeV}$

$E_\gamma = 135 \pm 15\text{MeV}$

TOF side ( $n$ )		PIP side ( $p$ )		result
theta(deg)	solid angle(sr)	theta(deg)	solid angle(sr)	$d^2\sigma/d\Omega_n d\Omega_p (\mu\text{b}/\text{sr}^2)$
102.800	0.0722960	59.224	0.277805	$4.6644 \pm 0.515$
111.700	0.0722018	51.535	0.271025	$4.7608 \pm 0.507$
122.700	0.0638072	42.466	0.255947	$5.1877 \pm 0.510$
131.100	0.0644373	35.818	0.238273	$4.7579 \pm 0.614$
141.300	0.0712122	28.012	0.165438	$3.8682 \pm 0.810$
150.100	0.0705706	21.468	0.087445	$4.2666 \pm 1.355$
42.900	0.0727633	122.159	0.187482	$3.0493 \pm 0.482$
51.900	0.0733384	111.267	0.257381	$3.3694 \pm 0.383$
63.500	0.0653192	98.019	0.273489	$3.6709 \pm 0.410$
72.000	0.0654819	88.867	0.276135	$5.2179 \pm 0.484$
82.900	0.0749560	77.780	0.269932	$5.4022 \pm 0.450$
92.000	0.0747562	69.042	0.257918	$5.2499 \pm 0.518$
13.900	0.0736106	160.505	0.044570	$2.8578 \pm 1.987$
22.900	0.0739018	148.156	0.190088	$2.2894 \pm 0.524$
33.300	0.0657336	134.350	0.258881	$2.2129 \pm 0.450$
41.900	0.0658171	123.402	0.272394	$3.4215 \pm 0.475$
53.700	0.0747291	109.153	0.273674	$3.4239 \pm 0.439$
62.800	0.0758320	98.793	0.263329	$3.6045 \pm 0.429$

Table A.7:  $(\gamma, pn)$  cross sections for  $E_\gamma=135\text{MeV}$  and  $E_m=40\text{-}70\text{MeV}$

$$E_\gamma = 175 \pm 25 \text{ MeV}$$

TOF side ( $n$ )		PIP side ( $p$ )		result
theta(deg)	solid angle(sr)	theta(deg)	solid angle(sr)	$d^2\sigma/d\Omega_n d\Omega_p (\mu b/sr^2)$
102.800	0.0722960	56.560	0.276074	$11.0821 \pm 0.579$
111.700	0.0722018	49.102	0.267739	$9.6736 \pm 0.556$
122.700	0.0638072	40.362	0.251329	$8.9896 \pm 0.626$
131.100	0.0644373	33.989	0.230793	$10.1132 \pm 0.735$
141.300	0.0712122	26.539	0.147366	$8.1951 \pm 0.887$
150.100	0.0705706	20.318	0.074395	$7.5993 \pm 1.505$
42.900	0.0727633	119.440	0.222638	$8.5601 \pm 0.514$
51.900	0.0733384	108.307	0.262211	$7.8239 \pm 0.441$
63.500	0.0653192	94.910	0.275176	$9.6810 \pm 0.483$
72.000	0.0654819	85.747	0.275429	$10.6567 \pm 0.559$
82.900	0.0749560	74.745	0.266458	$11.3417 \pm 0.537$
92.000	0.0747562	66.147	0.252600	$13.3079 \pm 0.589$
13.900	0.0736106	159.396	0.055957	$6.0164 \pm 1.598$
22.900	0.0739018	146.417	0.212761	$4.6056 \pm 0.516$
33.300	0.0657336	132.023	0.262676	$5.6890 \pm 0.468$
41.900	0.0658171	120.717	0.274034	$7.9741 \pm 0.501$
53.700	0.0747291	106.158	0.271642	$8.6502 \pm 0.478$
62.800	0.0758320	95.689	0.258449	$8.9771 \pm 0.492$

Table A.8:  $(\gamma, pn)$  cross sections for  $E_\gamma=175\text{MeV}$  and  $E_m=40\text{-}70\text{MeV}$

$$E_\gamma = 225 \pm 25 \text{MeV}$$

TOF side ( $n$ )		PIP side ( $p$ )		result
theta(deg)	solid angle(sr)	theta(deg)	solid angle(sr)	$d^2\sigma/d\Omega_n d\Omega_p (\mu b/sr^2)$
102.800	0.0722960	53.751	0.273540	$15.8887 \pm 0.711$
111.700	0.0722018	46.551	0.263698	$15.1346 \pm 0.683$
122.700	0.0638072	38.165	0.245936	$15.1012 \pm 0.789$
131.100	0.0644373	32.086	0.216796	$15.3359 \pm 0.896$
141.300	0.0712122	25.012	0.128924	$14.8809 \pm 1.178$
150.100	0.0705706	19.127	0.061117	$13.9704 \pm 1.958$
42.900	0.0727633	116.401	0.247377	$10.9933 \pm 0.574$
51.900	0.0733384	105.038	0.266731	$13.1945 \pm 0.570$
63.500	0.0653192	91.525	0.276092	$16.5693 \pm 0.652$
72.000	0.0654819	82.380	0.273751	$17.3446 \pm 0.685$
82.900	0.0749560	71.502	0.261920	$20.2584 \pm 0.684$
92.000	0.0747562	63.075	0.246250	$20.0393 \pm 0.728$
13.900	0.0736106	158.114	0.070408	$6.7736 \pm 1.504$
22.900	0.0739018	144.424	0.229253	$7.3861 \pm 0.563$
33.300	0.0657336	129.391	0.266367	$10.6810 \pm 0.582$
41.900	0.0658171	117.713	0.275095	$12.0524 \pm 0.628$
53.700	0.0747291	102.859	0.268497	$13.4543 \pm 0.603$
62.800	0.0758320	92.306	0.252225	$15.1666 \pm 0.626$

Table A.9:  $(\gamma, pn)$  cross sections for  $E_\gamma=225\text{MeV}$  and  $E_m=40\text{-}70\text{MeV}$

$$E_\gamma = 275 \pm 25 \text{MeV}$$

TOF side ( $n$ )		PIP side ( $p$ )		result
theta(deg)	solid angle(sr)	theta(deg)	solid angle(sr)	$d^2\sigma/d\Omega_n d\Omega_p (\mu b/sr^2)$
102.800	0.0722960	51.348	0.270791	$18.3303 \pm 0.842$
111.700	0.0722018	44.377	0.259771	$15.8580 \pm 0.806$
122.700	0.0638072	36.302	0.240023	$16.9609 \pm 0.947$
131.100	0.0644373	30.476	0.196273	$15.1763 \pm 1.071$
141.300	0.0712122	23.723	0.113624	$15.1234 \pm 1.356$
150.100	0.0705706	18.124	0.048411	$14.6544 \pm 2.687$
42.900	0.0727633	113.652	0.252990	$15.3483 \pm 0.709$
51.900	0.0733384	102.114	0.270039	$15.0822 \pm 0.687$
63.500	0.0653192	88.537	0.276100	$19.4384 \pm 0.783$
72.000	0.0654819	79.434	0.271507	$23.3859 \pm 0.900$
82.900	0.0749560	68.690	0.257306	$23.7159 \pm 0.859$
92.000	0.0747562	60.428	0.230390	$21.8397 \pm 0.884$
13.900	0.0736106	156.910	0.085095	$9.5438 \pm 1.571$
22.900	0.0739018	142.571	0.239560	$9.9489 \pm 0.669$
33.300	0.0657336	126.976	0.269191	$12.8527 \pm 0.715$
41.900	0.0658171	114.990	0.275354	$13.8532 \pm 0.763$
53.700	0.0747291	99.915	0.264894	$16.4636 \pm 0.766$
62.800	0.0758320	89.318	0.246057	$18.5271 \pm 0.822$

Table A.10:  $(\gamma, pn)$  cross sections for  $E_\gamma=275\text{MeV}$  and  $E_m=40\text{-}70\text{MeV}$

$$E_\gamma = 325 \pm 25 \text{MeV}$$

TOF side ( $n$ )		PIP side ( $p$ )		result
theta(deg)	solid angle(sr)	theta(deg)	solid angle(sr)	$d^2\sigma/d\Omega_n d\Omega_p (\mu b/sr^2)$
102.800	0.0722960	49.239	0.267938	$13.4448 \pm 0.805$
111.700	0.0722018	42.477	0.255970	$10.7291 \pm 0.763$
122.700	0.0638072	34.681	0.233762	$13.9784 \pm 0.973$
131.100	0.0644373	29.078	0.178691	$13.0522 \pm 1.157$
141.300	0.0712122	22.607	0.100567	$10.6675 \pm 1.475$
150.100	0.0705706	17.257	0.037320	$16.1306 \pm 2.667$
42.900	0.0727633	111.121	0.257636	$11.2696 \pm 0.680$
51.900	0.0733384	99.452	0.272440	$11.7311 \pm 0.675$
63.500	0.0653192	85.848	0.275465	$17.2530 \pm 0.827$
72.000	0.0654819	76.801	0.268894	$14.4333 \pm 0.842$
82.900	0.0749560	66.197	0.252696	$18.3244 \pm 0.849$
92.000	0.0747562	58.094	0.200093	$18.2259 \pm 0.959$
13.900	0.0736106	155.764	0.097878	$8.2858 \pm 1.376$
22.900	0.0739018	140.822	0.245588	$6.8345 \pm 0.647$
33.300	0.0657336	124.726	0.271343	$8.8544 \pm 0.661$
41.900	0.0658171	112.481	0.275004	$11.8880 \pm 0.770$
53.700	0.0747291	97.239	0.260986	$14.7604 \pm 0.808$
62.800	0.0758320	86.627	0.213687	$17.0580 \pm 0.910$

Table A.11:  $(\gamma, pn)$  cross sections for  $E_\gamma=325\text{MeV}$  and  $E_m=40\text{-}70\text{MeV}$

$$E_\gamma = 375 \pm 25 \text{ MeV}$$

TOF side ( $n$ )		PIP side ( $p$ )		result
theta(deg)	solid angle(sr)	theta(deg)	solid angle(sr)	$d^2\sigma/d\Omega_n d\Omega_p (\mu b/sr^2)$
102.800	0.0722960	47.358	0.265042	$9.3152 \pm 0.793$
111.700	0.0722018	40.787	0.252297	$9.8207 \pm 0.838$
122.700	0.0638072	33.243	0.227132	$8.8407 \pm 0.969$
131.100	0.0644373	27.842	0.163338	$7.3261 \pm 1.021$
141.300	0.0712122	21.622	0.089204	$9.7597 \pm 1.547$
150.100	0.0705706	16.493	0.028801	$7.2166 \pm 3.490$
42.900	0.0727633	108.765	0.261509	$8.6299 \pm 0.627$
51.900	0.0733384	96.997	0.274132	$11.1058 \pm 0.661$
63.500	0.0653192	83.395	0.274356	$11.9555 \pm 0.746$
72.000	0.0654819	74.415	0.266034	$13.7778 \pm 0.839$
82.900	0.0749560	63.951	0.248134	$12.7115 \pm 0.752$
92.000	0.0747562	56.002	0.173353	$14.2678 \pm 0.964$
13.900	0.0736106	154.660	0.110851	$7.5800 \pm 1.093$
22.900	0.0739018	139.155	0.249433	$6.0184 \pm 0.607$
33.300	0.0657336	122.608	0.272946	$7.9056 \pm 0.634$
41.900	0.0658171	110.143	0.274173	$9.0819 \pm 0.663$
53.700	0.0747291	94.776	0.256862	$11.8095 \pm 0.750$
62.800	0.0758320	84.170	0.181834	$11.9158 \pm 0.887$

Table A.12:  $(\gamma, pn)$  cross sections for  $E_\gamma=375\text{MeV}$  and  $E_m=40\text{-}70\text{MeV}$

$^{12}\text{C}(\gamma, pp)$  cross section with  $E_m=20\text{-}40\text{MeV}$

$E_\gamma = 135 \pm 15\text{MeV}$

TOF side ( $p$ )		PIP side ( $p$ )		result
theta(deg)	solid angle(sr)	theta(deg)	solid angle(sr)	$d^2\sigma/d\Omega_p d\Omega_p (\mu b/sr^2)$
102.800	0.0722960	59.288	0.277838	$0.1459 \pm 0.055$
111.700	0.0722018	51.593	0.271097	$0.0778 \pm 0.054$
122.700	0.0638072	42.516	0.256052	$0.2390 \pm 0.068$
131.100	0.0644373	35.861	0.238400	$0.1859 \pm 0.089$
141.300	0.0712122	28.047	0.165871	$0.0749 \pm 0.058$
150.100	0.0705706	21.496	0.087758	$0.1217 \pm 0.095$
42.900	0.0727633	122.224	0.187152	$0.2166 \pm 0.072$
51.900	0.0733384	111.337	0.257258	$0.2041 \pm 0.057$
63.500	0.0653192	98.093	0.273439	$0.2544 \pm 0.067$
72.000	0.0654819	88.941	0.276142	$0.2096 \pm 0.085$
82.900	0.0749560	77.852	0.270005	$0.1330 \pm 0.055$
92.000	0.0747562	69.111	0.258037	$0.2978 \pm 0.058$
13.900	0.0736106	160.532	0.044506	$-0.2495 \pm 0.168$
22.900	0.0739018	148.197	0.189852	$0.2672 \pm 0.074$
33.300	0.0657336	134.405	0.258785	$0.3320 \pm 0.073$
41.900	0.0658171	123.466	0.272347	$0.2128 \pm 0.077$
53.700	0.0747291	109.224	0.273713	$0.2640 \pm 0.056$
62.800	0.0758320	98.867	0.263436	$0.1437 \pm 0.054$

Table A.13:  $(\gamma, pp)$  cross sections for  $E_\gamma=135\text{MeV}$  and  $E_m=20\text{-}40\text{MeV}$

$$E_\gamma = 175 \pm 25 \text{ MeV}$$

TOF side ( $p$ )		PIP side ( $p$ )		result
theta(deg)	solid angle(sr)	theta(deg)	solid angle(sr)	$d^2\sigma/d\Omega_p d\Omega_p (\mu b/sr^2)$
102.800	0.0722960	56.617	0.276118	$0.2289 \pm 0.062$
111.700	0.0722018	49.155	0.267815	$0.2714 \pm 0.062$
122.700	0.0638072	40.406	0.251431	$0.3945 \pm 0.086$
131.100	0.0644373	34.028	0.230914	$0.2137 \pm 0.106$
141.300	0.0712122	26.571	0.147745	$0.3807 \pm 0.087$
150.100	0.0705706	20.342	0.074668	$0.0315 \pm 0.130$
42.900	0.0727633	119.502	0.222287	$0.6332 \pm 0.079$
51.900	0.0733384	108.374	0.262109	$0.4606 \pm 0.068$
63.500	0.0653192	94.980	0.275147	$0.6616 \pm 0.080$
72.000	0.0654819	85.816	0.275454	$0.6227 \pm 0.104$
82.900	0.0749560	74.812	0.266542	$0.3568 \pm 0.065$
92.000	0.0747562	66.210	0.252722	$0.3711 \pm 0.066$
13.900	0.0736106	159.422	0.055883	$0.2735 \pm 0.175$
22.900	0.0739018	146.458	0.212538	$0.6541 \pm 0.085$
33.300	0.0657336	132.078	0.262593	$0.5602 \pm 0.088$
41.900	0.0658171	120.779	0.274004	$0.6524 \pm 0.087$
53.700	0.0747291	106.226	0.271697	$0.4654 \pm 0.067$
62.800	0.0758320	95.759	0.258567	$0.4285 \pm 0.068$

Table A.14:  $(\gamma, pp)$  cross sections for  $E_\gamma=175\text{MeV}$  and  $E_m=20\text{-}40\text{MeV}$

$$E_\gamma = 225 \pm 25 \text{ MeV}$$

TOF side ( $p$ )		PIP side ( $p$ )		result
theta(deg)	solid angle(sr)	theta(deg)	solid angle(sr)	$d^2\sigma/d\Omega_p d\Omega_p (\mu b/sr^2)$
102.800	0.0722960	53.802	0.273593	$0.9148 \pm 0.082$
111.700	0.0722018	46.597	0.263777	$0.8504 \pm 0.085$
122.700	0.0638072	38.205	0.246037	$0.9929 \pm 0.111$
131.100	0.0644373	32.120	0.217232	$1.2420 \pm 0.148$
141.300	0.0712122	25.039	0.129249	$0.8321 \pm 0.121$
150.100	0.0705706	19.148	0.061350	$0.5701 \pm 0.174$
42.900	0.0727633	116.461	0.247244	$1.1176 \pm 0.089$
51.900	0.0733384	105.101	0.266652	$0.9867 \pm 0.083$
63.500	0.0653192	91.589	0.276083	$1.0321 \pm 0.099$
72.000	0.0654819	82.444	0.273791	$0.9540 \pm 0.124$
82.900	0.0749560	71.562	0.262012	$0.8491 \pm 0.080$
92.000	0.0747562	63.131	0.246373	$0.7282 \pm 0.079$
13.900	0.0736106	158.140	0.070323	$0.8988 \pm 0.187$
22.900	0.0739018	144.465	0.229085	$0.9948 \pm 0.095$
33.300	0.0657336	129.443	0.266299	$1.0764 \pm 0.104$
41.900	0.0658171	117.772	0.275082	$1.0295 \pm 0.107$
53.700	0.0747291	102.923	0.268567	$1.0294 \pm 0.082$
62.800	0.0758320	92.370	0.252353	$1.1568 \pm 0.087$

Table A.15:  $(\gamma, pp)$  cross sections for  $E_\gamma=225\text{MeV}$  and  $E_m=20\text{-}40\text{MeV}$

$$E_\gamma = 275 \pm 25 \text{ MeV}$$

TOF side ( $p$ )		PIP side ( $p$ )		result
theta(deg)	solid angle(sr)	theta(deg)	solid angle(sr)	$d^2\sigma/d\Omega_p d\Omega_p (\mu b/sr^2)$
102.800	0.0722960	51.393	0.270849	$1.1558 \pm 0.101$
111.700	0.0722018	44.418	0.259849	$1.4463 \pm 0.112$
122.700	0.0638072	36.337	0.240122	$1.4315 \pm 0.147$
131.100	0.0644373	30.506	0.196655	$2.1212 \pm 0.215$
141.300	0.0712122	23.747	0.113907	$1.5833 \pm 0.174$
150.100	0.0705706	18.143	0.048603	$1.5304 \pm 0.286$
42.900	0.0727633	113.709	0.252878	$1.7745 \pm 0.112$
51.900	0.0733384	102.175	0.269978	$1.3534 \pm 0.099$
63.500	0.0653192	88.597	0.276107	$1.4312 \pm 0.119$
72.000	0.0654819	79.492	0.271558	$1.1852 \pm 0.135$
82.900	0.0749560	68.745	0.257402	$1.1215 \pm 0.091$
92.000	0.0747562	60.479	0.231056	$1.0351 \pm 0.098$
13.900	0.0736106	156.937	0.084999	$1.3924 \pm 0.214$
22.900	0.0739018	142.612	0.239429	$1.4589 \pm 0.113$
33.300	0.0657336	127.028	0.269136	$1.8758 \pm 0.133$
41.900	0.0658171	115.047	0.275355	$1.9030 \pm 0.132$
53.700	0.0747291	99.975	0.264975	$1.6842 \pm 0.107$
62.800	0.0758320	89.378	0.246189	$1.5600 \pm 0.107$

Table A.16:  $(\gamma, pp)$  cross sections for  $E_\gamma=275\text{MeV}$  and  $E_m=20-40\text{MeV}$

$$E_\gamma = 325 \pm 25 \text{ MeV}$$

TOF side ( $p$ )		PIP side ( $p$ )		result
theta(deg)	solid angle(sr)	theta(deg)	solid angle(sr)	$d^2\sigma/d\Omega_p d\Omega_p (\mu b/sr^2)$
102.800	0.0722960	49.280	0.267998	$0.9513 \pm 0.092$
111.700	0.0722018	42.514	0.256047	$1.0906 \pm 0.101$
122.700	0.0638072	34.712	0.233858	$1.2887 \pm 0.145$
131.100	0.0644373	29.105	0.179029	$1.5170 \pm 0.206$
141.300	0.0712122	22.629	0.100817	$1.2239 \pm 0.179$
150.100	0.0705706	17.273	0.037475	$1.2837 \pm 0.328$
42.900	0.0727633	111.176	0.257539	$1.6437 \pm 0.113$
51.900	0.0733384	99.509	0.272395	$1.2871 \pm 0.099$
63.500	0.0653192	85.904	0.275484	$1.0589 \pm 0.114$
72.000	0.0654819	76.855	0.268953	$0.9906 \pm 0.137$
82.900	0.0749560	66.247	0.252793	$0.9677 \pm 0.093$
92.000	0.0747562	58.140	0.200691	$1.2820 \pm 0.112$
13.900	0.0736106	155.791	0.097773	$1.9178 \pm 0.224$
22.900	0.0739018	140.862	0.245489	$1.4531 \pm 0.113$
33.300	0.0657336	124.777	0.271300	$1.6353 \pm 0.136$
41.900	0.0658171	112.536	0.275018	$1.7868 \pm 0.137$
53.700	0.0747291	97.296	0.261076	$1.5247 \pm 0.105$
62.800	0.0758320	86.683	0.214421	$1.6466 \pm 0.119$

Table A.17:  $(\gamma, pp)$  cross sections for  $E_\gamma=325\text{MeV}$  and  $E_m=20\text{-}40\text{MeV}$

$$E_\gamma = 375 \pm 25 \text{MeV}$$

TOF side ( $p$ )		PIP side ( $p$ )		result
theta(deg)	solid angle(sr)	theta(deg)	solid angle(sr)	$d^2\sigma/d\Omega_p d\Omega_p (\mu b/sr^2)$
102.800	0.0722960	47.396	0.265104	$0.5374 \pm 0.083$
111.700	0.0722018	40.821	0.252373	$0.4796 \pm 0.091$
122.700	0.0638072	33.272	0.227222	$0.5717 \pm 0.138$
131.100	0.0644373	27.867	0.163640	$0.6185 \pm 0.185$
141.300	0.0712122	21.642	0.089427	$0.8170 \pm 0.181$
150.100	0.0705706	16.508	0.028928	$0.6193 \pm 0.307$
42.900	0.0727633	108.818	0.261426	$1.2339 \pm 0.099$
51.900	0.0733384	97.051	0.274100	$1.1388 \pm 0.092$
63.500	0.0653192	83.447	0.274385	$1.0682 \pm 0.108$
72.000	0.0654819	74.465	0.266099	$1.0631 \pm 0.137$
82.900	0.0749560	63.998	0.248232	$0.9714 \pm 0.090$
92.000	0.0747562	56.044	0.173892	$1.0278 \pm 0.109$
13.900	0.0736106	154.687	0.110737	$1.9291 \pm 0.198$
22.900	0.0739018	139.194	0.249345	$1.4216 \pm 0.108$
33.300	0.0657336	122.658	0.272914	$1.3987 \pm 0.128$
41.900	0.0658171	110.196	0.274197	$1.4792 \pm 0.130$
53.700	0.0747291	94.830	0.256958	$1.2817 \pm 0.100$
62.800	0.0758320	84.223	0.182512	$1.2993 \pm 0.125$

Table A.18: ( $\gamma, pp$ ) cross sections for  $E_\gamma=375\text{MeV}$  and  $E_m=20\text{-}40\text{MeV}$

$^{12}\text{C}(\gamma, pp)$  cross section with  $E_m=40\text{-}70\text{MeV}$

$E_\gamma = 135 \pm 15\text{MeV}$

TOF side ( $p$ )		PIP side ( $p$ )		result
theta(deg)	solid angle(sr)	theta(deg)	solid angle(sr)	$d^2\sigma/d\Omega_p d\Omega_p (\mu b/sr^2)$
102.800	0.0722960	59.288	0.277838	$0.4943 \pm 0.065$
111.700	0.0722018	51.593	0.271097	$0.4425 \pm 0.061$
122.700	0.0638072	42.516	0.256052	$0.3811 \pm 0.074$
131.100	0.0644373	35.861	0.238400	$0.3941 \pm 0.093$
141.300	0.0712122	28.047	0.165871	$0.4817 \pm 0.075$
150.100	0.0705706	21.496	0.087758	$0.1932 \pm 0.096$
42.900	0.0727633	122.224	0.187152	$0.2840 \pm 0.062$
51.900	0.0733384	111.337	0.257258	$0.3691 \pm 0.054$
63.500	0.0653192	98.093	0.273439	$0.4204 \pm 0.064$
72.000	0.0654819	88.941	0.276142	$0.5038 \pm 0.086$
82.900	0.0749560	77.852	0.270005	$0.4673 \pm 0.056$
92.000	0.0747562	69.111	0.258037	$0.5197 \pm 0.056$
13.900	0.0736106	160.532	0.044506	$0.5450 \pm 0.163$
22.900	0.0739018	148.197	0.189852	$0.1682 \pm 0.061$
33.300	0.0657336	134.405	0.258785	$0.3508 \pm 0.067$
41.900	0.0658171	123.466	0.272347	$0.4987 \pm 0.071$
53.700	0.0747291	109.224	0.273713	$0.4711 \pm 0.055$
62.800	0.0758320	98.867	0.263436	$0.3394 \pm 0.051$

Table A.19:  $(\gamma, pp)$  cross sections for  $E_\gamma=135\text{MeV}$  and  $E_m=40\text{-}70\text{MeV}$

$$E_\gamma = 175 \pm 25 \text{ MeV}$$

TOF side ( $p$ )		PIP side ( $p$ )		result
theta(deg)	solid angle(sr)	theta(deg)	solid angle(sr)	$d^2\sigma/d\Omega_p d\Omega_p (\mu b/sr^2)$
102.800	0.0722960	56.617	0.276118	$1.7864 \pm 0.101$
111.700	0.0722018	49.155	0.267815	$1.3868 \pm 0.094$
122.700	0.0638072	40.406	0.251431	$1.4181 \pm 0.119$
131.100	0.0644373	34.028	0.230914	$1.0153 \pm 0.133$
141.300	0.0712122	26.571	0.147745	$0.9788 \pm 0.114$
150.100	0.0705706	20.342	0.074668	$0.8703 \pm 0.158$
42.900	0.0727633	119.502	0.222287	$1.6401 \pm 0.102$
51.900	0.0733384	108.374	0.262109	$1.5668 \pm 0.094$
63.500	0.0653192	94.980	0.275147	$1.8175 \pm 0.114$
72.000	0.0654819	85.816	0.275454	$1.9276 \pm 0.145$
82.900	0.0749560	74.812	0.266542	$2.0432 \pm 0.096$
92.000	0.0747562	66.210	0.252722	$1.7682 \pm 0.096$
13.900	0.0736106	159.422	0.055883	$0.5431 \pm 0.212$
22.900	0.0739018	146.458	0.212538	$1.4092 \pm 0.103$
33.300	0.0657336	132.078	0.262593	$1.3118 \pm 0.111$
41.900	0.0658171	120.779	0.274004	$1.8646 \pm 0.121$
53.700	0.0747291	106.226	0.271697	$1.6742 \pm 0.091$
62.800	0.0758320	95.759	0.258567	$1.6373 \pm 0.095$

Table A.20:  $(\gamma, pp)$  cross sections for  $E_\gamma=175 \text{ MeV}$  and  $E_m=40-70 \text{ MeV}$

$$E_\gamma = 225 \pm 25 \text{MeV}$$

TOF side ( $p$ )		PIP side ( $p$ )		result
theta(deg)	solid angle(sr)	theta(deg)	solid angle(sr)	$d^2\sigma/d\Omega_p d\Omega_p (\mu b/sr^2)$
102.800	0.0722960	53.802	0.273593	$2.8344 \pm 0.129$
111.700	0.0722018	46.597	0.263777	$2.5933 \pm 0.125$
122.700	0.0638072	38.205	0.246037	$2.3105 \pm 0.156$
131.100	0.0644373	32.120	0.217232	$2.5413 \pm 0.214$
141.300	0.0712122	25.039	0.129249	$2.4676 \pm 0.178$
150.100	0.0705706	19.148	0.061350	$1.8635 \pm 0.248$
42.900	0.0727633	116.461	0.247244	$3.2541 \pm 0.129$
51.900	0.0733384	105.101	0.266652	$3.3008 \pm 0.125$
63.500	0.0653192	91.589	0.276083	$3.3980 \pm 0.152$
72.000	0.0654819	82.444	0.273791	$3.5346 \pm 0.193$
82.900	0.0749560	71.562	0.262012	$3.2308 \pm 0.124$
92.000	0.0747562	63.131	0.246373	$3.1865 \pm 0.127$
13.900	0.0736106	158.140	0.070323	$2.0987 \pm 0.260$
22.900	0.0739018	144.465	0.229085	$2.4880 \pm 0.133$
33.300	0.0657336	129.443	0.266299	$2.7152 \pm 0.147$
41.900	0.0658171	117.772	0.275082	$3.1571 \pm 0.153$
53.700	0.0747291	102.923	0.268567	$3.1018 \pm 0.123$
62.800	0.0758320	92.370	0.252353	$3.4281 \pm 0.131$

Table A.21:  $(\gamma, pp)$  cross sections for  $E_\gamma=225\text{MeV}$  and  $E_m=40\text{-}70\text{MeV}$

$$E_\gamma = 275 \pm 25 \text{ MeV}$$

TOF side ( $p$ )		PIP side ( $p$ )		result
theta(deg)	solid angle(sr)	theta(deg)	solid angle(sr)	$d^2\sigma/d\Omega_p d\Omega_p (\mu b/sr^2)$
102.800	0.0722960	51.393	0.270849	$3.2320 \pm 0.156$
111.700	0.0722018	44.418	0.259849	$3.1496 \pm 0.158$
122.700	0.0638072	36.337	0.240122	$3.0346 \pm 0.204$
131.100	0.0644373	30.506	0.196655	$3.0182 \pm 0.282$
141.300	0.0712122	23.747	0.113907	$3.3442 \pm 0.241$
150.100	0.0705706	18.143	0.048603	$3.4756 \pm 0.379$
42.900	0.0727633	113.709	0.252878	$3.8422 \pm 0.158$
51.900	0.0733384	102.175	0.269978	$4.4028 \pm 0.158$
63.500	0.0653192	88.597	0.276107	$3.9561 \pm 0.184$
72.000	0.0654819	79.492	0.271558	$3.7506 \pm 0.226$
82.900	0.0749560	68.745	0.257402	$3.7155 \pm 0.151$
92.000	0.0747562	60.479	0.231056	$3.6246 \pm 0.157$
13.900	0.0736106	156.937	0.084999	$2.8959 \pm 0.306$
22.900	0.0739018	142.612	0.239429	$3.7398 \pm 0.163$
33.300	0.0657336	127.028	0.269136	$3.3886 \pm 0.181$
41.900	0.0658171	115.047	0.275355	$3.6253 \pm 0.188$
53.700	0.0747291	99.975	0.264975	$3.9104 \pm 0.157$
62.800	0.0758320	89.378	0.246189	$4.0025 \pm 0.163$

Table A.22:  $(\gamma, pp)$  cross sections for  $E_\gamma=275 \text{ MeV}$  and  $E_m=40-70 \text{ MeV}$

$$E_\gamma = 325 \pm 25 \text{ MeV}$$

TOF side ( $p$ )		PIP side ( $p$ )		result
theta(deg)	solid angle(sr)	theta(deg)	solid angle(sr)	$d^2\sigma/d\Omega_p d\Omega_p (\mu b/sr^2)$
102.800	0.0722960	49.280	0.267998	$2.5013 \pm 0.155$
111.700	0.0722018	42.514	0.256047	$2.2666 \pm 0.151$
122.700	0.0638072	34.712	0.233858	$2.5575 \pm 0.211$
131.100	0.0644373	29.105	0.179029	$2.5892 \pm 0.294$
141.300	0.0712122	22.629	0.100817	$1.7988 \pm 0.243$
150.100	0.0705706	17.273	0.037475	$2.0552 \pm 0.426$
42.900	0.0727633	111.176	0.257539	$3.2016 \pm 0.158$
51.900	0.0733384	99.509	0.272395	$3.3852 \pm 0.152$
63.500	0.0653192	85.904	0.275484	$3.2384 \pm 0.180$
72.000	0.0654819	76.855	0.268953	$3.4206 \pm 0.233$
82.900	0.0749560	66.247	0.252793	$2.9520 \pm 0.147$
92.000	0.0747562	58.140	0.200691	$3.2545 \pm 0.165$
13.900	0.0736106	155.791	0.097773	$2.9671 \pm 0.276$
22.900	0.0739018	140.862	0.245489	$3.3845 \pm 0.165$
33.300	0.0657336	124.777	0.271300	$2.5854 \pm 0.173$
41.900	0.0658171	112.536	0.275018	$2.9873 \pm 0.182$
53.700	0.0747291	97.296	0.261076	$3.4083 \pm 0.156$
62.800	0.0758320	86.683	0.214421	$3.6867 \pm 0.176$

Table A.23:  $(\gamma, pp)$  cross sections for  $E_\gamma = 325 \text{ MeV}$  and  $E_m = 40\text{-}70 \text{ MeV}$

$$E_\gamma = 375 \pm 25 \text{MeV}$$

TOF side ( $p$ )		PIP side ( $p$ )		result
theta(deg)	solid angle(sr)	theta(deg)	solid angle(sr)	$d^2\sigma/d\Omega_p d\Omega_p (\mu b/sr^2)$
102.800	0.0722960	47.396	0.265104	$1.6869 \pm 0.146$
111.700	0.0722018	40.821	0.252373	$1.4959 \pm 0.148$
122.700	0.0638072	33.272	0.227222	$1.9503 \pm 0.208$
131.100	0.0644373	27.867	0.163640	$2.0775 \pm 0.298$
141.300	0.0712122	21.642	0.089427	$1.9449 \pm 0.256$
150.100	0.0705706	16.508	0.028928	$1.8631 \pm 0.443$
42.900	0.0727633	108.818	0.261426	$2.6317 \pm 0.141$
51.900	0.0733384	97.051	0.274100	$2.5988 \pm 0.136$
63.500	0.0653192	83.447	0.274385	$2.9727 \pm 0.169$
72.000	0.0654819	74.465	0.266099	$2.8896 \pm 0.215$
82.900	0.0749560	63.998	0.248232	$2.3460 \pm 0.138$
92.000	0.0747562	56.044	0.173892	$2.3716 \pm 0.165$
13.900	0.0736106	154.687	0.110737	$2.7155 \pm 0.247$
22.900	0.0739018	139.194	0.249345	$2.8194 \pm 0.153$
33.300	0.0657336	122.658	0.272914	$2.5431 \pm 0.166$
41.900	0.0658171	110.196	0.274197	$2.7841 \pm 0.176$
53.700	0.0747291	94.830	0.256958	$2.6568 \pm 0.143$
62.800	0.0758320	84.223	0.182512	$3.1988 \pm 0.177$

Table A.24:  $(\gamma, pp)$  cross sections for  $E_\gamma=375\text{MeV}$  and  $E_m=40\text{-}70\text{MeV}$

# Appendix B

## Correction factors applied to TOF dead bars

PIP position	Neutron Angle	Neutrons in TOF	Protons in TOF
forward	102.8°	1.0	1.0
	111.7°	1.0	1.0
	122.7°	1.047	1.333
	131.1°	1.179	2.0
	141.3°	1.120	1.0
	150.1°	1.067	1.0
center	42.9°	1.0	1.0
	51.9°	1.0	1.0
	63.5°	1.047	1.333
	72.0°	1.179	2.0
	82.9°	1.047	1.0
	92.0°	1.067	1.0
backward	13.9°	1.0	1.0
	22.9°	1.0	1.0
	33.3°	1.047	1.333
	41.9°	1.120	1.333
	53.7°	1.047	1.0
	62.8°	1.067	1.0

Table B.1: *correction factors applied to dead TOF bars*

# Appendix C

## Energy threshold correction factors

Threshold correction for photon energy bin of  $135 \pm 15 \text{ MeV}$  is tabled below for the corresponding angular bins. The correction factors are also averaged over the two missing energy bins of 20-40MeV and 40-70MeV.

PIP geometry	PIP Proton Angle	$E_m$ 20-40MeV	$E_m$ 40-70MeV
forward	59.22°	1.073	1.333
	51.53°	1.067	1.285
	42.47°	1.047	1.240
	35.82°	1.042	1.221
	28.01°	1.029	1.237
	21.47°	1.039	1.228
center	122.16°	1.377	1.915
	111.27°	1.328	1.796
	98.02°	1.288	1.697
	88.87°	1.287	1.589
	77.78°	1.243	1.457
	69.04°	1.220	1.447
backward	160.50°	1.503	2.551
	148.16°	1.465	2.475
	134.35°	1.422	2.318
	123.40°	1.405	2.014
	109.15°	1.360	1.878
	98.79°	1.341	1.831

Table C.1: *Detector energy threshold correction factors for photon bins  $E_\gamma = 135 \pm 15 \text{ MeV}$ . The uncertainties for the factors are  $\sim 2\%$ , see discussion on threshold correction in Chapter 4.*

# Bibliography

- [1] M.Q. Barton and J.H. Smith, Phys. Rev. 95 (1954) 573.
- [2] K. Gottfried, Nucl. Phys. 5 (1958) 557.
- [3] M. Vanderhaeghen, L. Machenil, J. Ryckebusch and M. Waroquier, Nucl.Phys. A580 (1994) 551.
- [4] L. Machenil, M. Vanderhaeghen, J. Ryckebusch and M. Waroquier, Phys Lett B 316 (1993) 17.
- [5] M.Q. Barton and J.H. Smith, Phys. Rev. 110 (1958) 1143.
- [6] J. Garvey *et al.*, Nucl. Phys. 70 (1965) 241.
- [7] I.L. Smith, J. Garvey, J.G. Rutherglen and G.R. Brookes, Nucl. Phys. B1 (1967) 483.
- [8] S.N. Dancer *et al.*, Phys. Rev. Lett. 61 (1988) 1170.
- [9] I.J.D. MacGregor *et al.*, Nucl. Phys. A533 (1991) 269.
- [10] J.C. McGeorge *et al.*, Phys. Rev. C51 (1995) 1967.
- [11] J. Ahrens, Nucl. Phys. A446 (1985) 229c.
- [12] D. Walker, Phys. Rev. 81 (1951) 634.
- [13] C. Levinthal and A. Silverman, Phys. Rev. 82 (1951) 822.

- [14] J.C. Keck, Phys. Rev. 85 (1952) 410.
- [15] J.S. Levinger, Phys. Rev. 84 (1951) 43.
- [16] J.S. Levinger, Phys. Lett. B82 (1979) 181.
- [17] B.L. Berman, S.C. Fultz and P.F. Yergin, Phys. Rev. C10 (1974) 2221.
- [18] P.C. Stein *et al.*, Phys. Rev. 119 (1960) 348.
- [19] R.M. Weinstein *et al.*, Phys. Rev. 99 (1955) 1621.
- [20] J. Arends *et al.*, Z. Phys. A298 (1980) 103.  
J. Arends *et al.*, Z. Phys. A305 (1982) 205.  
J. Arends *et al.*, Nucl. Phys. A526 (1991) 479.
- [21] S. Homma *et al.*, Phys. Rev. Lett. 45 (1980) 706.  
S. Homma *et al.*, Phys. Rev. Lett. 52 (1984) 2026.  
S. Homma *et al.*, Phys. Rev. Lett. 53 (1984) 2536.  
S. Homma *et al.*, Phys. Rev. C 27 (1983) 31.
- [22] M. Kanazawa *et al.*, Phys. Rev. C 35 (1987) 1828.
- [23] K. Baba *et al.*, Nucl. Phys. A415 (1984) 462.
- [24] S.M. Doran *et al.*, Nucl. Phys. A559 (1993) 347.
- [25] S. Klein, Universität Tübingen PhD Thesis (1990).
- [26] J. Ryckebusch, M. Vanderhaeghen, L. Machenil and M. Waroquier,  
Nucl.Phys. A568 (1994) 828.
- [27] P.D. Harty *et al.*, Phys. Rev. C47 (1993) 2185.
- [28] O.A.P Tavares and M.L. Terranova, J.Phys.G 18 (1992) 521.

- [29] J Ahrens *et al.*, Nucl Phys A251 (1975) 479.
- [30] R. Jastrow, Phys. Rev. 98 (1955) 1479.
- [31] P.D. Harty *et al.*, Phys. Rev. C\_ (1996) 2185. *to be published*
- [32] J. Ryckebusch, L. Machenil, M. Vanderhaeghen, and M. Waroquier, Phys. Lett. B 291 (1992) 213.
- [33] L. Van Hoorebeke *et al.*, Phys. Rev. C42 (1990) R1179.
- [34] W. Weise, M.G. Huber and M. Danos, Z.Phys. 236 (1970) 176.
- [35] M. Gari and H. Hebach, Phys. Reports 72 (1981) 1.
- [36] A.J.F. Siegert, Phys. Rev. 52 (1937) 787.
- [37] M. Wakamatsu and K. Matsumoto, Nucl. Phys. A392 (1983) 323.
- [38] L. Boato and M.M. Giannini, J.Phys.G 15 (1989) 1605.
- [39] C. Giusti, F.D. Pacati and M. Radici, Nucl. Phys. A546 (1992) 607.
- [40] T. Omhura, N. Morita and M. Yamada, Prog.Theor.Phys. 15 (1956) 222.
- [41] R.V. Reid Jr., Ann. of Phys. 50 (1968) 411.
- [42] S. Boffi, C. Giusti, F.D. Pacati and M. Radici, Nucl. Phys. A546 (1993) 473.
- [43] R.C. Carrasco and E. Oset *et al.*, Nucl. Phys. A536 (1992) 445. R.C. Carrasco and E. Oset, Nucl. Phys. A570 (1994) 701.
- [44] G.E. Cross and I.J.D. MacGregor *et al.*, Nucl. Phys. A593 (1995) 463.
- [45] T. Hehl *private communication*. T. Lamparter *to be published*
- [46] J. Ryckebusch, Proceedings of the 6th Workshop on Perspectives in Nuclear Physics (1993).

- [47] I. Anthony *et al.*, NIM A301 (1991) 230.
- [48] S.J. Hall, G.J. Miller, R. Beck and P. Jennewein, NIM A368 (1996) 698.
- [49] S.J. Hall and G.J. Miller, Kelvin Lab Annual Report 1990, pp 35-38.
- [50] J.R.M Annand and B. Oussena, NIM A330 (1993) 220.
- [51] T. Hehl *et al.*, NIM A354 (1995) 505
- [52] J. A. MacKenzie, University of Edinburgh, PhD Thesis (1995).
- [53] D. Watts, PhD Thesis, to be submitted
- [54] J.R.M. Annand, *Kelvin Lab Internal Report*.
- [55] W. Braunschweig *et al.*, NIM 134 (1976) 261.
- [56] G.E. Cross *private communication*.
- [57] T. Hehl *private communication*.
- [58] G.J. Miller *private communication*.
- [59] R.A. Cecil *et al.*, NIM 161 (1979) 439.
- [60] R. Madey *et al.*, NIM 151 (1978) 445.
- [61] *Scintillation Materials*, NE Technology Catalogue.
- [62] S.N Dancer, University of Glasgow, PhD Thesis (1987).
- [63] S. Franczuk *private communication*.
- [64] T. Lamparter *private communication*
- [65] D.F. Measday and C. Richard-Serre, CERN 69-17 (1969).
- [66] Proceedings of the IOP Conf. on Nucl. and Part. Phys. 133 (1993) 104